HIGH-FIDELITY SIMULATION OF COMPRESSIBLE FLOWS FOR HYPERSONIC PROPULSION APPLICATIONS

by

Collin C. Otis

BS, University of Pittsburgh, 2008

MS, University of Pittsburgh, 2010

Submitted to the Graduate Faculty of

the Swanson School of Engineering in partial fulfillment

of the requirements for the degree of

Doctor of Philosophy

University of Pittsburgh

2013

UNIVERSITY OF PITTSBURGH

SWANSON SCHOOL OF ENGINEERING

This dissertation was presented

by

Collin C. Otis

It was defended on

March 29, 2013

and approved by

Peyman Givi, PhD, James T. MacLeod Professor, Department of Mechanical

Engineering and Materials Science and

Professor, Department of Chemical and Petroleum Engineering

Anne M. Robertson, PhD, Associate Professor, Department of Mechanical

Engineering and Materials Science

Guofeng Wang, PhD, Assistant Professor, Department of Mechanical

Engineering and Materials Science

Ivan Yotov, PhD, Professor and Chair, Department of Mathematics

Dissertation Director: **Peyman Givi, PhD**, James T. MacLeod Professor,

Department of Mechanical Engineering and Materials Science and

Professor, Department of Chemical and Petroleum Engineering

HIGH-FIDELITY SIMULATION OF COMPRESSIBLE FLOWS FOR HYPERSONIC PROPULSION APPLICATIONS

Collin C. Otis, PhD

University of Pittsburgh, 2013

In the first part of this dissertation, the scalar filtered mass density function (SFMDF) methodology is implemented into the computer code US3D. The SFMDF is a sub-grid scale closure and is simulated via a Lagrangian Monte Carlo solver. US3D is an Eulerian finite volume code and has proven very effective for compressible flow simulations. The resulting SFMDF-US3D code is employed for large eddy simulation (LES) of compressible turbulent flows on unstructured meshes. Simulations are conducted of subsonic and supersonic flows. The consistency and accuracy of the simulated results are assessed along with appraisal of the overall performance of the methodology.

In the second part of this dissertation, a new methodology is developed for accurate capturing of discontinuities in multi-block finite difference simulations of hyperbolic partial differential equations. The fourth-order energy-stable weighted essentially non-oscillatory (ESWENO) scheme on closed domains is combined with simultaneous approximation term (SAT) weak interface and boundary conditions. The capability of the methodology is demonstrated for accurate simulations in the presence of significant and abrupt changes in grid resolution between neighboring subdomains. Results are presented for the solutions of linear scalar hyperbolic wave equations and the Euler equations in one and two dimensions. Strong discontinuities are passed across subdomain interfaces without significant distortions. It is demon-

strated that the methodology provides stable and accurate solutions even when large differences in the grid-spacing exist, whereas strong imposition of the interface conditions causes noticeable oscillations.

Keywords: Large eddy simulation, filtered density function, turbulent reacting flows, multi-block finite difference schemes, high-order numerical methods, WENO shock-capturing, computational fluid dynamics.

TABLE OF CONTENTS

LIST OF TABLES

LIST OF FIGURES

ACKNOWLEDGMENTS

and high school Physics, Biology, Precalculus, and Calculus teacher, Mrs. Judith S. Huyett, who was one of the first to instill in me a love of physics, math, and science as a whole.

I am inexpressibly grateful to my loving parents, Pastor Christopher D. Otis and Mrs. Karen A. Otis, for instilling the values of hard work, discipline, and perseverance in me as a youth. They never let me settle for second-best and always pushed me to do more than I thought was possible. Mom and Dad: I owe any success in life to your careful raising and continued love. Thank you.

I reserve a special thanks for my wonderful, courageous, and strong wife, Mrs. Audra M. Otis. She has been an ever-constant love, support, strength, comforter, and closest friend and ally. Without her love, friendship, and support, I could never have started or finished this undertaking. Thank you. To our beloved children, Sydney and Brady, thank you for bringing immeasurable joy and purpose to my life. Audge, Sydney, and Brady: I love you very much. Coming home to you each day makes me a very happy, rich, and lucky husband and dad.

These acknowledgements represent a small portion of the many people who have helped immeasurably to conceive this work and the PhD it represents. If such an exhaustive list were to be penned, it would consume more pages than the dissertation itself. I express my sincere gratitude to each one.

Above all, I thank my Lord, Jesus Christ, for His hand on my life. I am grateful to Him for orchestrating my circumstances to His pleasure and guiding me through each day. May this work bring glory to Him.

1.0   INTRODUCTION

One of the most challenging issues in hypersonic propulsion systems is the predic-
tion of high-speed turbulent reactive flows via computational fluid dynamics (CFD).
For reliable simulations, the underlying CFD methods must be capable of capturing
the chaotic fluid mechanics of an exceedingly complex system of nonlinear chemi-
cal, physical, and thermodynamic processes. This requires that a large number of
individually challenging problems be overcome simultaneously. The flows under con-
sideration are highly-compressible with strong stationary and moving shocks that
can only be captured via accurate and stable numerical methods. The concurrent
existence of regions of premixed and nonpremixed combustion necessitates robust
physical and chemical models to properly account for the reactants conversion. The
entire field is turbulence-dominated and stochastic; thus, turbulence modeling is es-
pecially important to capture highly-nonlinear turbulence-chemistry interactions. In
addition, a myriad of other complexities must be properly treated, such as boundary
conditions, grid generation & refinement, treatment of complex geometries, shock-
vortex interactions, reduced chemistry mechanisms, and computational scalability,
to name a few. Two of the most critical challenges currently at the forefront of CFD
development for high-speed combustion are:[4]

   (1) accurate and generalizable turbulent combustion models, and

   (2) high-order accurate and stable numerical methods.

The thrust of this dissertation is to progress the state-of-the-art in both of these
areas.

   The first objective of this work is to develop an accurate and flexible turbulent
combustion model for prediction of high-speed flows. Amongst the CFD methodolo-
gies currently available, it is widely accepted that the optimal means of capturing the

physics of turbulent reacting flows is via large eddy simulation (LES). In LES, one of the most challenging technical obstacles is associated with the subgrid scale (SGS) quantities. For accurate and consistent modeling of these quantities,[5–11] the filtered density function (FDF) methodology, including its mass-weighted form, the filtered mass density function (FMDF), has proven particularly effective.[12,13] The FDF is essentially the counterpart of the probability density function (PDF) methodology in Reynolds-averaged Navier-Stokes (RANS) simulations.[8,11,14] In its most comprehensive, stand-alone form, the FDF accounts for the joint statistics of *five* SGS variables: energy, pressure, frequency, velocity, and all other scalar variables.[15] The level of sophistication can be reduced with consideration of fewer variables. The simplest and most widely used form considers only the scalar field (SFDF and SFMDF)[16,17] and has been successful for prediction of a variety turbulent flames.[18–26]

A major challenge associated with FDF is its implementation in complex geometries. Structured multi-block grids lack the required flexibility and robustness to deal with such geometries. Unstructured grids provide a good option for discretization on complex shapes. The objective here is to implement the SFMDF on the popular and very powerful unstructured US3D finite volume (FV) computer code.[27] The flow solver in this code is based on the kinetic energy consistent (KEC) approach[28] that has been extended to sixth-order accuracy. Careful choices of limiters allow high-order solutions to be obtained on a wide range of flows relevant to hypersonic propulsion systems. The high fidelity and scalability of US3D have been demonstrated in numerous successful applications.[27–36] Herein, a simulation strategy for FDF on US3D is developed with the first demonstration of SFMDF for LES of compressible flows on unstructured meshes. Sample LES results are presented of subsonic and supersonic temporally-developing mixing layers under non-reacting and reacting conditions.

The second objective of this work is to advance the state-of-the-art in numerical solution of highly compressible flows. In these flows, the presence of discontinuities makes it a challenge to obtain accurate and stable solutions. High-order weighted essentially non-oscillatory (WENO) methods have become popular for such cases.[37–40] The high-order nature of WENO schemes allows for accurate resolution

2

of detailed physics, while the stencil-biasing mechanics prevent numerical oscillations near discontinuities. While WENO schemes are very robust in practice, they do not satisfy a summation by parts (SBP) convention by default.[41,42] Therefore, a general time-stability proof cannot be derived.[43] In contrast, the energy-stable WENO (ESWENO) scheme[43–46] satisfies SBP and is stable in the L_2 sense.

A major challenge in the practical application of ESWENO is generating appropriate finite-difference grids. Grids must be smoothly-varying and match boundaries with a high order of accuracy. In moderately complex geometries, mapping such a smooth mesh to complicated boundaries can be extremely time-consuming, if not impossible. If such a mesh *can* be generated, necessary local grid refinement is usually not feasible. Such geometries are often treated with unstructured FV techniques with sacrifice of the accuracy. Alternatively, multi-block meshes can alleviate such difficulties while maintaining high fidelity. Here, a multi-block ESWENO scheme is developed. Each subdomain is mapped with an independent curvilinear mesh; the only requirement is that neighboring subdomains have collocated grid points along the interface surface. The simultaneous approximation term (SAT) interface closure is used to close interface and global domain boundaries.[47] The new scheme, denoted by ESWENO-SAT, is shown to be stable for linear conservation laws with continuous solutions. One- and two-dimensional flows are considered to demonstrate the solution procedure for systems of linear and nonlinear hyperbolic equations on multi-block domains.

1.1   SCOPE

This dissertation is organized as follows. Chapter 2 deals with SFMDF on US3D. The work described in this chapter was presented at the 42nd AIAA Fluid Dynamics Conference & Exhibit,[48] and the 48th AIAA/ASME/SAE/ASEE Joint Propulsion Conference & Exhibit.[49] It was also part of an invited talk at the 47th AIAA/ASME/SAE/ASEE Joint Propulsion Conference & Exhibit[50] and is currently in press.[51] Chapter 3 deals with the ESWENO-SAT scheme. The work described in this chap-

ter was presented at the 42nd AIAA Fluid Dynamics Conference & Exhibit[52] and the 7th International Conference on Computational Fluid Dynamics (ICCFD7).[53] It was awarded Second Place, Student Paper Award at the latter.

2.0   SFMDF IN US3D

In the work described in this chapter, the scalar filtered mass density function (SFMDF) methodology is implemented into the computer code US3D. The SFMDF is a subgrid scale (SGS) closure and is simulated via a Lagrangian Monte Carlo solver. US3D is an Eulerian finite volume (FV) hydrodynamic solver and has proven very effective for compressible flow simulations. The resulting SFMDF-US3D code is employed for large eddy simulation (LES) of compressible turbulent flows on unstructured meshes. Simulations are conducted of subsonic and supersonic flows under non-reacting and reacting conditions. The consistency and the accuracy of the simulated results are assessed along with appraisal of the overall performance of the methodology.

2.1   FORMULATION

2.1.1   Governing Equations

High-speed reacting flows are rich with complexities due to the intimate interdependence of mixing, chemical reaction, and hydrodynamics. The transport variables to describe such flows are the fluid mass density $\rho\left(\boldsymbol{x}, t\right)$, the velocity vector $\boldsymbol{u}\left(\boldsymbol{x}, t\right) = [u_1, u_2, u_3]$, total specific enthalpy $h\left(\boldsymbol{x}, t\right)$, and mass fractions of N_s chem-

ical species $[\phi_1, ..., \phi_{N_s}]$, where $\boldsymbol{x} = [x_1, x_2, x_3]$ is the position vector and t is time. Neglecting radiation and body forces and assuming unity Lewis number, the conservation equations are[6]

$$\frac{\partial \rho}{\partial t} + \frac{\partial \rho u_i}{\partial x_i} = 0, \tag{2.1}$$

$$\frac{\partial \rho u_j}{\partial t} + \frac{\partial \rho u_i u_j}{\partial x_i} = -\frac{\partial p}{\partial x_j} + \frac{\partial \tau_{ij}}{\partial x_i}, \tag{2.2}$$

$$\frac{\partial \rho \phi_\alpha}{\partial t} + \frac{\partial \rho u_i \phi_\alpha}{\partial x_i} = -\frac{\partial J_i^\alpha}{\partial x_i} + \rho S_\alpha, \quad \alpha = 1, 2, \ldots, N_s \tag{2.3}$$

$$\frac{\partial \rho h}{\partial t} + \frac{\partial \rho u_i h}{\partial x_i} = -\frac{\partial q_i}{\partial x_i} + \frac{\partial p}{\partial t} + u_i \frac{\partial p}{\partial x_i} + \tau_{ij} \frac{\partial u_i}{\partial x_j}, \tag{2.4}$$

where p is the thermodynamic pressure, τ_{ij} are the components of the viscous stress tensor, q_i is the heat flux in the ith direction, and J_i^α is the scalar mass flux of chemical species α in the ith direction. To facilitate the use of conservative numerical schemes, it is sometimes useful to consider the total energy,

$$E(\boldsymbol{x}, t) = h - \frac{p}{\rho} + \frac{1}{2} u_i u_i, \tag{2.5}$$

which is governed by

$$\frac{\partial \rho E}{\partial t} + \frac{\partial \rho u_i E}{\partial x_i} = -\frac{\partial q_i}{\partial x_i} + \frac{\partial \sigma_{ij} u_i}{\partial x_j}, \tag{2.6}$$

where $\sigma_{ij} = \tau_{ij} - p\delta_{ij}$ and δ_{ij} is the kronecker delta. We define $\boldsymbol{\phi}$ as the scalar array,

$$\boldsymbol{\phi} = [\phi_1, \ldots, \phi_{N_s}, \phi_{N_h}], \quad N_h = N_s + 1, \quad \boldsymbol{\phi}_{N_h} = h. \tag{2.7}$$

The total specific enthalpy is defined as

$$h = \sum_{\alpha=1}^{N_s} h_\alpha \phi_\alpha, \quad h_\alpha = \Delta h_\alpha^\circ + \int_{T_0}^{T} c_{p_\alpha} dT', \tag{2.8}$$

where $T(\boldsymbol{x}, t)$ is the thermodynamic temperature, T_0 is the reference temperature, c_{p_α} is the specific heat of species α under constant pressure, and Δh_α° is the enthalpy of formation of species α at the reference temperature. The system is closed with an ideal gas equation of state,

$$p = \rho R T, \quad R = \phi_\alpha \frac{\mathcal{R}}{W_\alpha}, \tag{2.9}$$

where R is the specific gas constant of the mixture, $\mathcal{R}$ is the universal gas constant, and W_α is the molecular weight of species α. Assuming a Newtonian fluid with Fourier conduction, the diffusive fluxes are modeled,[54]

$$\tau_{ij} = 2\mu S_{ij} - \frac{2}{3}\mu S_{nn}\delta_{ij}, \tag{2.10}$$

$$q_i = -\lambda\frac{\partial T}{\partial x_i} + \rho\sum_{\alpha=1}^{N_s}\Delta h_\alpha^\circ \phi_\alpha V_{\alpha,i}, \tag{2.11}$$

$$J_i^\alpha = \rho\phi_\alpha V_{\alpha,i}, \tag{2.12}$$

where μ is the fluid dynamic viscosity, λ is the thermal conductivity, and $V_{\alpha,i}$ is the diffusion velocity of species α in the ith direction. The strain rate is defined as:

$$S_{ij} = \frac{1}{2}\left(\frac{\partial u_i}{\partial x_j} + \frac{\partial u_j}{\partial x_i}\right). \tag{2.13}$$

Assuming Fickian diffusion,

$$\phi_{(\alpha)}V_{(\alpha),i} = -D\frac{\partial \phi_\alpha}{\partial x_i}, \tag{2.14}$$

where parentheses prevent summation convention and D is the coefficient of diffusion, assumed constant. The modeled fluxes are

$$\tau_{ij} = \mu\left(\frac{\partial u_i}{\partial x_j} + \frac{\partial u_j}{\partial x_i} - \frac{2}{3}\frac{\partial u_n}{\partial x_n}\delta_{ij}\right), \tag{2.15}$$

$$q_i = -\lambda\frac{\partial T}{\partial x_i} - \gamma\Delta h_\alpha^\circ\frac{\partial \phi_\alpha}{\partial x_i} = -\gamma\frac{\partial h}{\partial x_i}, \tag{2.16}$$

$$J_i^\alpha = -\gamma\frac{\partial \phi_\alpha}{\partial x_i}, \tag{2.17}$$

where $\gamma = \rho D$ is the mass and thermal diffusivity. The final equivalence in Eq. (2.16) assumes calorically perfect gas (CPG).

2.1.2 Large Eddy Simulation

Large eddy simulation (LES) involves the use of a spatial filtering function:[8,55,56]

$$\langle Q\left(\boldsymbol{x},t\right)\rangle_{l} = \int_{-\infty}^{\infty} Q\left(\boldsymbol{x}',t\right)\mathcal{G}\left(\boldsymbol{x}',\boldsymbol{x}\right)\mathrm{d}\boldsymbol{x}', \qquad (2.18)$$

where $\mathcal{G}$ denotes the filter with characteristic length Δ and $\langle Q\left(\boldsymbol{x},t\right)\rangle_{l}$ is the filtered value of $Q\left(\boldsymbol{x},t\right)$. The filter has the following properties:[57]

$$\mathcal{G}\left(\boldsymbol{x}',\boldsymbol{x}\right) = \mathcal{G}\left(\boldsymbol{x}'-\boldsymbol{x}\right), \qquad (2.19a)$$

$$\mathcal{G}\left(\boldsymbol{x}\right) = \mathcal{G}\left(-\boldsymbol{x}\right), \qquad (2.19b)$$

$$\int_{-\infty}^{\infty}\mathcal{G}\left(\boldsymbol{x}\right)\mathrm{d}\boldsymbol{x}' = 1, \qquad (2.19c)$$

which imply spatial invariance, symmetry, and normalization properties, respectively. In variable density flows, it is convenient to consider the Favré (density-weighted) filtered values,

$$\langle f\rangle_{L} = \frac{\langle\rho f\rangle_{l}}{\langle\rho\rangle_{l}}. \qquad (2.20)$$

Applying the filtering operation to Eqs. (2.1)–(2.4) and (2.6) yields

$$\frac{\partial\langle\rho\rangle_{l}}{\partial t} + \frac{\partial\langle\rho\rangle_{l}\langle u_{i}\rangle_{L}}{\partial x_{i}} = 0, \qquad (2.21)$$

$$\frac{\partial\langle\rho\rangle_{l}\langle u_{j}\rangle_{L}}{\partial t} + \frac{\partial\langle\rho\rangle_{l}\langle u_{j}\rangle_{L}\langle u_{i}\rangle_{L}}{\partial x_{i}} = -\frac{\partial\langle p\rangle_{l}}{\partial x_{j}} + \frac{\partial\langle\tau_{ij}\rangle_{L}}{\partial x_{i}} - \frac{\partial\mathcal{T}_{ij}}{\partial x_{i}}, \qquad (2.22)$$

$$\frac{\partial\langle\rho\rangle_{l}\langle\phi_{\alpha}\rangle_{L}}{\partial t} + \frac{\partial\langle\rho\rangle_{l}\langle u_{i}\rangle_{L}\langle\phi_{\alpha}\rangle_{L}}{\partial x_{i}} = -\frac{\partial\langle J_{i}^{\alpha}\rangle_{L}}{\partial x_{i}} - \frac{\partial\mathcal{M}_{i}^{\alpha}}{\partial x_{i}} + \langle\rho S_{\alpha}\rangle_{l}, \qquad (2.23)$$

$$\frac{\partial\langle\rho\rangle_{l}\langle h\rangle_{L}}{\partial t} + \frac{\partial\langle\rho\rangle_{l}\langle u_{i}\rangle_{L}\langle h\rangle_{L}}{\partial x_{i}} = -\frac{\partial\langle q_{i}\rangle_{L}}{\partial x_{i}} + \frac{\partial\langle p\rangle_{l}}{\partial t} + \langle u_{i}\rangle_{L}\frac{\partial\langle p\rangle_{l}}{\partial x_{i}}$$
$$+ \langle\tau_{ij}\rangle_{L}\frac{\partial\langle u_{i}\rangle_{L}}{\partial x_{j}} - \frac{\partial\mathcal{H}_{i}}{\partial x_{i}} + \mathcal{P} + \Gamma, \qquad (2.24)$$

$$\frac{\partial\langle\rho\rangle_{l}\langle E\rangle_{L}}{\partial t} + \frac{\partial\langle\rho\rangle_{l}\langle u_{i}\rangle_{L}\langle E\rangle_{L}}{\partial x_{i}} = -\frac{\partial\langle p\rangle_{l}\langle u_{i}\rangle_{L}}{\partial x_{i}} - \frac{\partial\langle q_{i}\rangle_{L}}{\partial x_{i}} + \frac{\partial\langle\tau_{ij}\rangle_{L}\langle u_{i}\rangle_{L}}{\partial x_{j}}$$
$$- \frac{\partial}{\partial x_{i}}\left(\gamma c_{v}\mathcal{Q}_{i} + \frac{1}{2}\mathcal{J}_{i} - \mathcal{D}_{i}\right). \qquad (2.25)$$

8

The unclosed terms are the SGS stress, $\mathcal{T}_{ij}$; SGS mass flux, $\mathcal{M}_i^\alpha$; SGS heat flux, $\mathcal{H}_i$; SGS convected pressure gradient, $\mathcal{P}$; SGS viscous heating, Γ; SGS temperature flux, $\mathcal{Q}_i$; SGS turbulent diffusion, $\mathcal{J}_i$; and SGS viscous dissipation, $\mathcal{D}_i$:

$$\mathcal{T}_{ij} = \langle \rho \rangle_l \left(\langle u_i u_j \rangle_L - \langle u_i \rangle_L \langle u_j \rangle_L \right), \tag{2.26}$$

$$\mathcal{M}_i^\alpha = \langle \rho \rangle_l \left(\langle u_i \phi_\alpha \rangle_L - \langle u_i \rangle_L \langle \phi_\alpha \rangle_L \right), \tag{2.27}$$

$$\mathcal{H}_i = \langle \rho \rangle_l \left[\langle u_i h \rangle_L - \langle u_i \rangle_L \langle h \rangle_L \right], \tag{2.28}$$

$$\mathcal{P} = \left\langle u_i \frac{\partial p}{\partial x_i} \right\rangle_l - \langle u_i \rangle_L \frac{\partial \langle p \rangle_l}{\partial x_i}, \tag{2.29}$$

$$\Gamma = \left\langle \tau_{ij} \frac{\partial u_i}{\partial x_j} \right\rangle_l - \langle \tau_{ij} \rangle_L \frac{\partial \langle u_i \rangle_L}{\partial x_j}, \tag{2.30}$$

$$\mathcal{Q}_i = \langle \rho \rangle_l \left(\langle u_i T \rangle_L - \langle u_i \rangle_L \langle T \rangle_L \right), \tag{2.31}$$

$$\mathcal{J}_i = \langle \rho \rangle_l \left(\langle u_i u_j u_j \rangle_L - \langle u_i \rangle_L \langle u_j u_j \rangle_L \right), \tag{2.32}$$

$$\mathcal{D}_i = \langle \sigma_{ji} u_j \rangle_L - \langle \sigma_{ji} \rangle_L \langle u_j \rangle_L. \tag{2.33}$$

In chemically-reacting flows, the chemical source term, $\langle \rho S_\alpha \rangle_l$, also requires a closure. The following approximations are made in deriving Eqs. (2.21)–(2.25):

$$\frac{\partial \langle \tau_{ij} \rangle_l}{\partial x_i} \approx \frac{\partial \langle \tau_{ij} \rangle_L}{\partial x_i} = \frac{\partial}{\partial x_i} \left[2\mu \langle S_{ij} \rangle_L - \frac{2}{3} \mu \langle S_{nn} \rangle_L \delta_{ij} \right], \tag{2.34}$$

$$\frac{\partial}{\partial x_i} \left(-\gamma \frac{\partial \langle \phi_\alpha \rangle_l}{\partial x_i} \right) \approx \frac{\partial}{\partial x_i} \left(-\gamma \frac{\partial \langle \phi_\alpha \rangle_L}{\partial x_i} \right), \tag{2.35}$$

$$\frac{\partial}{\partial x_i} \left(-\gamma \frac{\partial \langle h \rangle_l}{\partial x_i} \right) \approx \frac{\partial}{\partial x_i} \left(-\gamma \frac{\partial \langle h \rangle_L}{\partial x_i} \right), \tag{2.36}$$

$$\frac{\partial \langle q_i \rangle_l}{\partial x_i} \approx -\frac{\partial}{\partial x_i} \left[\lambda \frac{\partial \langle T \rangle_L}{\partial x_i} - \gamma \sum_{\alpha=1}^{N_s} \Delta h_\alpha^\circ \frac{\partial \langle \phi_k \rangle_L}{\partial x_i} \right]$$
$$\approx -\frac{\partial}{\partial x_i} \left[\gamma \frac{\partial \langle h \rangle_L}{\partial x_i} \right], \tag{2.37}$$

where the Favré-filtered strain rate is approximated by:

$$\langle S_{ij} \rangle_L \approx \frac{1}{2} \left(\frac{\partial \langle u_i \rangle_L}{\partial x_j} + \frac{\partial \langle u_j \rangle_L}{\partial x_i} \right). \tag{2.38}$$

The filtered equation of state is:

$$\langle p \rangle_l = \langle \rho \rangle_l \langle RT \rangle_L$$
$$\approx \langle \rho \rangle_l \langle R \rangle_L \langle T \rangle_L, \tag{2.39}$$

$$\langle R \rangle_L = \langle \phi_\alpha \rangle_L \frac{\mathcal{R}}{W_\alpha}. \tag{2.40}$$

2.1.3 Subgrid Scale Closure

The subgrid scale (SGS) stress is modeled with the modified Smagorinsky[58] turbulent viscosity closure of Yoshizawa,[59,60]

$$\mathcal{T}_{ij} = -2\mu_t \langle S_{ij} \rangle_L + \frac{2}{3}\mu_t \langle S_{nn} \rangle_L \delta_{ij} + \frac{2}{3} \langle \rho \rangle_l \langle \kappa \rangle_L \delta_{ij}, \tag{2.41}$$

where the subgrid viscosity and isotropic part of the subgrid stress are

$$\mu_t = \langle \rho \rangle_l C_v \Delta^2 \sqrt{\langle S_{ij} \rangle_L \langle S_{ij} \rangle_L}, \tag{2.42}$$

$$\langle \kappa \rangle_L = C_I \Delta^2 \langle S_{ij} \rangle_L \langle S_{ij} \rangle_L, \tag{2.43}$$

respectively and $C_I = 0.18$ and $C_v = 0.04$ are model constants.[61] The eddy-viscosity closure is used to model the SGS mass and enthalpy fluxes:

$$\frac{\partial \mathcal{M}_i^\alpha}{\partial x_i} = -\frac{\partial}{\partial x_i}\left[\gamma_t \frac{\partial \langle \phi_\alpha \rangle_L}{\partial x_i} \right], \tag{2.44}$$

$$\frac{\partial \mathcal{H}_i}{\partial x_i} = -\frac{\partial}{\partial x_i}\left[\gamma_t \frac{\partial \langle h \rangle_L}{\partial x_i} \right], \tag{2.45}$$

where the subgrid diffusivity is $\gamma_t = \mu_t/Sc_t$. The turbulent Prandtl and Schmidt numbers are taken to be equivalent and constant: $Pr_t = Sc_t = 0.7$. The SGS convected pressure gradient, $\mathcal{P}$, and viscous heating, Γ, are neglected. The eddy-viscosity model is used to close the SGS heat flux:

$$\mathcal{Q}_j = -\frac{\lambda_t}{c_p}\frac{\partial \langle T \rangle_L}{\partial x_j}, \quad \lambda_t = \frac{\mu_t c_p}{Pr_t}. \tag{2.46}$$

Both the turbulent diffusion, $\mathcal{J}_j$, and viscous dissipation, $\mathcal{D}_j$, are neglected.

The energy, E, and enthalpy, h, carry overlapping, but not identical, information. The conservative numerical discretizations used in US3D require the use of E as the transported thermodynamic variable, while solution of the SFMDF for SGS closure of the chemical source term as described below necessitates the use of h. US3D solves Eq. (2.25); the FDF scheme solves Eq. (2.24). As shown in Appendix A, these two transport equations are consistent, with the assumption:

$$\frac{\partial}{\partial x_i}\left[\gamma_t \frac{\partial \langle h \rangle_L}{\partial x_i} \right] - \langle u_n \rangle_L \frac{\partial \mathcal{T}_{in}}{\partial x_i} + \frac{1}{2}\left[\frac{\partial \mathcal{T}_{nn}}{\partial t} + \frac{\partial \langle u_i \rangle_L \mathcal{T}_{nn}}{\partial x_i} \right] = \lambda_t \frac{\partial}{\partial x_i}\frac{\partial \langle T \rangle_L}{\partial x_i}. \tag{2.47}$$

No attempt is made to validate this assumption.

2.1.4 Filtered Density Function

The filtered chemical source term $\langle \rho S_\alpha \rangle_l$ is closed via the scalar filtered mass density function (SFMDF), defined as[17]

$$F\left(\boldsymbol{\psi}; \boldsymbol{x}, t\right) = \int_{-\infty}^{\infty} \rho(\boldsymbol{x}', t)\zeta[\boldsymbol{\psi}; \boldsymbol{\phi}(\boldsymbol{x}', t)]G\left(\boldsymbol{x}' - \boldsymbol{x}\right)d\boldsymbol{x}', \qquad (2.48)$$

where $\boldsymbol{\psi} = [\psi_1, \ldots, \psi_{N_h}]$ denotes the sample-space variables for the scalar array, $\boldsymbol{\phi}$. The fine-grained density, ζ, is defined as[62]

$$\zeta[\boldsymbol{\psi}; \boldsymbol{\phi}(\boldsymbol{x}', t)] = \delta(\boldsymbol{\psi} - \boldsymbol{\phi}(\boldsymbol{x}', t)) = \prod_{\alpha=1}^{N_h} \delta(\psi_\alpha - \phi_\alpha(\boldsymbol{x}', t)). \qquad (2.49)$$

Equation (2.48) implies that the SFMDF is the mass-weighted, spatially-filtered value of the fine-grained density. We define the conditional expectation as

$$\begin{aligned} \langle Q\left(\boldsymbol{x}, t\right) \,|\, \boldsymbol{\psi} \rangle &= \langle Q\left(\boldsymbol{x}, t\right) \,|\, \boldsymbol{\phi}\left(\boldsymbol{x}, t\right) = \boldsymbol{\psi} \rangle \\ &= \frac{\int_{-\infty}^{+\infty} \rho\left(\boldsymbol{x}', t\right) Q\left(\boldsymbol{x}', t\right) \zeta\left[\boldsymbol{\psi}, \boldsymbol{\phi}\left(\boldsymbol{x}', t\right)\right] G\left(\boldsymbol{x} - \boldsymbol{x}'\right) d\boldsymbol{x}'}{F\left(\boldsymbol{\psi}; \boldsymbol{x}, t\right)}. \end{aligned} \qquad (2.50)$$

The SFMDF has the following properties:

$$\int_{-\infty}^{+\infty} F\left(\boldsymbol{\psi}; \boldsymbol{x}, t\right) d\boldsymbol{\psi} = \int_{-\infty}^{+\infty} \rho\left(\boldsymbol{x}', t\right) \zeta[\boldsymbol{\psi}; \boldsymbol{\phi}(\boldsymbol{x}', t)]G\left(\boldsymbol{x} - \boldsymbol{x}'\right) d\boldsymbol{x}' = \langle \rho\left(\boldsymbol{x}, t\right) \rangle_l. \quad \text{(i)}$$

If $Q\left(\boldsymbol{x}, t\right) = \hat{Q}\left(\boldsymbol{\phi}\left(\boldsymbol{x}, t\right)\right)$, then

$$\langle Q\left(\boldsymbol{x}, t\right) \,|\, \boldsymbol{\psi} \rangle = \hat{Q}\left(\boldsymbol{\psi}\right), \qquad \text{(ii)}$$

and

$$\int_{-\infty}^{+\infty} \langle Q\left(\boldsymbol{x}, t\right) \,|\, \boldsymbol{\psi} \rangle F\left(\boldsymbol{\psi}; \boldsymbol{x}, t\right) d\boldsymbol{\psi} = \langle \rho Q \rangle_l. \qquad \text{(iii)}$$

The chemical source term is considered to be a known function of the scalar array, $S_\alpha\left(\boldsymbol{x}, t\right) = \hat{S}_\alpha\left(\boldsymbol{\phi}\right)$; therefore, the SFMDF provides closure of the filtered chemical source term:

$$\int_{-\infty}^{+\infty} \hat{S}_\alpha\left(\boldsymbol{\psi}\right) F\left(\boldsymbol{\psi}; \boldsymbol{x}, t\right) d\boldsymbol{\psi} = \langle \rho S_\alpha \rangle_l. \qquad (2.51)$$

The transport equation for the SFMDF is derived by assuming $\rho\left(\boldsymbol{x}, t\right) = \rho\left(\boldsymbol{\phi}\right)$ and expanding the total derivative of the fine-grained density:

$$\frac{\partial \rho \zeta}{\partial t} + \frac{\partial \rho u_i \zeta}{\partial x_i} = -\frac{\partial \zeta}{\partial \psi_i}\left[\frac{\partial \rho \phi_i}{\partial t} + \frac{\partial \rho u_j \phi_i}{\partial x_j}\right]. \qquad (2.52)$$

Substituting Eqs. (2.23)–(2.24) into the RHS of Eq. (2.52),

$$\frac{\partial \rho \zeta}{\partial t} + \frac{\partial \rho u_i \zeta}{\partial x_i} = -\frac{\partial \zeta}{\partial \psi_\alpha}\left[\frac{\partial}{\partial x_i}\left(\gamma \frac{\partial \phi_\alpha}{\partial x_i}\right) + \rho S_\alpha(\boldsymbol{\phi})\right]$$
$$-\frac{\partial \zeta}{\partial \psi_{N_h}}\left[\frac{\partial}{\partial x_i}\left(\gamma \frac{\partial h}{\partial x_i}\right) + \frac{\partial p}{\partial t} + u_i \frac{\partial p}{\partial x_i} + \tau_{ij}\frac{\partial u_i}{\partial x_j}\right]. \quad (2.53)$$

Multiplying Eq. (2.53) by $G(\boldsymbol{x}' - \boldsymbol{x})$, integrating over $\boldsymbol{x}' \in (-\infty, \infty)$, and assuming filtering and differentiation commute yields

$$\frac{\partial F}{\partial t} + \boxed{\frac{\partial \langle u_i \,|\, \boldsymbol{\psi}\rangle F}{\partial x_i}} = -\boxed{\frac{\partial}{\partial \psi_k}\left[\left\langle \frac{1}{\hat{\rho}(\boldsymbol{\phi})}\frac{\partial}{\partial x_i}\left(\gamma \frac{\partial \phi_k}{\partial x_i}\right)\,\middle|\, \boldsymbol{\psi}\right\rangle F\right]} - \boxed{\frac{\partial \langle L_h \,|\, \boldsymbol{\psi}\rangle F}{\partial \psi_{N_h}}} - \frac{\partial S_\alpha(\boldsymbol{\psi}) F}{\partial \psi_\alpha},$$
$$(2.54)$$

where

$$L_h = \frac{1}{\rho}\left[\frac{\partial p}{\partial t} + u_i \frac{\partial p}{\partial x_i} + \tau_{ij}\frac{\partial u_i}{\partial x_j}\right], \quad (2.55)$$

and boxed terms due to SGS convection, mixing, and compressibility require closures. The SGS convection is modeled via

$$\frac{\partial \langle u_i \,|\, \boldsymbol{\psi}\rangle F}{\partial x_i} = \frac{\partial}{\partial x_i}\left[\langle u_i \rangle_L F\right] - \frac{\partial}{\partial x_i}\left(\gamma_t \frac{\partial (F/\langle \rho \rangle_l)}{\partial x_i}\right).$$

SGS mixing is closed using the interaction by exchange with the mean (IEM) model:[63,64]

$$-\frac{\partial}{\partial \psi_i}\left[\frac{F}{\hat{\rho}}\left\langle \frac{\partial}{\partial x_j}\left(\gamma \frac{\partial \phi_i}{\partial x_j}\right)\,\middle|\, \boldsymbol{\psi}\right\rangle\right] = \frac{\partial}{\partial x_i}\left(\gamma \frac{\partial (F/\hat{\rho})}{\partial x_i}\right) + \frac{\partial}{\partial \psi_i}\left[\Omega_m F\left(\psi_i - \langle \phi_i \rangle_L\right)\right].$$

The effect of SGS compressibility is neglected:

$$\frac{\partial \langle L_h \,|\, \boldsymbol{\psi}\rangle F}{\partial \psi_{N_h}} \approx \frac{\partial}{\partial \psi_{N_h}}\left[\frac{1}{\langle \rho \rangle_l}\left[\frac{\partial \langle p \rangle_l}{\partial t} + \langle u_i \rangle_L \frac{\partial \langle p \rangle_l}{\partial x_i} + \langle \tau_{ij} \rangle_L \frac{\partial \langle u_i \rangle_L}{\partial x_j}\right] F\right].$$

With these assumptions, the modeled SFMDF transport equation becomes:

$$\frac{\partial F}{\partial t} + \frac{\partial (\langle u_i \rangle_L F)}{\partial x_i} = \frac{\partial}{\partial x_i}\left[(\gamma + \gamma_t)\frac{\partial (F/\langle \rho \rangle_l)}{\partial x_i}\right] + \frac{\partial}{\partial \psi_\alpha}\left[\Omega_m F\left(\psi_\alpha - \langle \phi_\alpha \rangle_L\right)\right]$$
$$-\frac{\partial \langle L_h \rangle_L F}{\partial \psi_{N_h}} - \frac{\partial S_\alpha(\boldsymbol{\psi}) F}{\partial \psi_\alpha}, \quad (2.56)$$

where

$$\langle L_h \rangle_L = \frac{1}{\langle \rho \rangle_l}\left(\frac{\partial \langle p \rangle_l}{\partial t} + \langle u_i \rangle_L \frac{\partial \langle p \rangle_l}{\partial x_i} + \langle \tau_{ij} \rangle_L \frac{\partial \langle u_i \rangle_L}{\partial x_j}\right). \quad (2.57)$$

2.2   SFMDF IN US3D

The SFMDF essentially represents the single-point joint probability density function (PDF) of N_h random variables. Numerical solution of the SFMDF requires discretization in $(N_h + 4)$-dimensional space. This is impractical for large values of N_h, as is the case with a large number of chemical species. Using the principle of equivalent systems, an affordable Lagrangian Monte Carlo (MC) technique is employed instead.[65,66] A set of stochastic differential equations (SDEs) are formulated whose Fokker-Planck equation represents the modeled SFMDF transport equation.[67,68] The modeled SDEs are:

$$dX_i = \left[\langle u_i \rangle_L + \frac{1}{\langle \rho \rangle_l} \frac{\partial}{\partial x_i} (\gamma + \gamma_t) \right] dt + \sqrt{\frac{2(\gamma + \gamma_t)}{\langle \rho \rangle_l}} dW_i, \tag{2.58}$$

$$d\psi_\alpha = -\Omega_m (\psi_\alpha - \langle \phi_\alpha \rangle_L) dt + S_\alpha(\boldsymbol{\psi}), \tag{2.59}$$

$$d\psi_h = -\Omega_m (\psi_h - \langle h \rangle_L) dt + \frac{1}{\langle \rho \rangle_l} \left[\frac{\partial \langle p \rangle_l}{\partial t} + \langle u_i \rangle_L \frac{\partial \langle p \rangle_l}{\partial x_i} + \langle \tau_{ij} \rangle_L \frac{\partial \langle u_i \rangle_L}{\partial x_j} \right] dt, \tag{2.60}$$

where X_i, ψ_α, and ψ_h represent sample space variables for x_i, ϕ_α, and h, respectively. The Fokker-Planck equation corresponding to Eqs. (2.58)–(2.60) is

$$\begin{aligned} \frac{\partial F}{\partial t} + \frac{\partial \langle u_i \rangle_L F}{\partial x_i} &= \frac{\partial}{\partial x_i} \left[(\gamma + \gamma_t) \frac{\partial (F/\langle \rho \rangle_l)}{\partial x_i} \right] \\ &+ \frac{\partial}{\partial \psi_\alpha} \left[\Omega_m (\psi_\alpha - \langle \phi_\alpha \rangle_L) F \right] - \frac{\partial S_\alpha F}{\partial \psi_\alpha} - \frac{\partial L_h F}{\partial \psi_h}. \end{aligned} \tag{2.61}$$

Transport equations for each of the filtered scalars, $\langle \phi_k \rangle_L$, is derived by multiplying Eq. (2.61) by $\psi_k, k \in [1, \ldots, N_h]$ and integrating over sample-space $\boldsymbol{\psi} = [\psi_1, \ldots, \psi_{N_h}]$:

$$\frac{\partial \langle \rho \rangle_l \langle \phi_\alpha \rangle_L}{\partial t} + \frac{\partial \langle \rho \rangle_l \langle u_i \rangle_L \langle \phi_\alpha \rangle_L}{\partial x_i} = \frac{\partial}{\partial x_i} \left[(\gamma + \gamma_t) \frac{\partial \langle \phi_\alpha \rangle_L}{\partial x_i} \right] + \langle \rho \rangle_l \langle S_\alpha \rangle_L, \tag{2.62}$$

$$\begin{aligned} \frac{\partial \langle \rho \rangle_l \langle h \rangle_L}{\partial t} + \frac{\partial \langle \rho \rangle_l \langle u_i \rangle_L \langle h \rangle_L}{\partial x_i} &= \frac{\partial}{\partial x_i} \left[(\gamma + \gamma_t) \frac{\partial \langle h \rangle_L}{\partial x_i} \right] + \frac{\partial \langle p \rangle_l}{\partial t} \\ &+ \langle u_i \rangle_L \frac{\partial \langle p \rangle_l}{\partial x_i} + \langle \tau_{ij} \rangle_L \frac{\partial \langle u_i \rangle_L}{\partial x_j}. \end{aligned} \tag{2.63}$$

The US3D computer code solves for cell-centered values of the filtered variables on unstructured tetrahedral and quadrilateral elements. The viscous terms are evaluated via a second-order equivalent weighted least squares approximation, similar to

Table 1: Ensemble sizes for the Monte Carlo solver.

Label	Ensemble Type	Nominal Particles Per Cell
E1	Cell	30
E2	Largest sphere contained within cell	30
E3	Sphere with half radius of largest sphere	100

that in central difference schemes.[69,70] The convective terms are evaluated by a hybrid flux-splitting. A symmetric sixth-order interpolation is used to reconstruct the convective fluxes in smooth regions of the flow.[69] Near the sharp gradients, the flux approximation smoothly reverts to a Steger-Warming splitting scheme with second-order MUSCL reconstruction.[71] The form of the convective flux is $F = F_c + \kappa F_{diss}$, in which F is the total flux at a face center, F_c is a sixth-order central reconstruction, F_{diss} is the Steger-Warming effective dissipation operator, and κ is the shock sensor of Ducros et al.[72] Time-integration is via an explicit third-order Runge-Kutta scheme.

The solution of the SFMDF requires integration of the SDEs in Eqs. (2.58)–(2.60). These are treated using the Euler-Maruyamma approximation.[17,73] A large number of realizations of the SDEs are simulated by overlaying the US3D finite volume domain with a set of notional MC particles. To reconstruct the SFMDF, an ensemble of MC particles within a spatial control volume Ω is assembled. Theoretically, we require $|\Omega| \to 0$, and $N_p \to \infty$, where N_p is the number of particles in the ensemble set. In practice, the ensemble domain is approximated by a geometric shape of finite size containing a finite number of particles. Table 1 shows the ensemble sizes considered. The transport equations for all of the first-order filtered equations and the second-order SGS moments, $\tau(\phi, \phi) = \langle \phi \phi \rangle_L - \langle \phi \rangle_L \langle \phi \rangle_L$, are also solved via US3D. The source terms in these equations are obtained from the SFMDF. The MC solution of the SDEs operates synchronously with the FV solver.[74] The FV solver requires the filtered source terms, $\langle S_\alpha \rangle_L$, at the cell centers. For integration of the SDEs, the MC solver requires the filtered hydrodynamic variables at each

14

of the particle locations. For this, a second-order interpolation scheme is employed that uses the cell-centered values and gradients to reconstruct the velocity at each particle location. The filtered terms corresponding to compressibility are taken from the center of the cell surrounding the particle. An efficient method is constructed to track each particle within the volume. There is a certain level of redundancy inherent in the hybrid scheme in that the first two filtered moments are available from both FV and MC solvers. This redundancy facilitates consistency assessment of the computational methodology.

2.3   DEMONSTRATION

The hybrid SFMDF-US3D solver is employed for LES of a three-dimensional, temporally-developing mixing layer.[75–78] In this layer, the stream-wise, cross-stream, and span-wise directions are denoted by $\{x, y, z\}$, with the corresponding velocities $\{u, v, w\}$. The temporal mixing layer consists of two parallel streams traveling in opposite directions with the same speed on a cube-shaped domain with length L. The flow is periodic in the streamwise and spanwise directions. The cross-stream boundaries are treated as slip walls. The length L is specified such that $L = 2^{N_P}\lambda_u$, where N_P is the desired number of successive vortex pairings and λ_u is the wavelength of the most unstable mode corresponding to the mean streamwise velocity profile imposed at the initial time. Transport of a passive scalar, ϕ, is considered. Both the filtered stream-wise velocity and passive scalar fields are initialized with hyperbolic tangent profiles, where $\langle u \rangle_L = U_r$, $\langle \phi \rangle_L = 1$ on the top stream, $\langle u \rangle_L = -U_r$, $\langle \phi \rangle_L = 0$ on the bottom stream, and U_r is the reference velocity. In these simulations, the Reynolds number is $Re = U_r L_r/\nu = 50$ and the Mach number is $Ma = U_r/\sqrt{\gamma R T_r}$, where T_r is the constant temperature at which the entire field is initialized and $L_r = \delta_v(t=0)/2$ is the reference length, taken to be one-half of the initial vorticity thickness. The vorticity thickness is defined as $\delta_v = U_r/ \left| \partial \langle u \rangle_L /\partial y \right|_{max}$. Initial perturbations are used to expedite the formation of large-scale vortical structures. Both two- and three-dimensional perturbations are added with a random phase shift between the

15

Table 2: Grid parameters for resolution assessments.

Label	Element Type	Number of Cells
G1	Hexahedral	32,768
G2	Tetrahedral	113,832
G3	Hexahedral	125,000
G4	Hexahedral	474,552

three-dimensional modes.[79] These perturbations yield vortex pairings and strong three-dimensionality.

Simulations are conducted of a subsonic ($Ma = 0.2$) and a supersonic ($Ma = 3$) layer for both reacting and non-reacting cases. For reacting cases, a one-step reaction of the form $A + B \rightarrow 2P$ is used with reactant conversion rate $S_A = -k_r \phi_A \phi_B$, where k_r is the reaction rate constant and ϕ_X is the mass fraction of species X. The field is initialized with $\langle \phi_A \rangle_L = \langle \phi \rangle_L$, $\langle \phi_B \rangle_L = 1 - \langle \phi \rangle_L$. The reactants are considered thermodynamically identical and the product is thermodynamically similar to the reactants, with a lower enthalpy of formation to simulate exothermic reaction. The reaction rate constant is parametrized by the Damköhler number, $Da = k_r \rho_r / (U_r/L_r)$, where the reference density, ρ_r, is taken to be the initial density of the fluid at the cross-stream boundaries. Simulations are conducted with slow ($Da = 10$) and fast ($Da = 10^6$) reactions. The reaction exothermicity is paremetrized by the nondimensional heat release, $Ce = -\Delta h_P^0 / (c_p T_0) = 2$, where Δh_P^0 is the heat of reaction. Transport of the passive scalar, $\langle \phi \rangle_L$, is considered in both MC and FV solvers.

Simulations are conducted on the meshes shown in Table 2. The hexahedral grids are uniformly spaced in all directions and the tetrahedral mesh is shown in Fig. 1. To assess the effects of grid resolution, simulations are conducted on the four meshes, G1 to G4. The MC particles are initially distributed uniformly throughout the domain with variable weights to maintain consistency with the filtered fluid density field.[80] Due to flow periodicity in the streamwise and spanwise directions, particles that

leave the domain at one of these boundaries are replaced by new particles introduced at the opposite boundary with the same velocity and scalar values. In the cross-stream directions, the free-slip boundary condition is satisfied by mirror-reflection of particles contacting these boundaries. For calculations of filtered quantities from the MC solver (*e.g.* $\langle\phi\rangle_L$), the particles are averaged according to the ensembles specified in Table 1. A sensitivity analysis is performed to assess the effect of ensemble size (E1 to E3) on the results. Unless otherwise noted, simulations are conducted on grid G1 and ensemble E1. Reynolds-averaged results are obtained by ensemble-averaging along the homogeneous directions of flow. Reynolds-averaged values are denoted by $\overline{\phi}$ and their Favre-averages by $\widetilde{\phi} = \overline{\rho\phi}/\overline{\rho}$. The resolved second-order moments are denoted by $R(\phi,\phi) = \langle\phi\phi\rangle_L - \langle\phi\rangle_L\langle\phi\rangle_L$ and the total second-order moments are denoted by $r(\phi,\phi) = \widetilde{\phi\phi} - \widetilde{\phi}\widetilde{\phi}$.

First, we consider the non-reacting, subsonic temporal mixing layer. To demonstrate visual consistency of the MC and FV solvers, contour plots of the instantaneous filtered values of the conserved scalar, $\langle\phi\rangle_L$, are shown in Fig. 2. The layer displays strong three-dimensionality, primary vortex rollup in the spanwise plane, and secondary instabilities in the streamwise plane. Further consistency validation is demonstrated in the scatter plots of $\langle\phi\rangle_L$ via FV *vs.* $\langle\phi\rangle_L$ via MC as shown in Fig. 3. The Reynolds-averaged values for the first moment of the scalar are shown in Fig. 4. These values compare well with each other and also with previous direct numerical simulation (DNS) data.[1] The second moments of the conserved scalar for various ensemble sizes are shown in Figs. 5–7. As expected, when the ensemble size is decreased, the second moments converge to the FV results. The total second moment (Fig. 7) compares well with DNS results and is consistently calculated on the MC and FV solvers. A grid resolution study is performed to determine the sensitivity of accuracy and consistency to mesh spacing. As shown in Figs. 8–10, the first and second moments converge to the finest mesh and agree well with DNS.

In the reacting case, consistency of the MC solver and realizability of the simulated results are investigated. Consistency is confirmed by the scatter plots of the first moments of the product and temperature as shown in Figs. 11–12. The Reynolds-averaged values for the first moment of the product mass fraction are

shown in Fig. 13 and show good consistency between FV and MC solvers. Realizability is confirmed in Figs. 14–15 where first moments of temperature and mass fraction via MC are compared with pure mixing and infinitely fast reaction boundary lines. For further assessment of the realizability, a conserved scalar Shvab-Zeldovich variable,[81]

$$Z = Y_A + \frac{c_p}{-2\Delta h_p^0} (T - T_r), \tag{2.64}$$

is compared with the passive scalar in Fig. 16 and yields an excellent agreement.

Simulations are performed of a supersonic non-reacting temporal mixing layer with $Ma = 3$. At high Mach numbers, turbulent mixing is inhibited by compressibility.[82] The formation of large- and small-scale vortical structures is retarded because the layer does not respond significantly to initial perturbations. For this reason, we increase the initial forcing amplitude to enhance structure growth. The supersonic layer displays the formation of eddy shocklets identified by regions with sharp density and pressure gradients. An instantaneous frontal view of the contours of the conserved scalar with shadowgraph in the background showing shocklets is displayed in Fig. 17. This figure also shows the ability of both the FV and MC schemes to capture the shocklets. Large variations in density exist and are captured consistently by FV and MC solvers as shown in Fig. 18. The consistency of the conserved scalar and density first moments is further demonstrated in the scatter plots shown in Figs. 19–20. In aggregate, these results are particularly encouraging as they demonstrate that the hybrid SFMDF-US3D solver is capable of conducting LES of shock-dominated flows.

Finally, simulations are performed of a $Ma = 3$ chemically-reacting supersonic mixing layer with $Da = 10^6$. Conserved scalar, total energy, and density first moment scatter plots are displayed in Figs. 21–23 and demonstrate consistency. The Reynolds-averaged values of temperature via FV and MC are shown in Fig. 24 and compare well.

18

2.4 CHAPTER SUMMARY

The scalar filtered mass density function (SFMDF) methodology is implemented into the US3D computer code. This code is an unstructured FV solver and has been very effective for large eddy simulation of compressible flows. The resulting hybrid SFMDF-US3D method is employed for LES of a temporally developing mixing layer. The consistency and the accuracy of the methodology is demonstrated via simulations of low and high Mach number flows for both non-reacting and chemically-reacting configurations. In particular it is shown that the scheme is capable of accurate simulation of shock dominated flows. The US3D-SFMDF code is now ready for LES of flows of interest in practical hypersonic propulsion systems.
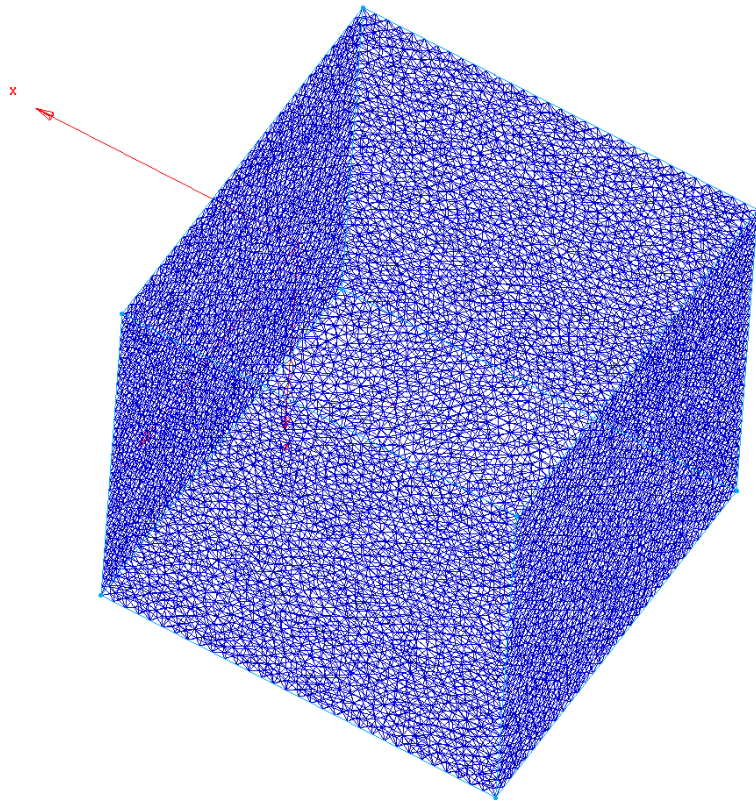
Figure 1: Unstructured tetrahedral mesh.
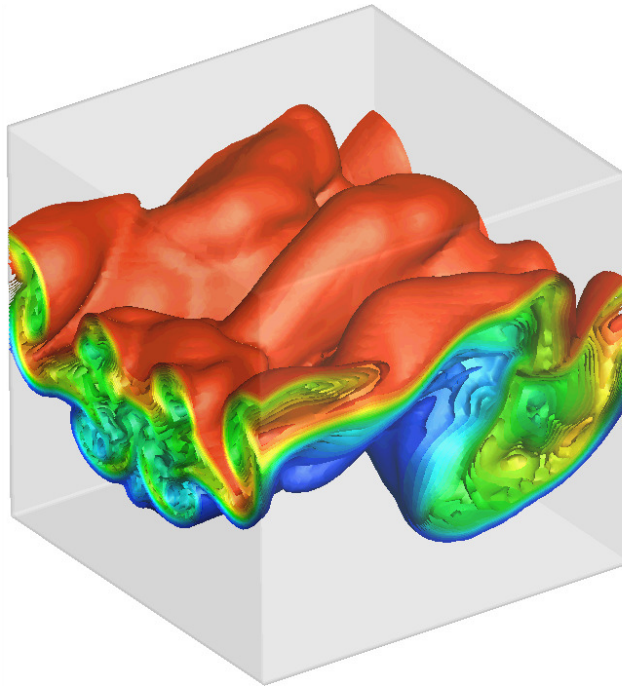
(a) $\langle\phi\rangle_L$ via FV
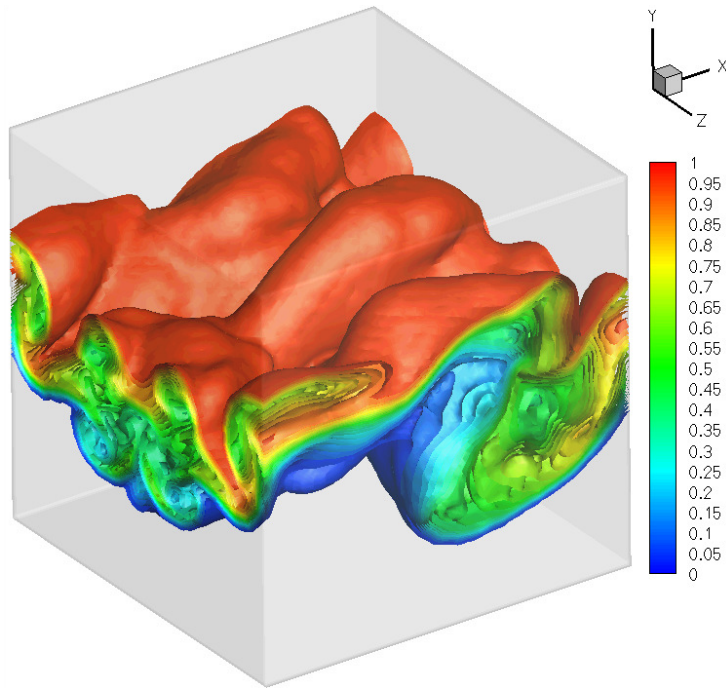
(b) $\langle\phi\rangle_L$ via MC

Figure 2: Contours of the conserved scalar for $Ma = 0.2$ non-reacting layer.

Figure 3: Scatter plot of the filtered values of the conserved scalar for the $Ma = 0.2$ non-reacting layer on grid G4. The correlation coefficient is 0.99916. Red 45° line shown for comparison.
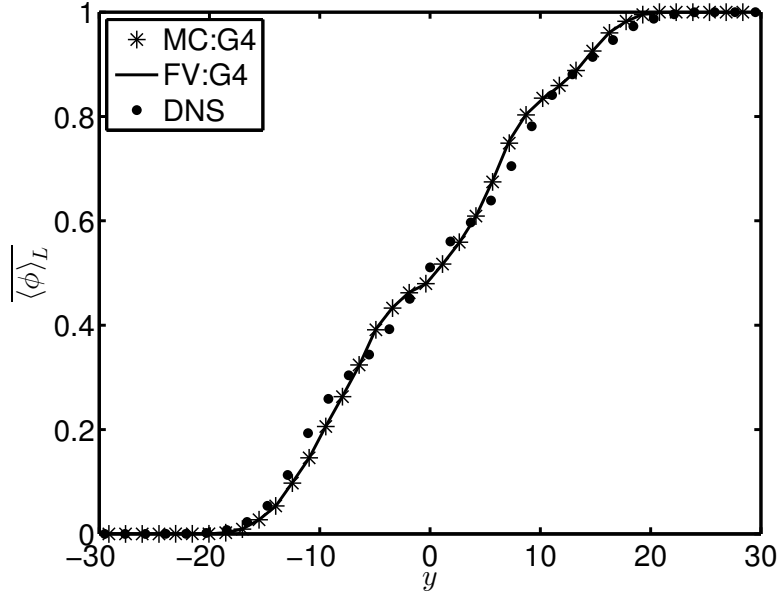
Figure 4: Cross-stream variation of the Reynolds-averaged values of the resolved scalar mean at $t = 80$ for $Ma = 0.2$ non-reacting layer. The solid line denotes LES-FV predictions, asterisks denote FDF-MC, and circles denote DNS data.[1]
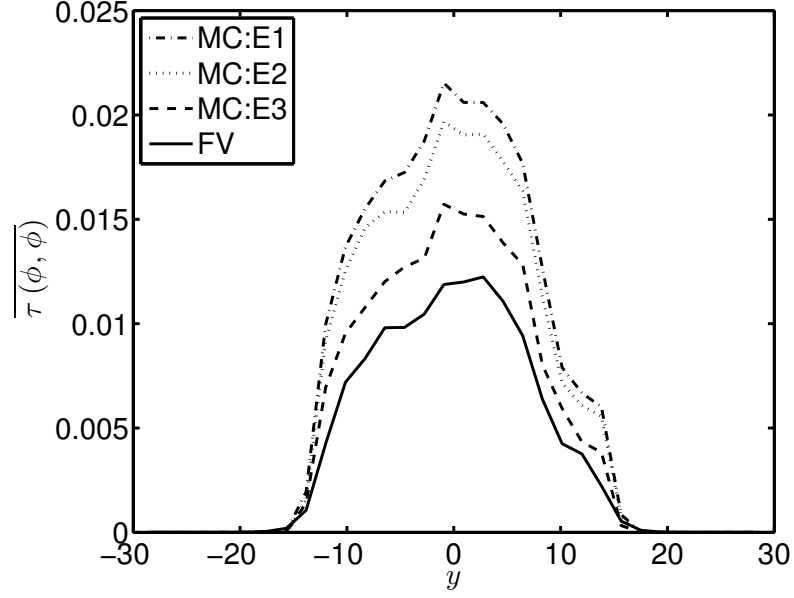
Figure 5: Cross-stream variation of the Reynolds-averaged SGS scalar variance at $t = 80$ for $Ma = 0.2$ non-reacting layer. The solid line denotes LES-FV results and the other lines denote FDF-MC predictions using various ensemble sizes (Table 1).
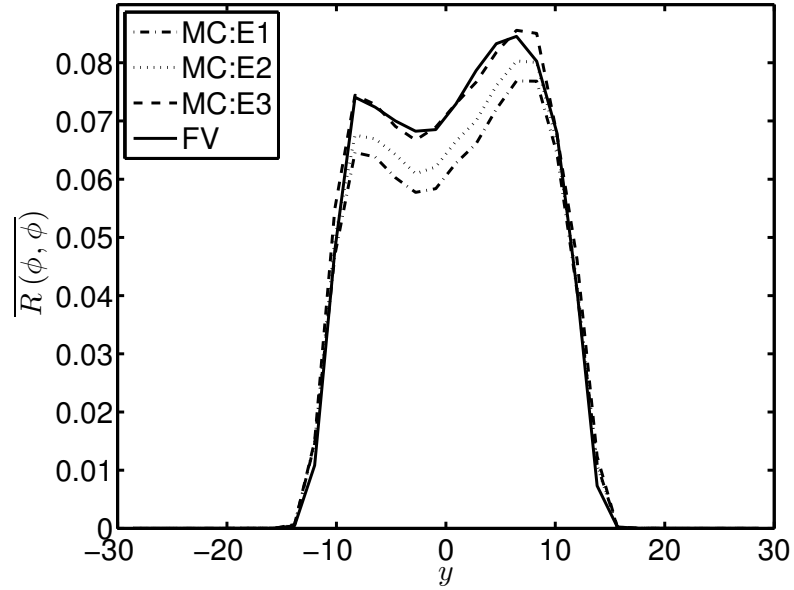
Figure 6: Cross-stream variation of the Reynolds-averaged values of the resolved scalar variance at $t = 80$ for $Ma = 0.2$ non-reacting layer. The solid line denotes LES-FV predictions and other lines denote FDF-MC results using various ensemble sizes (Table 1).
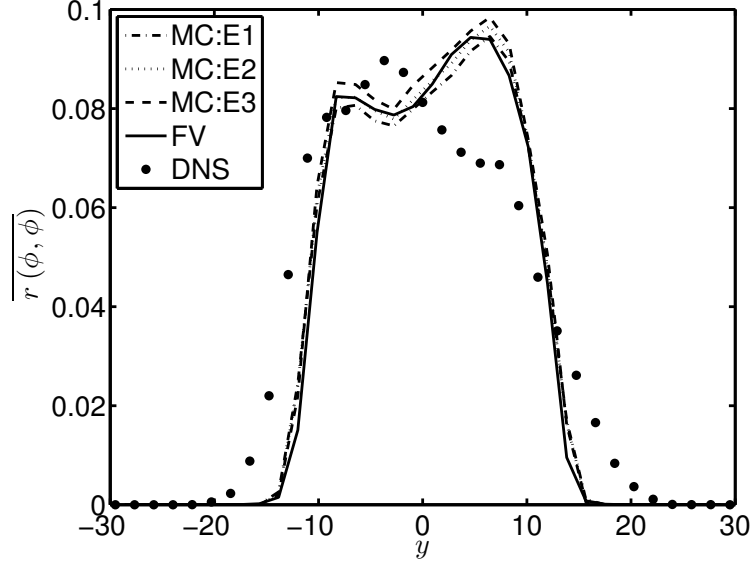
Figure 7: Cross-stream variation of the Reynolds-averaged values of the total scalar variance at $t = 80$ for $Ma = 0.2$ non-reacting layer. The solid line denotes LES-FV predictions and other lines denote FDF-MC results using various ensemble sizes (Table 1).
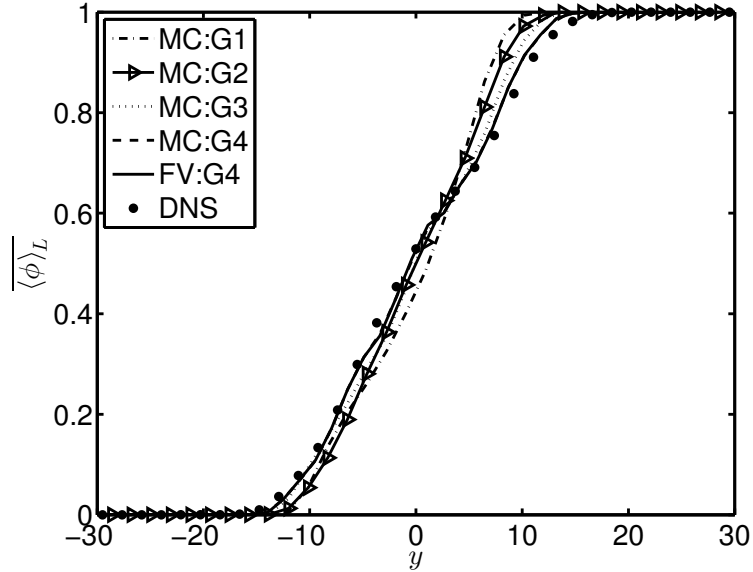
Figure 8: Cross-stream variation of the Reynolds-averaged values of the resolved scalar mean at $t = 60$ for $Ma = 0.2$ non-reacting layer. The solid line denotes LES-FV predictions on mesh G4 and other lines denote FDF-MC results on various meshes (Table 2).
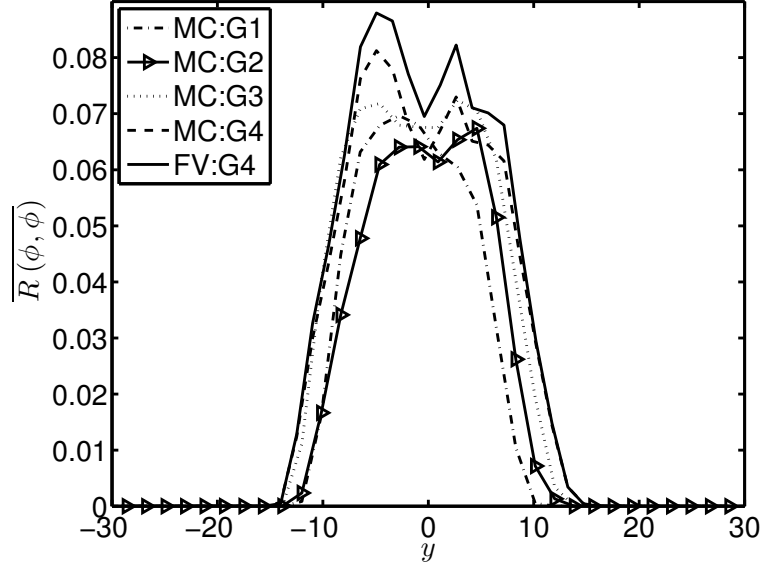
Figure 9: Cross-stream variation of the Reynolds-averaged values of the resolved scalar variance at $t = 60$ for $Ma = 0.2$ non-reacting layer. The solid line denotes LES-FV predictions on mesh G4 and other lines denote FDF-MC results on various meshes (Table 2).
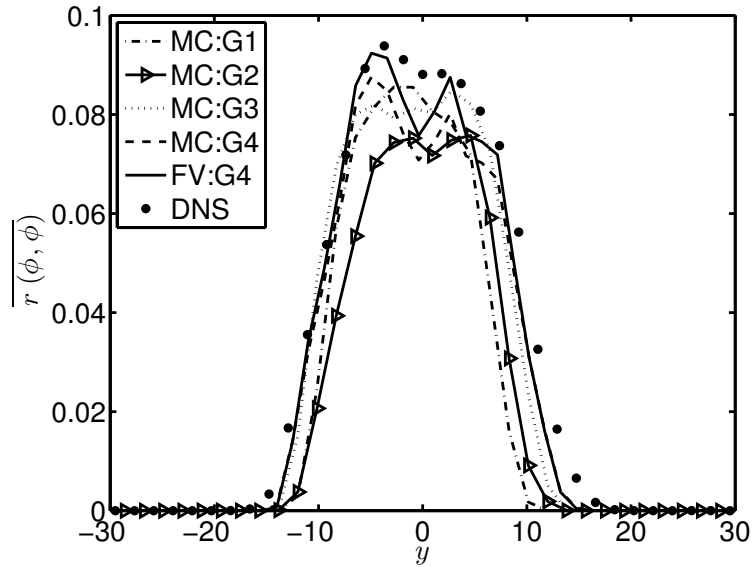
Figure 10: Cross-stream variation of the Reynolds-averaged values of the total scalar variance at $t = 60$ for $Ma = 0.2$ non-reacting layer. The solid line denotes LES-FV predictions on mesh G4 and other lines denote FDF-MC results on various meshes (Table 2).

25
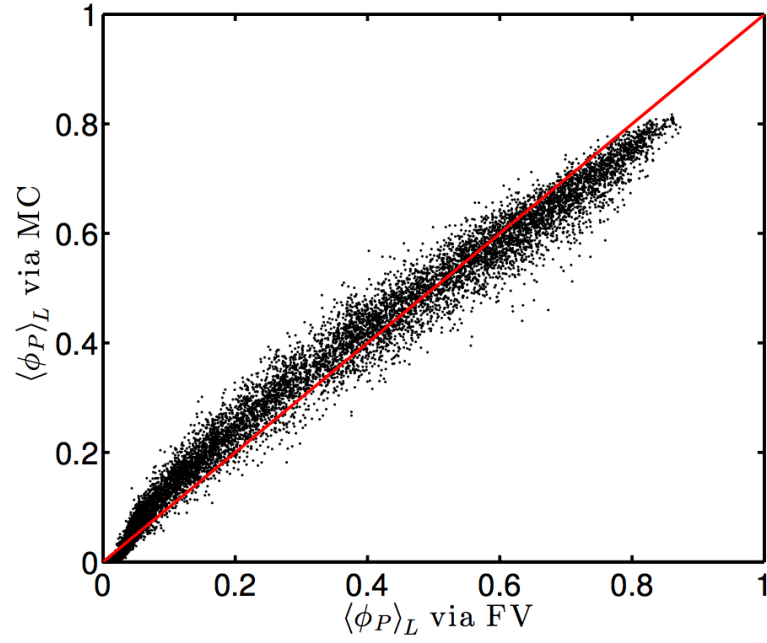
Figure 11: Scatter plot of filtered product formation for reacting $Ma = 0.2$ layer with $Da = 10$. Scatter points represent the quantity at a cell center as obtained from the FV and MC at $t = 80$.
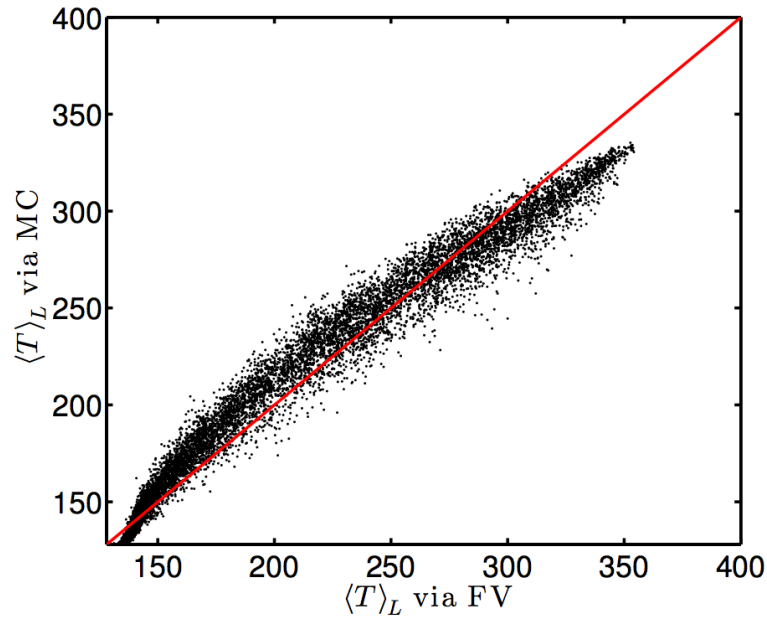
Figure 12: Scatter plot of filtered temperature for reacting $Ma = 0.2$ layer with $Da = 10$. Scatter points represent the quantity at a cell center as obtained from the FV and MC at $t = 80$.
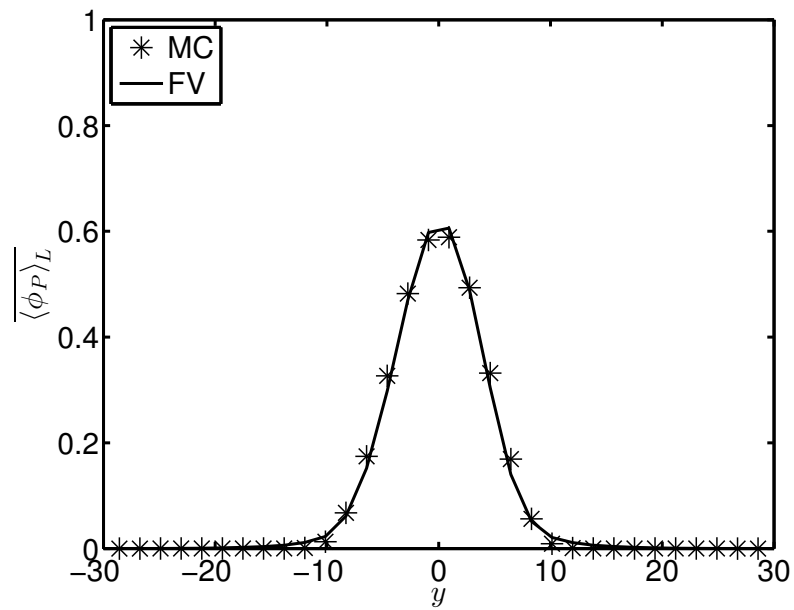
Figure 13: Cross-stream variation of the Reynolds-averaged values of the filtered product mass fraction at $t = 80$ for reacting $Ma = 0.2$ layer with $Da = 10$. Solid lines denote LES-FV predictions and asterisks denote MC results.
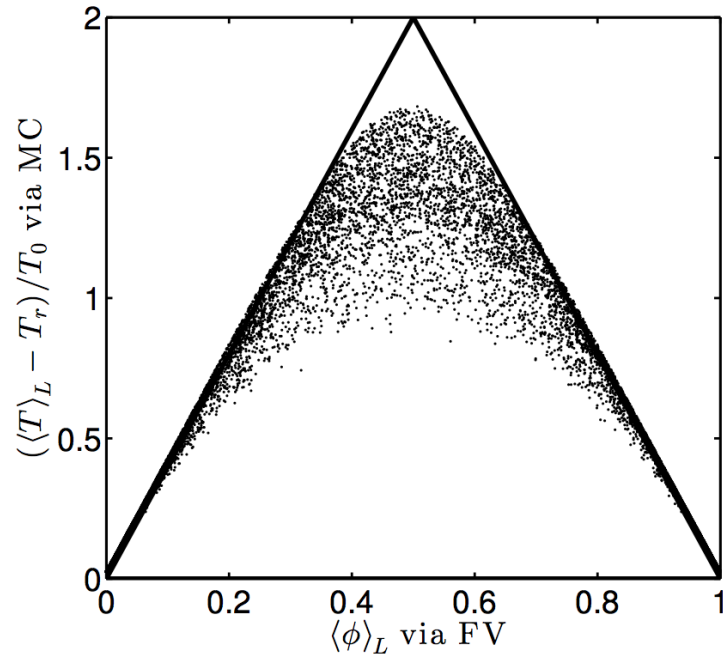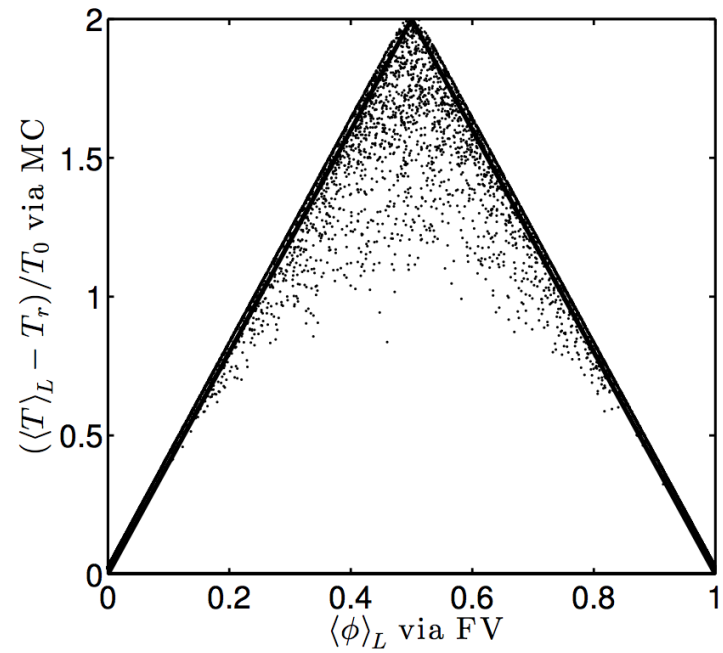
Figure 14: Scatter plots of filtered temperature *vs.* mixture fraction between the pure mixing and infinitely fast chemistry boundary lines. (a) $Da = 10$, (b) $Da = 10^6$
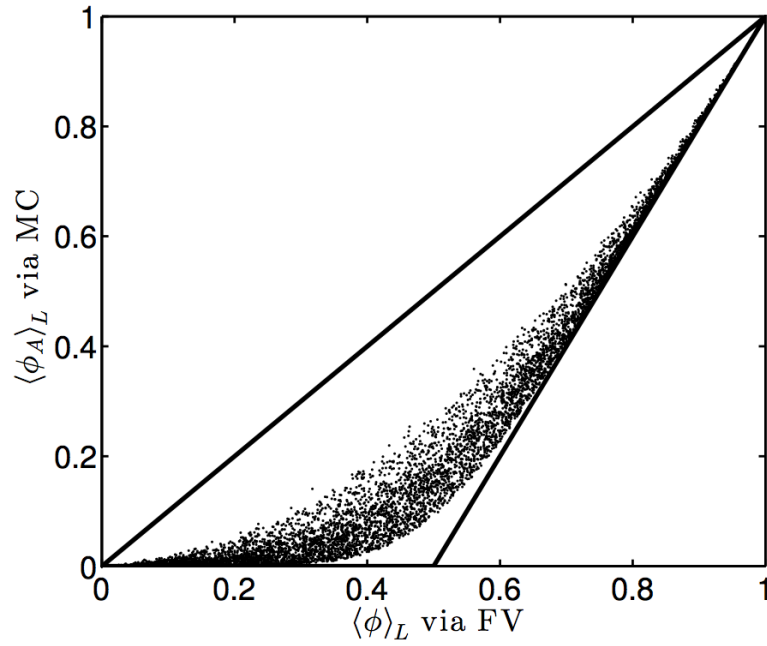
(a)
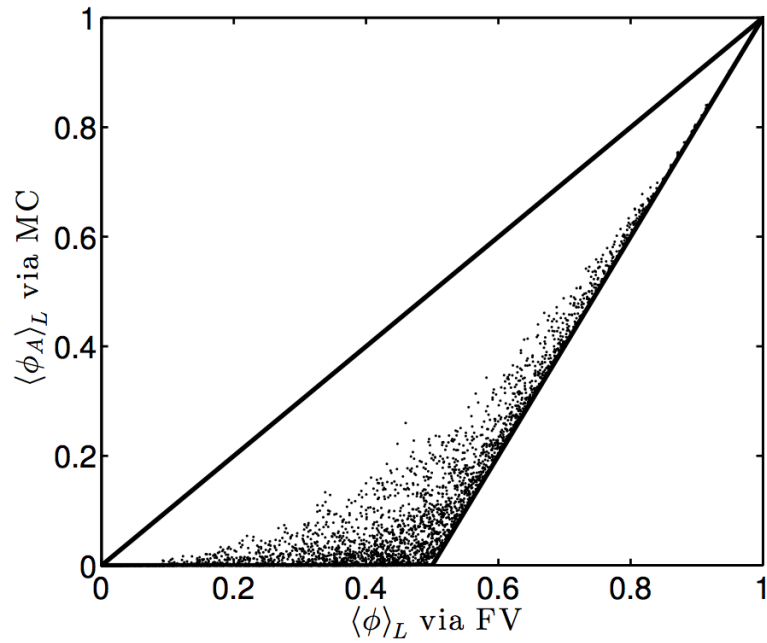
(b)

Figure 15: Scatter plots of filtered species mass fraction *vs.* the filtered mixture fraction between the pure mixing and the infinitely fast chemistry boundary lines. (a) $Da = 10$, (b) $Da = 10^6$.
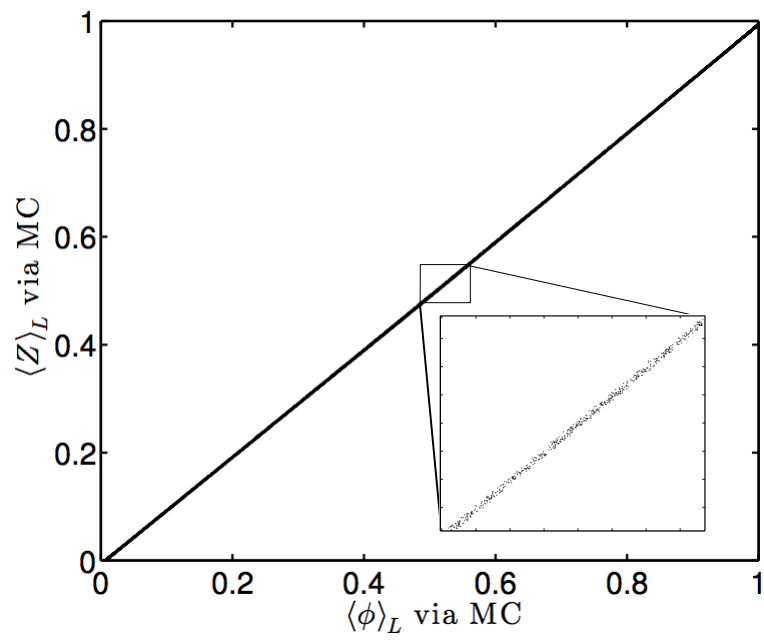
Figure 16: Scatter plots of the filtered conserved scalar *vs.* $\langle Z \rangle_L$ for $Da = 10^6$. Inset graph is magnification to display scatter. The correlation coefficient is 0.99999
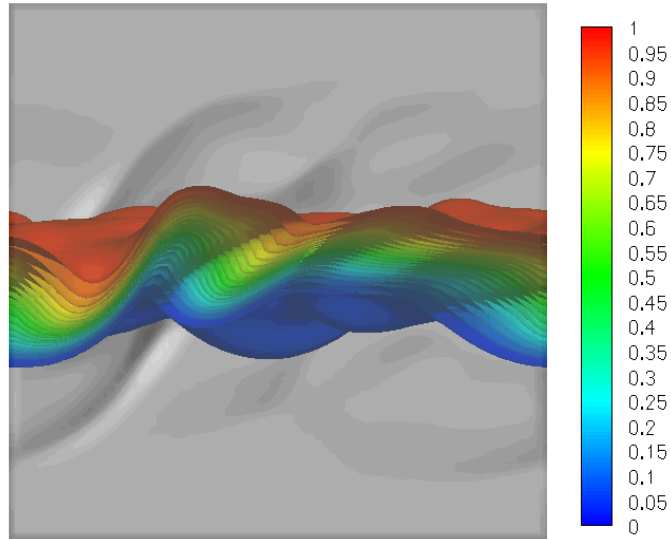
(a) FV
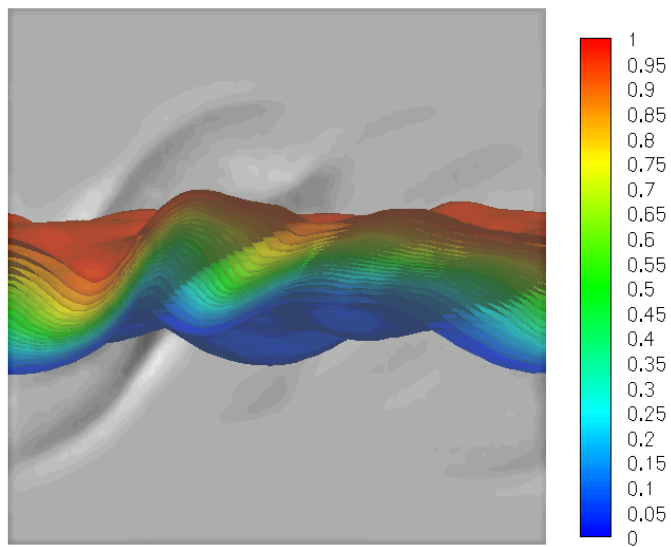
(b) MC

Figure 17: Contours of the filtered conserved scalar, $\langle\phi\rangle_L$, in foreground with shadowgraph showing eddy shocklets in background for $Ma = 3$ non-reacting layer from FV and MC.

31
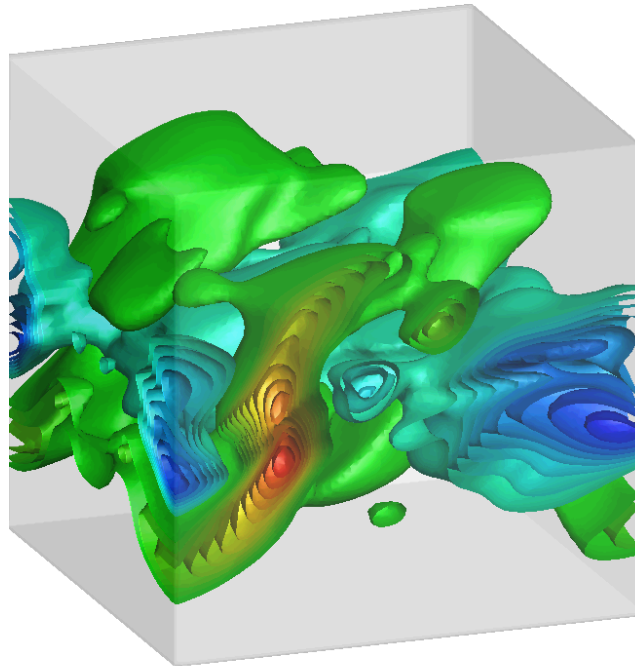
(a) FV
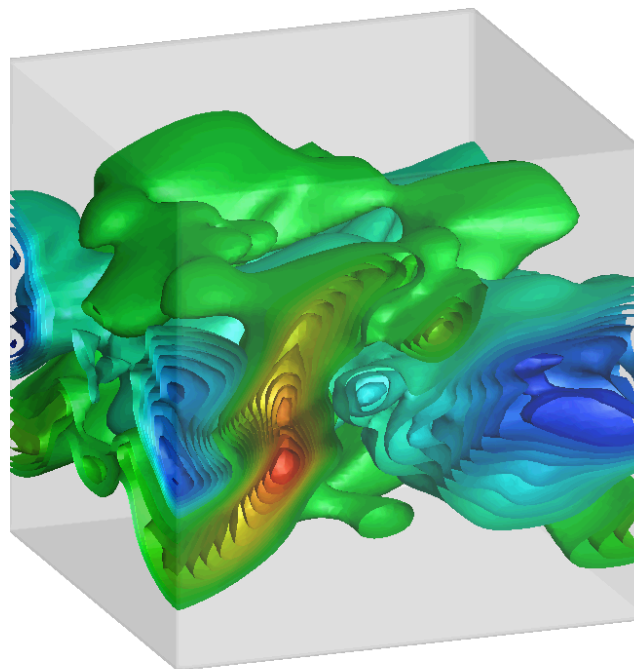
(b) MC
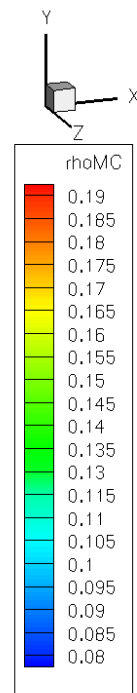
Figure 18: Contours of filtered density, $\langle\rho\rangle_l$, for $Ma = 3$ non-reacting layer from FV and MC.
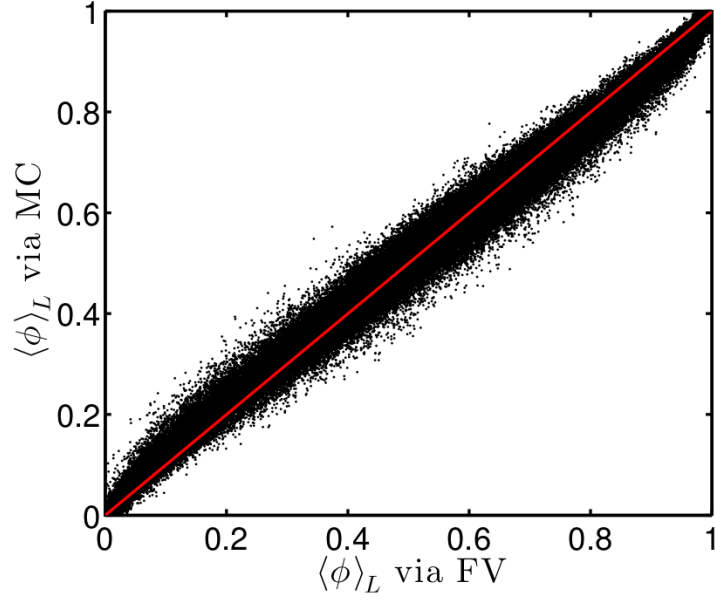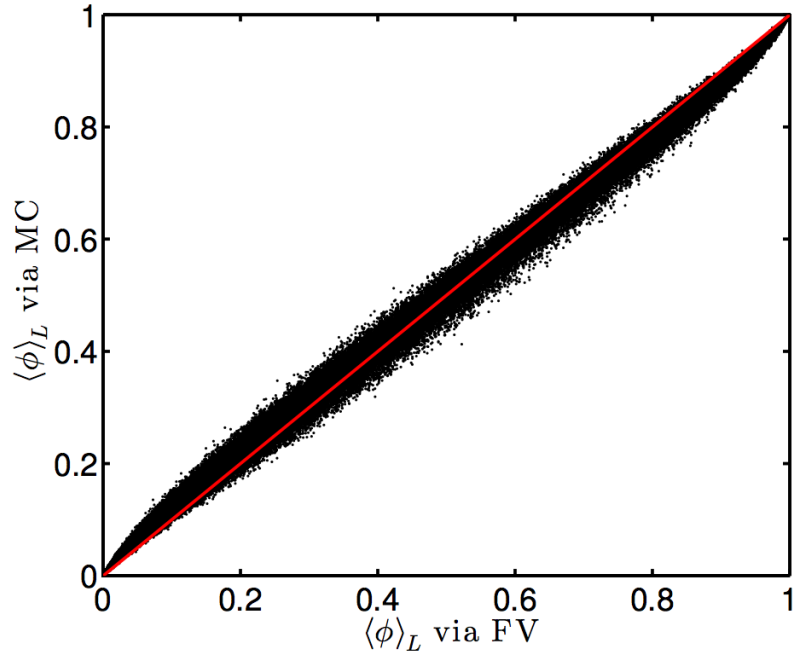
Figure 19: Scatter plot of the filtered values of the conserved scalar for $Ma = 3$ layer. The correlation coefficient is 0.99965. Red 45° line shown for comparison.
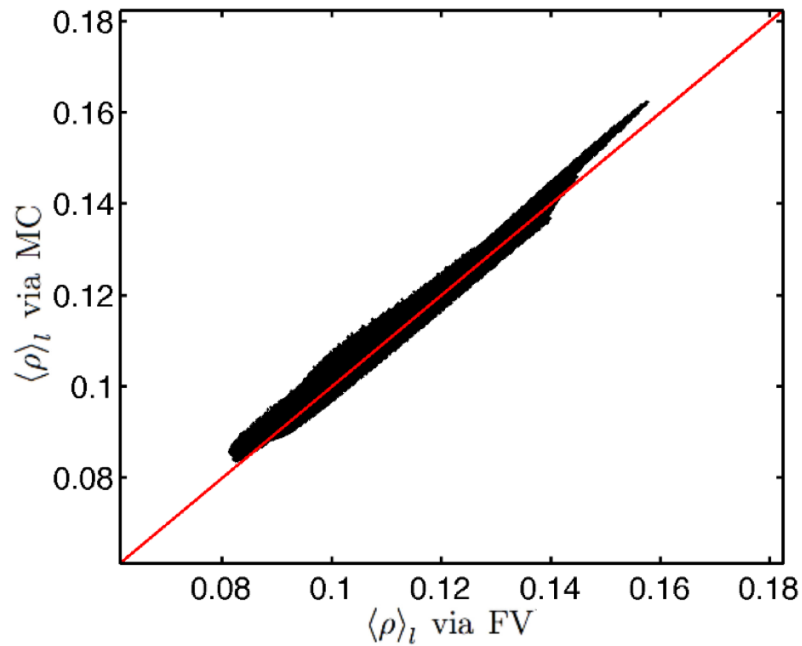

Figure 20: Scatter plot of the filtered values of density for $Ma = 3$ layer on mesh G4. The correlation coefficient is 0.99414. Red 45° line shown for comparison.
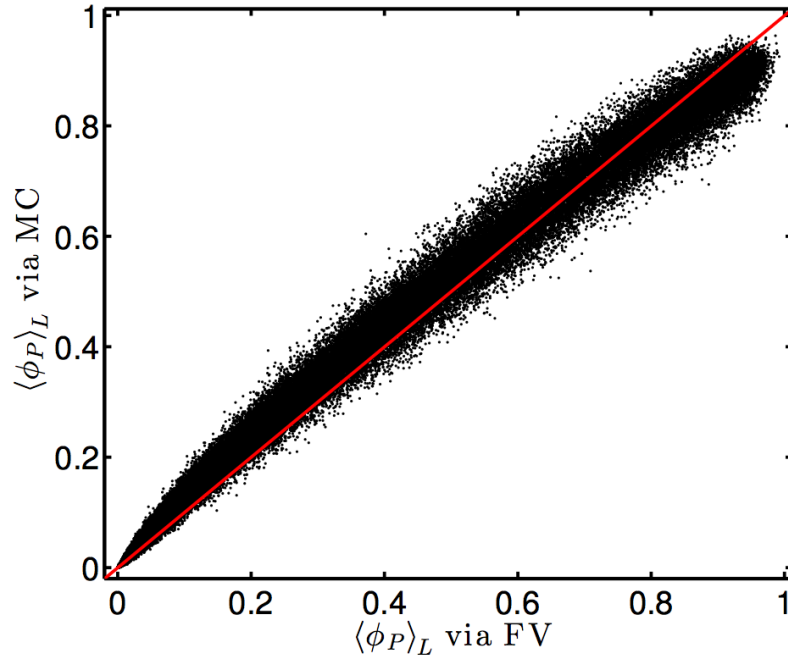
Figure 21: Scatter plot of filtered product formation for reacting $Ma = 3$ layer with $Da = 10^6$ on mesh G4. The correlation coefficient is 0.99610. Red 45° line shown for comparison.
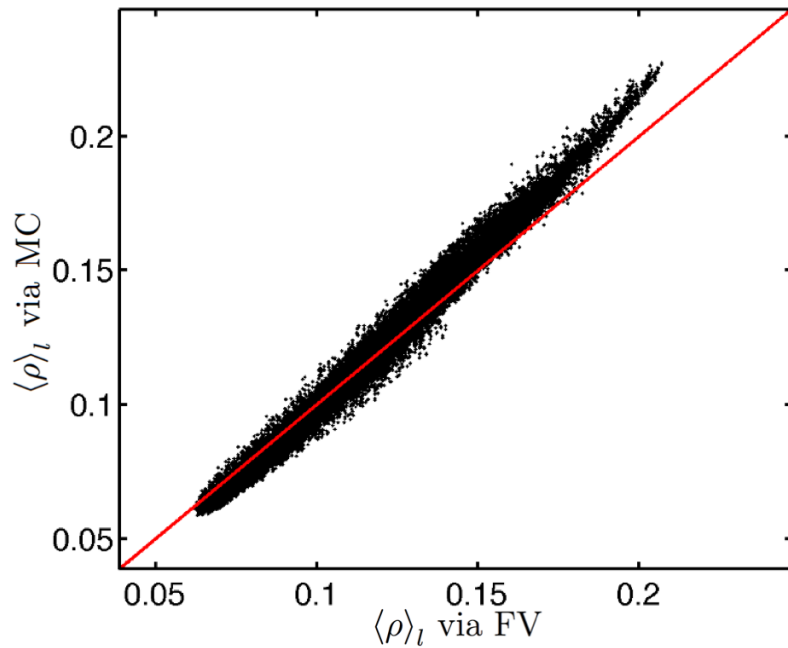
Figure 22: Scatter plot of filtered density for reacting $Ma = 3$ layer with $Da = 10^6$ on mesh G4. The correlation coefficient is 0.99413. Red 45° line shown for comparison.
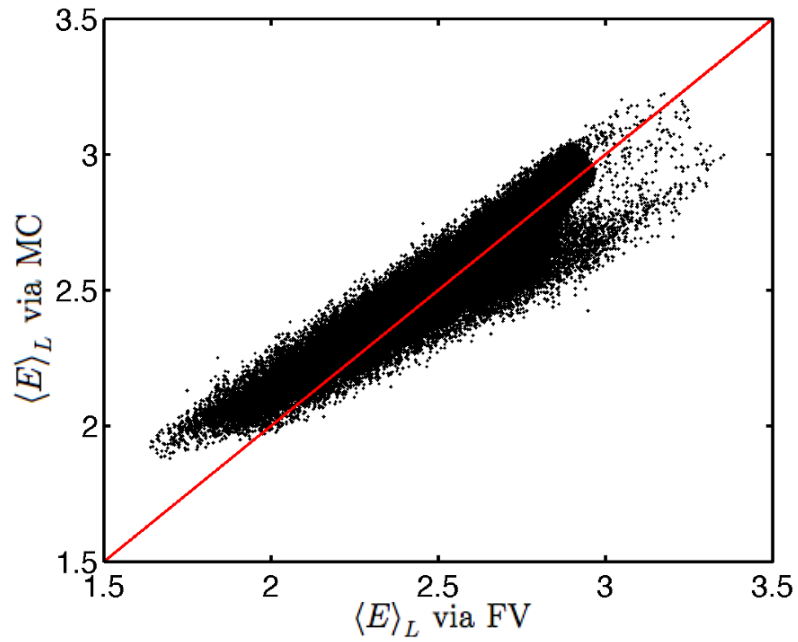
Figure 23: Scatter plot of filtered total energy for reacting $Ma = 3$ layer with $Da = 10^6$ on mesh G4. The correlation coefficient is 0.94697. Red 45° line shown for comparison.
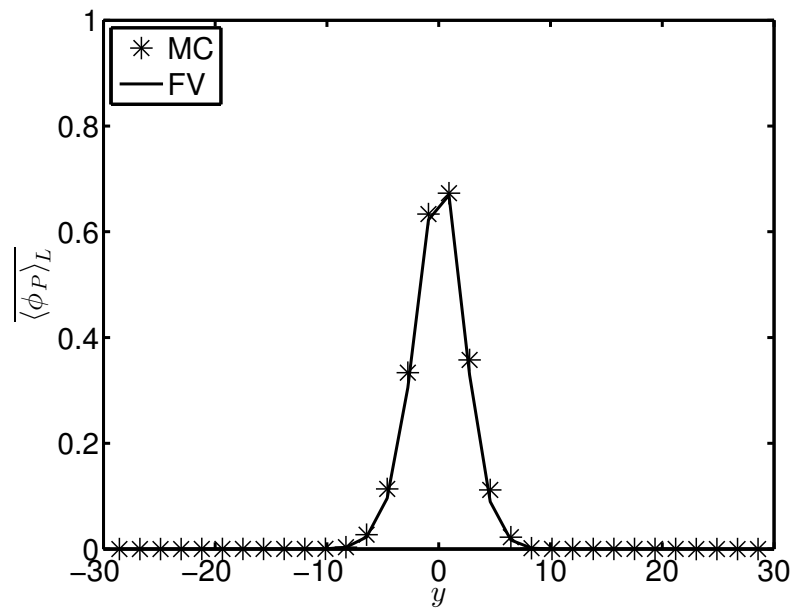
Figure 24: Cross-stream variation of the Reynolds-averaged values of the filtered temperature for $Ma = 3$ reacting layer with $Da = 10^6$ on mesh G4. Solid lines denote LES-FV predictions and asterisks denote MC results.

3.0 A MULTI-BLOCK ESWENO SCHEME

In this chapter, a new computational methodology is developed for accurate capturing of discontinuities in multi-block[83–85] finite difference simulations of hyperbolic partial differential equations. A fourth-order energy-stable weighted essentially non-oscillatory (ESWENO)[43–46] finite difference scheme on closed domains is combined with simultaneous approximation term (SAT)[47] weak interface and boundary conditions. Smoothness of grid-spacing across subdomain interfaces is not required. WENO stencil-biasing[37–40, 86, 87] is truncated near subdomain boundaries and only collocated interface points are communicated between neighboring subdomains. The performance of the methodology is assessed in the presence of significant jumps in grid-spacing across subdomain interfaces. Results are presented for several canonical test cases involving the linear scalar hyperbolic wave equation in one and two dimensions, and the Euler equations in one and two dimensions. It is demonstrated that the new methodology allows strong discontinuities to be passed across subdomain interfaces without a significant distortion. It is demonstrated that the methodology provides stable and accurate solutions even when large differences in the grid-spacing exist, whereas strong imposition of the interface conditions causes noticeable oscillations. With weak subdomain interdependence, low subdomain-to-subdomain message-passing overhead, and ease of local grid refinement, the new methodology is designed to be amenable to parallel simulations of flows in complex geometries.

3.1   FORMULATION

We consider the linear scalar hyperbolic wave equation on a finite (non-periodic) domain:

$$\frac{\partial v}{\partial t} + \frac{\partial f}{\partial x} = 0, \quad f = av, \quad x \in \Omega, \quad \Omega = [A, B],$$
$$v(x, 0) = v_0(x),$$
$$v(A, t) = g(t),$$

(3.1)

where $v = v\,(x, t)$ is the continuous solution; a, A, and B are positive constants; $v_0(x)$ and $g(t)$ are bounded continuous functions; and x and t are independent variables. To obtain an energy estimate, Eq. (3.1) is multiplied by v and integrated over the domain, Ω, which yields the continuous energy estimate,

$$\frac{d}{dt}\|v\|_{L_2}^2 = -a\left[v^2(B, t) - g^2(t)\right],$$

(3.2)

where $\|\cdot\|_{L_2}$ denotes the L_2 norm. Equation (3.2) admits a solution that is stable in time ($\frac{d}{dt}\|v\|_{L_2}^2 \leq 0$). Note that Eq. (3.2) is obtained by assuming that $\partial f/\partial x$ satisfies integration by parts (IBP).

The objective of the work in this chapter is to obtain a pth-order accurate finite difference approximation for the continuous spatial derivative in Eq. (3.1),

$$\frac{\partial \boldsymbol{f}}{\partial x} = \boldsymbol{D} \cdot \boldsymbol{f} + O(\Delta x^p),$$

(3.3)

such that a discrete energy estimate analogous to Eq. (3.2) can be obtained. In Eq. (3.3), $\boldsymbol{f}$ represents a projection of f onto a uniform N-point discretization of the Ω, $\boldsymbol{D}$ denotes a discrete derivative operator, and Δx denotes the constant grid-spacing of the discretization. The discrete solution of v is denoted by $\boldsymbol{u}$. Herein, bold variables represent discrete multicomponent arrays (vectors, matrices, *etc.*) and non-bold variables represent scalars or continuous variables. It is well-established

that in order to facilitate an energy estimate, $\boldsymbol{D}$ must satisfy summation by parts (SBP),[41,42] the discrete analog to IBP. SBP is embodied by the constraints,

$$\boldsymbol{D} = \boldsymbol{P}^{-1}(\boldsymbol{Q} + \boldsymbol{R}) \quad ; \quad \boldsymbol{Q} + \boldsymbol{Q}^T = Diag[-1, 0, ..., 0, 1], \tag{3.4}$$

$$\boldsymbol{R} = \boldsymbol{R}^T \quad ; \quad \boldsymbol{v}^T \boldsymbol{R} \boldsymbol{v} \geq 0, \quad \boldsymbol{v} \neq 0, \tag{3.5}$$

$$\boldsymbol{P} = \boldsymbol{P}^T \quad ; \quad \boldsymbol{v}^T \boldsymbol{P} \boldsymbol{v} > 0, \quad \boldsymbol{v} \neq 0, \tag{3.6}$$

that is, $\boldsymbol{Q}$ is almost skew-symmetric, $\boldsymbol{R}$ is symmetric positive semidefinite (SPS), and $\boldsymbol{P}$ is symmetric positive definite (SPD). To facilitate construction of an SPS matrix, we introduce the dissipation matrix, $\boldsymbol{R}$:

$$\boldsymbol{R} = \boldsymbol{\Lambda}_0 + \boldsymbol{\Delta}\boldsymbol{\Lambda}_1 \left[\boldsymbol{\Delta}\right]^T + \boldsymbol{\Delta} \left[\boldsymbol{\Delta}\right]^T \boldsymbol{\Lambda}_2 \boldsymbol{\Delta} \left[\boldsymbol{\Delta}\right]^T + \boldsymbol{\Delta} \left[\boldsymbol{\Delta}\right]^T \boldsymbol{\Delta}\boldsymbol{\Lambda}_3 \left[\boldsymbol{\Delta}\right]^T \boldsymbol{\Delta} \left[\boldsymbol{\Delta}\right]^T, \tag{3.7}$$

where the components $\boldsymbol{\Lambda}_i$ are diagonal SPS matrices of appropriate size,

$$\boldsymbol{\Lambda}_e = Diag \left[\lambda_1, ..., \lambda_N\right] \quad ; \quad \lambda_j \geq 0, \quad j = 1, N \quad ; \quad e = 2p, \quad p = 0, 1, \tag{3.8}$$

$$\boldsymbol{\Lambda}_o = Diag \left[\lambda_1, ..., \lambda_N\right] \quad ; \quad \lambda_j \geq 0, \quad j = 0, N \quad ; \quad o = 2p+1, \quad p = 0, 1, \tag{3.9}$$

and $\boldsymbol{\Delta}$ is the $N + 1 \times N$ differencing matrix,

$$\boldsymbol{\Delta} = \begin{bmatrix} -1 & 1 & 0 & 0 & 0 & 0 \\ 0 & -1 & 1 & 0 & 0 & 0 \\ 0 & 0 & \ddots & \ddots & 0 & 0 \\ 0 & 0 & 0 & -1 & 1 & 0 \\ 0 & 0 & 0 & 0 & -1 & 1 \end{bmatrix}. \tag{3.10}$$

These forms result in a semi-discrete energy equation that yields time-stability in the L_2 energy norm:[46]

$$\frac{d}{dt}\|\boldsymbol{u}\|_{\boldsymbol{P}} \leq 0, \tag{3.11}$$

where $\|\cdot\|_{\boldsymbol{P}}$ (e.g. $\|\boldsymbol{u}\|_{\boldsymbol{P}} = \boldsymbol{u}^T \boldsymbol{P} \boldsymbol{u}$) is the $\boldsymbol{P}$-norm, a discrete analog to the L_2 norm. Time-stability in the L_2 norm is hereafter referred to simply as *stability*.

3.1.1 Non-Oscillatory Schemes

We discretize the domain of Eq. (3.1) with two interdigitated grids:

$$\boldsymbol{x} = \left[x_1 = A, x_2, \ldots, x_N = B\right], \tag{3.12}$$

$$\bar{\boldsymbol{x}} = \left[\bar{x}_0 = A, \bar{x}_1, \ldots, \bar{x}_N = B\right]. \tag{3.13}$$

The finite difference grid-points, $\boldsymbol{x}$, are denoted *solution-points* because they carry the solution data. Each solution-point, x_i, lies in a control volume bounded on the left and right by *flux-points* $\bar{x}_{i-1}$ and $\bar{x}_i$, respectively. At each of these points, a numerical flux will be calculated to facilitate conservative calculation of the derivative. Data located at flux-points carry the overbar notation (*e.g.* $\bar{\boldsymbol{f}}$) while data located at solution-points are represented by variables without an overbar (*e.g.* $\boldsymbol{f}$). The flux- and solution-points are collocated at the boundaries. The solution-points are equally-spaced, while the flux-points may be unevenly-spaced between solution points.

The conventional fourth-order WENO finite difference scheme[3,88] for Eq. (3.1) is written in a semi-discrete form,

$$\frac{\partial u_i}{\partial t} + \frac{\overline{f}_i - \overline{f}_{i-1}}{\Delta x} = 0, \tag{3.14}$$

where $\bar{f}_i$ is the WENO flux given by

$$\bar{\boldsymbol{f}} = \sum_r \bar{w}^{(r)} \bar{\boldsymbol{f}}^{(r)}, \tag{3.15}$$

and $\bar{\boldsymbol{f}}^{(r)} = \boldsymbol{\mathcal{I}}^{(r)} \boldsymbol{f}$, $r \in \{L, C, R\}$ are second-order fluxes obtained by interpolating data from the solution-points to the flux-points for the three candidate stencils S^L, S^C, and S^R (left, center, and right stencils, respectively). As described in Ref. [46], the interpolation operators $\boldsymbol{\mathcal{I}}^{(r)}$ are $N+1 \times N$ matrices that interpolate data from the solution-points to the flux-points.

The nonlinear weight functions, $\bar{w}^{(r)}$, embody the stencil-biasing mechanics of the WENO scheme. The classical weight functions of Jiang and Shu[88] are defined,

$$\bar{w}^{(r)} = \frac{\bar{\alpha}^{(r)}}{\sum_r \bar{\alpha}^{(r)}}, \quad \bar{\alpha}^{(r)} = \frac{\bar{d}^{(r)}}{(\epsilon + \bar{\beta}^{(r)})^2}, \tag{3.16}$$

where $\bar{d}^{(r)}$ are the target weights that force the WENO scheme to asymptote to a target central difference scheme in smooth regions of the flow. The smoothness indicators, $\bar{\beta}^{(r)}$, are given by

$$\bar{\beta}_i^L = (f_i - f_{i-1})^2, \quad \bar{\beta}_i^C = (f_{i+1} - f_i)^2, \quad \bar{\beta}_i^R = (f_{i+2} - f_{i+1})^2. \tag{3.17}$$

The parameter ϵ is set to 10^{-6} to prevent a zero denominator.[88] This WENO scheme does not follow SBP convention; thus, an energy estimate is not readily obtainable.[43]

The ESWENO scheme involves a modification of the WENO weight functions such that the derivative operator satisfies SBP, making an energy estimate possible. Furthermore, an artifical dissipation term is added to the derivative operator to maintain stability. We consider the finite-domain ESWENO 3-4-3 scheme, which uses a fourth-order approximation in the domain interior and an inward-biased, third-order approximation near boundaries. This scheme is globally fourth-order.[46,89,90]

The finite-domain ESWENO 3-4-3 scheme is formed by constructing a derivative operator that permits the WENO stencil-biasing framework of Eq. (3.36) and satisfies the SBP requirements of Eqs. (3.4)-(3.6). The grid-points are uniformly distributed with spacing $\delta x = x_i - x_{i-1}$, while the flux-points are nonuniformly distributed with spacing $\bar{\delta}x = \bar{x}_i - \bar{x}_{i-1}$. The grid suggested in Ref. [46] is used:

$$\bar{x} = \left[A, \left(A + \frac{43\delta x}{144} \right), \left(A + \frac{61\delta x}{36} \right), \left(A + \frac{349\delta x}{144} \right), \left(A + \frac{7\delta x}{2} \right), \dots, \right.$$
$$\left. \left(B - \frac{7\delta x}{2} \right), \left(B - \frac{349\delta x}{144} \right), \left(B - \frac{61\delta x}{36} \right), \left(B - \frac{43\delta x}{144} \right), B \right]. \tag{3.18}$$

The ESWENO differentiation operator has the form,

$$\boldsymbol{D} = \boldsymbol{P}^{-1}\boldsymbol{\Delta}\sum_r \bar{w}^{(r)}\boldsymbol{\mathcal{I}}^{(r)}, \tag{3.19}$$

where $r = L, C, R$ are the three candidate stencils. Differentiation of the flux, $\boldsymbol{f}$, yields

$$\boldsymbol{D}\boldsymbol{f} = \boldsymbol{P}^{-1}\boldsymbol{\Delta}\sum_r \bar{w}^{(r)}\bar{\boldsymbol{f}}^{(r)} = \boldsymbol{P}^{-1}\boldsymbol{\Delta}\sum_r \bar{w}^{(r)}\boldsymbol{\mathcal{I}}^{(r)}\boldsymbol{f}. \tag{3.20}$$

40

The ESWENO weight functions are defined by

$$\bar{w}^{(r)} = \frac{\bar{\alpha}^{(r)}}{\sum_r \bar{\alpha}^{(r)}}, \quad \bar{\alpha}^{(r)} = d^{(r)} \left(1 + \frac{\bar{\tau}}{(\epsilon + \bar{\beta}^{(r)})^2} \right), \quad (3.21)$$

with stencil biasing parameters,

$$\bar{\tau}_i = (-f_{i-1} + 3f_i - 3f_{i+1} + f_{i+2})^2, \quad 2 \le i \le N - 2, \quad (3.22)$$

$$\bar{\tau}_i = (-f_i + 3f_{i+1} - 3f_{i+2} + f_{i+3})^2, \quad i = 1, \quad (3.23)$$

$$\bar{\tau}_i = (-f_i + 3f_{i-1} - 3f_{i-2} + f_{i-3})^2, \quad i = N - 1. \quad (3.24)$$

The smoothness indicators, $\bar{\beta}^{(r)}$, remain the same as in WENO. However, extra stencils, S^{LL} and S^{RR}, and smoothness indicators,

$$\bar{\beta}_i^{LL} = (f_{i-1} - f_{i-2})^2, \quad \bar{\beta}_i^{RR} = (f_{i+3} - f_{i+2})^2, \quad (3.25)$$

are needed to facilitate third-order stencil-biasing mechanics near the boundaries. A limiting operation is used to ensure that the downwind (DW) stencil weight does not overtake the central or upwind weights:

$$\bar{\beta}_i^{\mathrm{DW}} = \left(\frac{1}{3} \sum_r \left[\bar{\beta}_i^{(r)} \right]^4 \right)^{\frac{1}{4}}. \quad (3.26)$$

A block-norm, $\boldsymbol{P}$, of the form,

$$\boldsymbol{P} = \delta x \begin{pmatrix} \boldsymbol{P}_0 & 0 & 0 \\ 0 & \boldsymbol{I} & 0 \\ 0 & 0 & \boldsymbol{P}_0^{PT} \end{pmatrix}, \quad \boldsymbol{P}_0 = \begin{pmatrix} p_{11} & p_{12} & p_{13} & p_{14} \\ p_{12} & p_{22} & p_{23} & p_{24} \\ p_{13} & p_{23} & p_{33} & p_{34} \\ p_{14} & p_{24} & p_{34} & p_{44} \end{pmatrix}, \quad (3.27)$$

is used and the derivative operator takes the form,

$$\boldsymbol{Q} = \begin{pmatrix} Q_0 & Q_d & 0 \\ -Q_d^T & Q_l & Q_d \\ 0 & -Q_d^T & -(Q_0)^{PT} \end{pmatrix}, \quad \boldsymbol{Q}_0 = \begin{pmatrix} -\frac{1}{2} & q_{12} & q_{13} & q_{14} \\ -q_{12} & 0 & q_{23} & q_{24} \\ -q_{13} & -q_{23} & 0 & q_{34} \\ -q_{14} & -q_{24} & -q_{34} & 0 \end{pmatrix},$$

$$\boldsymbol{Q}_d = \begin{pmatrix} 0 & \cdots & & \\ 0 & \cdots & & \\ -\frac{1}{12} & 0 & \cdots & \\ \frac{8}{12} & -\frac{1}{12} & 0 & \cdots \end{pmatrix}, \tag{3.28}$$

where PT denotes the per-symmetric transpose, $P_{ij} = P_{[N-(i-1)][N-(j-1)]}$. The matrix $\boldsymbol{P}$ and target operator $\boldsymbol{D}$ are given in Appendix B.

A key distinction of the ESWENO scheme is its energy-stabilization term. The baseline WENO scheme,

$$\boldsymbol{D}_{weno} = \boldsymbol{P}^{-1}\left(\boldsymbol{Q} + \boldsymbol{R}_{weno}\right), \tag{3.29}$$

does not guarantee stability; the elements of R_{weno} may take negative values such that R_{weno} is not SPS. Stability is achieved by adding a dissipative operator, $\boldsymbol{R}_{es}$, to ensure that the total dissipation operator, $\boldsymbol{R} = \boldsymbol{R}_{weno} + \boldsymbol{R}_{es}$, is SPS. The ESWENO scheme has the form,

$$\boldsymbol{D} = \boldsymbol{P}^{-1}\left(\boldsymbol{Q} + \boldsymbol{R}_{weno} + \boldsymbol{R}_{es}\right). \tag{3.30}$$

The stabilization operator, $\boldsymbol{R}_{es}$, is determined by enforcing the condition that the total dissipation operator, $\boldsymbol{R}$, is SPS and the entire scheme remains design-order. We expand $\boldsymbol{R}_{weno}$ as[43]

$$\boldsymbol{P}^{-1}\boldsymbol{R}_{weno} = \boldsymbol{\Lambda}_0 + \boldsymbol{\Delta}\boldsymbol{\Lambda}_1\left[\boldsymbol{\Delta}\right]^T + \boldsymbol{\Delta}\left[\boldsymbol{\Delta}\right]^T \boldsymbol{\Lambda}_2\boldsymbol{\Delta}\left[\boldsymbol{\Delta}\right]^T + \boldsymbol{\Delta}\left[\boldsymbol{\Delta}\right]^T \boldsymbol{\Delta}\boldsymbol{\Lambda}_3\left[\boldsymbol{\Delta}\right]^T \boldsymbol{\Delta}\left[\boldsymbol{\Delta}\right]^T, \tag{3.31}$$

and assuming a similar form for $\boldsymbol{R}_{es}$:

$$\boldsymbol{P}^{-1}\boldsymbol{R}_{es} = \hat{\boldsymbol{\Lambda}}_0 + \boldsymbol{\Delta}\hat{\boldsymbol{\Lambda}}_1\left[\boldsymbol{\Delta}\right]^T + \boldsymbol{\Delta}\left[\boldsymbol{\Delta}\right]^T \hat{\boldsymbol{\Lambda}}_2\boldsymbol{\Delta}\left[\boldsymbol{\Delta}\right]^T + \boldsymbol{\Delta}\left[\boldsymbol{\Delta}\right]^T \boldsymbol{\Delta}\hat{\boldsymbol{\Lambda}}_3\left[\boldsymbol{\Delta}\right]^T \boldsymbol{\Delta}\left[\boldsymbol{\Delta}\right]^T. \tag{3.32}$$

We guarantee that $\boldsymbol{R}$ is SPS by smoothly enforcing positivity:

$$[\lambda_j]_i + [\hat{\lambda}_j]_i \geq 0, \quad \forall\, i, j. \tag{3.33}$$

We achieve this by constructing the components of $\hat{\boldsymbol{\Lambda}}_j$ as

$$[\hat{\lambda}_j]_i = \frac{1}{2}\left(\sqrt{[\lambda_j]_i^2 + \delta_i^2} - [\lambda_j]_i\right). \tag{3.34}$$

Design-order accuracy is preserved if the constraints $\delta_1 \leq O\left(\delta x^3\right)$ and $\delta_2 \leq O\left(\delta x^2\right)$ are satisfied. The matrices $\mathbf{\Lambda}_i$ are specified in Appendix B. Defining the dissipative energy-stabilization flux,

$$\bar{\boldsymbol{\psi}} = \left[\hat{\mathbf{\Lambda}}_1 \left[\mathbf{\Delta}\right]^T + \left[\mathbf{\Delta}\right]^T \hat{\mathbf{\Lambda}}_2 \mathbf{\Delta} \left[\mathbf{\Delta}\right]^T + \left[\mathbf{\Delta}\right]^T \mathbf{\Delta} \hat{\mathbf{\Lambda}}_3 \left[\mathbf{\Delta}\right]^T \mathbf{\Delta} \left[\mathbf{\Delta}\right]^T \right] \boldsymbol{f}, \qquad (3.35)$$

allows the energy-stabilization operator to be combined with the WENO operator, yielding the combined flux form,

$$\boldsymbol{f}_x = \boldsymbol{D}\boldsymbol{f} = \boldsymbol{P}^{-1}\mathbf{\Delta}\left(\bar{\boldsymbol{f}} + \bar{\boldsymbol{\psi}}\right). \qquad (3.36)$$

3.1.2 Simultaneous Approximation Term Penalty Procedure

The simultaneous approximation term (SAT) penalty procedure was first introduced by Carpenter *et al.*[91] for boundary closures. It was later extended to interface closures.[47] Since that work, it has been successfully used for boundary and interface closures in a myriad of high-order numerical schemes.[92–95] Here, both boundary and interface conditions are imposed using SAT. Henceforth, the term *interface* shall generally refer to both subdomain interfaces *and* domain boundaries, as their SAT treatment is identical. A boundary is simply treated as a neighboring subdomain whose data on $\partial\Omega$ (domain boundary) is known exactly.

The SAT methodology is a *weak* penalty procedure, in that instead of strictly enforcing interface data by requiring the values of the solution at the interface x_i to be identical in the two neighboring subdomains, the values of the solution at these interfaces are penalized to pull the respective interface values together. The advantage of such a weak imposition of the interface condition is that it allows the global finite difference scheme to maintain SBP and, consequently, stability. Design-order accuracy of the scheme is also assured by choice of the free parameters.

We begin by requiring that neighboring subdomains have collocated points on their shared interfacial surface. The discrete solutions to Eq. (3.1) on the left and

right subdomains are denoted by $\boldsymbol{u}_L$ and $\boldsymbol{u}_R$, respectively. The semi-discrete form of Eq. (3.1) using the SAT interface penalty is

$$\frac{\partial \boldsymbol{u}_L}{\partial t} + a\boldsymbol{P}_L^{-1}\boldsymbol{Q}_L\boldsymbol{u}_L = \sigma_1 \boldsymbol{P}_L^{-1}\boldsymbol{e}_L \left[\boldsymbol{u}_L|_{x=x_i} - \boldsymbol{u}_R|_{x=x_i}\right], \tag{3.37}$$

$$\frac{\partial \boldsymbol{u}_R}{\partial t} + a\boldsymbol{P}_R^{-1}\boldsymbol{Q}_R\boldsymbol{u}_R = \sigma_3 \boldsymbol{P}_R^{-1}\boldsymbol{e}_R \left[\boldsymbol{u}_R|_{x=x_i} - \boldsymbol{u}_L|_{x=x_i}\right], \tag{3.38}$$

where x_i is the spatial location of the interface, $e_L = [0, ..., 0, 1]^T$, and $e_R = [1, 0, ..., 0]^T$. As described in Ref. [47], Eqs. (3.37)–(3.38) are stable and preserve design-order accuracy if

$$\sigma_1 \quad \leq \quad \frac{a}{2}, \tag{3.39}$$

$$\sigma_3 \quad = \quad \sigma_1 - a. \tag{3.40}$$

The SAT interface penalty provides subdomain connectivity for the multi-block formulation as described in the next section.

3.1.3 Univariate One-Dimensional Multi-Block Formulation

The formulation is first presented in the context of the continuous, one-dimensional linear scalar wave equation on the global domain $x \in [A, B]$:

$$
\begin{aligned}
&\frac{\partial v}{\partial t} + \frac{\partial F}{\partial x} = 0, \quad F = av, \quad x \in \Omega, \quad \Omega = [A, B], \\
&v(x, 0) = v_0(x), \\
&v(A, t) = g_L(t), \text{ if } a > 0, \\
&v(B, t) = g_R(t), \text{ if } a < 0,
\end{aligned}
\tag{3.41}
$$

where a is the constant wave speed and g_L and g_R denote boundary conditions on the left and right sides of the global domain, respectively. The domain, Ω, is partitioned into K subdomains. The subdomain $k \in \{1, 2, \ldots, K\}$ is discretized with N_k grid-points on the local domain $\Omega_k = [x_L, x_R] \subset \Omega$ and $x \in \Omega_k$: $\boldsymbol{x}_k = [x_1 = x_L, x_2, \ldots, x_{N_k} = x_R]$. We seek the discrete solution on each subdomain: $\boldsymbol{u}_k = [u_1, u_2, \ldots, u_{N_k}]$. The first and last points in each subdomain lie on the subdomain boundary, such that there are two collocated points at each subdomain interface. Each subdomain utilizes an SBP-satisfying differentiation scheme, $\boldsymbol{D} = \boldsymbol{P}^{-1}\boldsymbol{Q}$,

which may be different on each subdomain. This leads to the following semi-discrete form:

$$\boldsymbol{u}_t + a\boldsymbol{P}^{-1}\boldsymbol{Q}\boldsymbol{u} = (\sigma - \frac{1}{2})a\boldsymbol{P}^{-1}\left[\mathtt{I}_{a>0}\left(u_{L,k} - u_{L,n_L}\right)\boldsymbol{e}_1 - (1 - \mathtt{I}_{a>0})\left(u_{R,k} - u_{R,n_R}\right)\boldsymbol{e}_{N_k}\right],$$
$$(3.42)$$

where the RHS represents the SAT interface penalty to account for interface conditions. In Eq. (3.42), the left and right interface values on subdomain k are denoted by $u_{L,k}$ and $u_{R,k}$, respectively. Corresponding interface values on its neighbors with partition numbers n_L and n_R are denoted by u_{L,n_L} and u_{R,n_R}, respectively. The vectors,

$$\begin{aligned} \boldsymbol{e}_1 &= [1, 0, \ldots, 0]^T, \\ \boldsymbol{e}_{N_k} &= [0, \ldots, 0, 1]^T, \end{aligned} \qquad (3.43)$$

have length N_k and are used to restrict the penalty term to only the collocated interface points, although a non-diagonal ESWENO 3-4-3 $\boldsymbol{P}$-matrix will effectively smear the effect of the boundary penalty across multiple points near the interface. The indicator function,

$$\mathtt{I}_{a>0} = \begin{cases} 0 & : a \leq 0 \\ 1 & : a > 0 \end{cases}, \qquad (3.44)$$

is used to require that interface information always travels downwind. The SAT parameter, σ, controls the tightness of coupling between subdomains.* The discretization of Eq. (3.42) has been previously shown to be stable and accurate for $\sigma \leq 0$.[47,91] Reducing the value of σ indicates additional artificial dissipation at the interface. Unless otherwise noted, a value of $\sigma = -\frac{1}{2}$ is used for all calculations. Extra dissipation is added in some cases to maintain stability near subdomain interfaces because WENO stencil-biasing is not possible. In general, the second term on the LHS of Eq. (3.42) can be any SBP-satisfying differentiation scheme and need not be the same for each subdomain. Here, the globally fourth-order accurate ESWENO 3-4-3 scheme is used for all subdomains.

Equation (3.42) is time-stable and accurate to the design-order of $\boldsymbol{Q}$. Stability

---

*The notation of the constant, σ, is presented in a slightly different notation than that of Eqs. (3.37)–(3.38); however, the two forms are equivalent.

and accuracy of the multi-block scheme follows trivially by combining the proofs in Refs. [46, 47]. These hold due to the combination of stable and accurate derivative operators and boundary closures.

3.1.4 Hyperbolic Systems

The multi-block formulation is developed in the context of a single linear hyperbolic equation. Systems of hyperbolic equations are accommodated via a characteristic decomposition that forms a set of uncoupled, frozen, linear hyperbolic equations that each fit the form of Eq. (3.41). The linear differentiation and penalty scheme is applied on each of the characteristic equations. The resultant characteristic quantities are transformed back into the physical space prior to time integration. This is described further below.

First, we consider the general one-dimensional hyperbolic system of M differential equations,

$$\frac{\partial \boldsymbol{U}}{\partial t} + \frac{\partial \boldsymbol{F}}{\partial x} = 0, \quad \boldsymbol{F} = \boldsymbol{F}(\boldsymbol{U}), \tag{3.45}$$

where $\boldsymbol{U}\left(\boldsymbol{x}, t\right) = \left[U_1\left(\boldsymbol{x}, t\right), U_2\left(\boldsymbol{x}, t\right), \dots, U_M\left(\boldsymbol{x}, t\right)\right]$ is a vector of M conserved variables and $\boldsymbol{F}\left(\boldsymbol{x}, t\right) = \left[F_1\left(\boldsymbol{x}, t\right), F_2\left(\boldsymbol{x}, t\right), \dots, F_M\left(\boldsymbol{x}, t\right)\right]$ is the flux vector. Applying the chain rule to the second term on the LHS of Eq. (3.45) yields

$$\frac{\partial \boldsymbol{U}}{\partial t} + \boldsymbol{A}\frac{\partial \boldsymbol{U}}{\partial x} = 0, \tag{3.46}$$

where the tensor $\boldsymbol{A} = \partial \boldsymbol{F}/\partial \boldsymbol{U}$ is the Jacobian matrix. We seek a characteristic eigen-decomposition of the form,

$$\boldsymbol{A} = \boldsymbol{S}\boldsymbol{\Lambda}\boldsymbol{S}^{-1}, \tag{3.47}$$

with eigenvalue matrix $\boldsymbol{\Lambda} = \text{Diag}\left[\lambda_1, \lambda_2, \dots, \lambda_M\right]$ and left eigenvector matrix $\boldsymbol{S}$. Note that the eigen-decomposition in Eq. (3.47) is not guaranteed, in general, for all hyperbolic systems. We freeze $\boldsymbol{S}$ and $\boldsymbol{\Lambda}$ at a single point in time and space, substitute Eq. (3.47) into Eq. (3.46), and premultiply by $\boldsymbol{S}^{-1}$ to find the characteristic form:

$$\frac{\partial \boldsymbol{U}_c}{\partial t} + \boldsymbol{\Lambda}\frac{\partial \boldsymbol{U}_c}{\partial x} = 0, \tag{3.48}$$

where $\boldsymbol{U}_c = \boldsymbol{S}^{-1}\boldsymbol{U}$ and $\boldsymbol{F}_c = \boldsymbol{\Lambda}\boldsymbol{U}_c$ are the characteristic variables formed by transforming the physical variables $\boldsymbol{U}$ into characteristic space via $\boldsymbol{S}^{-1}$. Equation (3.48) is a set of uncoupled hyperbolic equations in characteristic space. The SAT penalty is applied in the linearized characteristic space:[47]

$$
\frac{\partial \boldsymbol{U}_c}{\partial t} + \boldsymbol{\Lambda}\frac{\partial \boldsymbol{U}_c}{\partial x} = (\sigma - \frac{1}{2})\boldsymbol{P}^{-1}\boldsymbol{\Lambda}\left[\mathtt{I}_{\boldsymbol{\Lambda}>0}\left([\boldsymbol{U}_c]_{L,k} - [\boldsymbol{U}_c]_{L,n_L}\right)\boldsymbol{e}_1 \right.
$$
$$
\left. - (1 - \mathtt{I}_{\boldsymbol{\Lambda}>0})\left([\boldsymbol{U}_c]_{R,k} - [\boldsymbol{U}_c]_{R,n_R}\right)\boldsymbol{e}_{N_k}\right]. \tag{3.49}
$$

Characteristic implementation for the new ESWENO-SAT scheme is as follows. The multi-block discretization, Eq. (3.42) is applied in characteristic space and rotated back into the physical space before time-integration. The semidiscrete form is

$$
\frac{\partial \boldsymbol{U}}{\partial t} + \boldsymbol{DF} = \boldsymbol{P}^{-1}\boldsymbol{S}(\sigma - \frac{1}{2})\boldsymbol{\Lambda}\left[\mathtt{I}_{\boldsymbol{\Lambda}>0}\left([\boldsymbol{U}_c]_{L,k} - [\boldsymbol{U}_c]_{L,n_L}\right)\boldsymbol{e}_1 \right.
$$
$$
\left. - (1 - \mathtt{I}_{\boldsymbol{\Lambda}>0})\left([\boldsymbol{U}_c]_{R,k} - [\boldsymbol{U}_c]_{R,n_R}\right)\boldsymbol{e}_{N_k}\right], \tag{3.50}
$$

where $\boldsymbol{D}$ represents the ESWENO differentiation operator. We expand $\boldsymbol{D}$ by applying the flux-differencing form of Eq. (3.36):

$$
\boldsymbol{DF} = \boldsymbol{P}^{-1}\boldsymbol{\Delta}\left(\bar{\boldsymbol{F}} + \bar{\boldsymbol{\psi}}\right). \tag{3.51}
$$

We expand $\bar{\boldsymbol{F}}$ using the interpolation matrices as in Eq. (3.20):

$$
\boldsymbol{DF} = \boldsymbol{P}^{-1}\boldsymbol{\Delta}\left(\sum_r \bar{w}^{(r)}\boldsymbol{\mathcal{I}}^{(r)}\boldsymbol{F} + \bar{\boldsymbol{\psi}}\right). \tag{3.52}
$$

We expand $\boldsymbol{F}$ using the characteristic decomposition in Eq. (3.47):

$$
\begin{aligned}
\boldsymbol{DF} &= \boldsymbol{P}^{-1}\boldsymbol{\Delta}\left(\sum_r \bar{w}^{(r)}\boldsymbol{\mathcal{I}}^{(r)}\boldsymbol{A}\boldsymbol{U} + \bar{\boldsymbol{\psi}}\right)\\
&= \boldsymbol{P}^{-1}\boldsymbol{\Delta}\left(\sum_r \bar{w}^{(r)}\boldsymbol{\mathcal{I}}^{(r)}\boldsymbol{S}\boldsymbol{\Lambda}\boldsymbol{S}^{-1}\boldsymbol{U} + \bar{\boldsymbol{\psi}}\right)\\
&= \boldsymbol{P}^{-1}\boldsymbol{\Delta}\boldsymbol{S}\left(\sum_r \bar{w}^{(r)}\boldsymbol{\mathcal{I}}^{(r)}\boldsymbol{\Lambda}\boldsymbol{U}_c + \boldsymbol{S}^{-1}\bar{\boldsymbol{\psi}}\right).
\end{aligned} \tag{3.53}
$$

To facilitate upwinding, we introduce the Lax-Friedrichs flux splitting,

$$
\boldsymbol{F}_c^{\pm} = \frac{1}{2}\left(\boldsymbol{\Lambda}\boldsymbol{U}_c \pm \boldsymbol{\Lambda}_{max}\boldsymbol{U}_c\right), \tag{3.54}
$$

where $\boldsymbol{\Lambda}_{max}$ is the length M vector of maximum eigenvalues on subdomain k. The final form of the derivative operator is

$$\boldsymbol{DF} = \boldsymbol{P}^{-1}\boldsymbol{\Delta S}\left(\sum_r \bar{w}^{(r)}\boldsymbol{\mathcal{I}}^{(r)}\boldsymbol{F}_c^+ + \sum_r \bar{w}^{(r)}\boldsymbol{\mathcal{I}}^{(r)}\boldsymbol{F}_c^- + \boldsymbol{S}^{-1}\bar{\boldsymbol{\psi}}\right). \qquad (3.55)$$

The final semidiscrete form is

$$\frac{\partial \boldsymbol{U}}{\partial t} + \boldsymbol{P}^{-1}\boldsymbol{\Delta S}\left(\sum_r \bar{w}^{(r)}\boldsymbol{\mathcal{I}}^{(r)}\boldsymbol{F}_c^+ + \sum_r \bar{w}^{(r)}\boldsymbol{\mathcal{I}}^{(r)}\boldsymbol{F}_c^- + \boldsymbol{S}^{-1}\bar{\boldsymbol{\psi}}\right) =$$
$$\boldsymbol{P}^{-1}\boldsymbol{S}(\sigma - \frac{1}{2})\boldsymbol{\Lambda}\left[\mathtt{I}_{\boldsymbol{\Lambda}>0}\left([\boldsymbol{U}_c]_{L,k} - [\boldsymbol{U}_c]_{L,n_L}\right)\boldsymbol{e}_1 - (1 - \mathtt{I}_{\boldsymbol{\Lambda}>0})\left([\boldsymbol{U}_c]_{R,k} - [\boldsymbol{U}_c]_{R,n_R}\right)\boldsymbol{e}_{N_k}\right]. \tag{3.56}$$

This yields an effective multi-block ESWENO numerical approximation of the derivative:

$$\boldsymbol{D}_{eff}\boldsymbol{F} = \boldsymbol{P}^{-1}\boldsymbol{\Delta S}\left(\sum_r \bar{w}^{(r)}\boldsymbol{\mathcal{I}}^{(r)}\boldsymbol{F}_c^+ + \sum_r \bar{w}^{(r)}\boldsymbol{\mathcal{I}}^{(r)}\boldsymbol{F}_c^- + \boldsymbol{S}^{-1}\bar{\boldsymbol{\psi}}\right)$$
$$- \boldsymbol{P}^{-1}\boldsymbol{S}(\sigma - \frac{1}{2})\boldsymbol{\Lambda}\left[\mathtt{I}_{\boldsymbol{\Lambda}>0}\left([\boldsymbol{U}_c]_{L,k} - [\boldsymbol{U}_c]_{L,n_L}\right)\boldsymbol{e}_1 - (1 - \mathtt{I}_{\boldsymbol{\Lambda}>0})\left([\boldsymbol{U}_c]_{R,k} - [\boldsymbol{U}_c]_{R,n_R}\right)\boldsymbol{e}_{N_k}\right]. \tag{3.57}$$

The new scheme is also applicable for numerical solution of multi-dimensional systems of equations. For illustration, we consider the two-dimensional system of m coupled hyperbolic equations,

$$\frac{\partial \boldsymbol{U}}{\partial t} + \frac{\partial \boldsymbol{F}}{\partial x} + \frac{\partial \boldsymbol{G}}{\partial y} = 0, \quad \boldsymbol{F} = \boldsymbol{F}(\boldsymbol{U}), \quad \boldsymbol{G} = \boldsymbol{G}(\boldsymbol{U}), \qquad (3.58)$$

where $\boldsymbol{U} = [U_1, U_2, \ldots, U_M]$. We use chain rule to expand the last two terms on the LHS of Eq. (3.58),

$$\frac{\partial \boldsymbol{U}}{\partial t} + \boldsymbol{A}_x\frac{\partial \boldsymbol{U}}{\partial x} + \boldsymbol{A}_y\frac{\partial \boldsymbol{U}}{\partial y} = 0, \qquad (3.59)$$

where the Jacobians $\boldsymbol{A}_x = \frac{\partial \boldsymbol{F}}{\partial \boldsymbol{U}}$ and $\boldsymbol{A}_y = \frac{\partial \boldsymbol{G}}{\partial \boldsymbol{U}}$ are assumed to have the eigen-decomposition,

$$\boldsymbol{A}_x = \boldsymbol{S}_x\boldsymbol{\Lambda}_x\boldsymbol{S}_x^{-1}, \qquad (3.60\text{a})$$

$$\boldsymbol{A}_y = \boldsymbol{S}_y\boldsymbol{\Lambda}_y\boldsymbol{S}_y^{-1}. \qquad (3.60\text{b})$$

Substituting Eq. (3.60) into Eq. (3.59):

$$\frac{\partial \boldsymbol{U}}{\partial t} + \boldsymbol{S}_x \frac{\partial \boldsymbol{F}_c}{\partial x} + \boldsymbol{S}_y \frac{\partial \boldsymbol{G}_c}{\partial y} = 0. \tag{3.61}$$

We solve Eq. (3.61) by independently applying Eq. (3.57) on $\frac{\partial \boldsymbol{F}}{\partial x}$ and $\frac{\partial \boldsymbol{G}}{\partial y}$, then integrating over time. For example, the characteristic decomposition of the two-dimensional Euler equations,

$$\frac{\partial \boldsymbol{U}}{\partial t} + \frac{\partial \boldsymbol{F}}{\partial x} + \frac{\partial \boldsymbol{G}}{\partial y} = 0, \tag{3.62}$$

$$\boldsymbol{U} = \begin{pmatrix} \rho \\ \rho u \\ \rho v \\ \rho E \end{pmatrix}, \quad \boldsymbol{F} = \begin{pmatrix} \rho u \\ \rho u^2 + p \\ \rho uv \\ (\rho E + p)u \end{pmatrix}, \quad \boldsymbol{G} = \begin{pmatrix} \rho v \\ \rho uv \\ \rho v^2 + p \\ (\rho E + p)v \end{pmatrix},$$

is accomplished via the characteristic decomposition of Pulliam and Chaussee,[96]

$$\boldsymbol{S}_h = \begin{pmatrix} 1 & 0 & \alpha & \alpha \\ \bar{u} & \bar{\rho}\left(1 - \mathtt{I}_{h=\text{`x'}}\right) & \alpha(\bar{u} + \mathtt{I}_{h=\text{`x'}}c) & \alpha(\bar{u} - \mathtt{I}_{h=\text{`x'}}c) \\ \bar{v} & -\bar{\rho}\mathtt{I}_{h=\text{`x'}} & \alpha\left[\bar{v} + (1 - \mathtt{I}_{h=\text{`x'}})\,c\right] & \alpha\left[\bar{v} - (1 - \mathtt{I}_{h=\text{`x'}})\,c\right] \\ \frac{\phi^2}{\gamma-1} & \bar{\rho}\left[(1 - \mathtt{I}_{h=\text{`x'}})\,\bar{u} - \mathtt{I}_{h=\text{`x'}}\bar{v}\right] & \alpha(\frac{\phi^2+c^2}{\gamma-1} + c\theta) & \alpha(\frac{\phi^2+c^2}{\gamma-1} - c\theta) \end{pmatrix}, \tag{3.63}$$

$$\boldsymbol{S}_h^{-1} = \begin{pmatrix} 1 - \frac{\phi^2}{c^2} & (\gamma-1)\frac{\bar{u}}{c^2} & (\gamma-1)\frac{\bar{v}}{c^2} & -\frac{\gamma-1}{c^2} \\ \frac{\mathtt{I}_{h=\text{`x'}}\bar{v} - (1 - \mathtt{I}_{h=\text{`x'}})\bar{u}}{\bar{\rho}} & \frac{1 - \mathtt{I}_{h=\text{`x'}}}{\bar{\rho}} & -\frac{\mathtt{I}_{h=\text{`x'}}}{\bar{\rho}} & 0 \\ \beta(\phi^2 - c\theta) & \beta\left[\mathtt{I}_{h=\text{`x'}}c - (\gamma-1)\bar{u}\right] & \beta\left[(1 - \mathtt{I}_{h=\text{`x'}})\,c - (\gamma-1)\bar{v}\right] & \beta(\gamma-1) \\ \beta(\phi^2 + c\theta) & -\beta\left[\mathtt{I}_{h=\text{`x'}}c + (\gamma-1)\bar{u}\right] & -\beta\left[(1 - \mathtt{I}_{h=\text{`x'}})\,c + (\gamma-1)\bar{v}\right] & \beta(\gamma-1) \end{pmatrix}, \tag{3.64}$$

$$\begin{aligned} \alpha &= \frac{\rho}{\sqrt{2}c}, \\ \beta &= \frac{1}{\sqrt{2}\rho c}, \\ \theta &= \mathtt{I}_{h=\text{`x'}}u + (1 - \mathtt{I}_{h=\text{`x'}})\,v, \\ \phi^2 &= \frac{1}{2}\left(\gamma - 1\right)u^2 + v^2, \end{aligned}$$

where the matrices $\boldsymbol{S}_x$ and $\boldsymbol{S}_y$ are presented in the representative form $\boldsymbol{S}_h$, $h \in \{\text{`x'}, \text{`y'}\}$. The operator $\mathtt{I}_{h=\text{`x'}}$ is an indicator function for $h = \text{`x'}$.

3.2 DEMONSTRATION

The ESWENO-SAT implementation is initialized by defining the problem geometry and partitioning the domain into a set of independent subdomains. If curvilinear meshes are used, the shape of the subdomains is flexible and the domain decomposition may be entirely unstructured, with each block having an arbitrary shape.[†] Such a flexibility allows blocks surrounding complex geometry to exactly match the body only locally, instead of fitting the entire body with one mesh. The only requirement is that for each subdomain-to-subdomain interface, the sets of points lying on the interface owned by the left and right subdomains must be collocated.[‡] No restriction is placed on similarity of grid topology or grid-spacing.

In this implementation, each subdomain is sent to a single processor on a distributed-memory computing architecture. The multi-block ESWENO scheme, Eq. (3.57), is carried out separately on each subdomain, in each dimension, with message-passing of collocated interface points between neighboring subdomains for calculation of the SAT penalty. Time integration is via an explicit fourth-order Runge-Kutta scheme.[99] A detailed pseudocode description the implementation is presented in Appendix B.

Simulation results are presented to show the stability and accuracy of the multi-block scheme. Design-order accuracy on smooth problems is shown and the ability of the scheme to accurately capture strong shocks without significant oscillation or diffusion is exemplified. A highlight of the results is the lack of interference of subdomain interfaces on the physics. Both delicate physical phenomena (such as a weak vortex) and strong shocks pass through interfaces without noticeable diffusion or dispersion, even in the presence of large jumps in grid-spacing across the interface.

Additionally, some simulations using strongly-imposed interface conditions are performed for comparison with results using the SAT interface conditions described in the previous section. Strong interface condition imposition involves overwriting data at the interface with results calculated on the upwind subdomain. The interface

---

[†]In the work presented in this chapter, only Cartesian meshes are used; extension to curvilinear grids is reserved for a future work.

[‡]It seems feasible that this requirement could be relaxed by repurposing ideas from adaptive mesh refinement (AMR).[97,98] Development for non-collocated interface points is reserved for a future work.

upwinding is performed before each Runge-Kutta substep and again on the global variables after each global time integration. Unless otherwise noted, simulations default to weak SAT interface conditions.

Results are presented for one- and two-dimensional test problems for both linear and nonlinear hyperbolic systems. To demonstrate convergence of the scheme to design-order accuracy, the L_2 error,

$$\|E\|_{L_2} = \sqrt{\sum_{m=1}^{M} \int_{\Omega} (u_m - v_m)^2 \, dxdy}, \qquad (3.65)$$

is integrated numerically using the midpoint rectangle rule.

3.2.1 One-Dimensional Linear Scalar Wave Equation

The one-dimensional linear scalar hyperbolic wave equation,

$$\frac{\partial \rho}{\partial t} + \frac{\partial \rho}{\partial x} = 0, \qquad (3.66)$$

is solved for the conserved scalar $\rho(x,t)$. Numerical results are presented comparing strong versus weak boundary and interface conditions. Equation (3.66) is solved for both smooth and discontinuous initial conditions.

Sine-Wave Advection: Equation (3.66) is solved numerically with the initial condition,

$$\rho(x,0) = \sin(x), \quad x \in [-\pi, \pi], \qquad (3.67)$$

after ten flow-through times. Calculations are performed on both a single subdomain and 4 equally-spaced subdomains. The L_2 error and the convergence rates are shown in Table 3. Both single- and multi-domain results converge to design-order. Moreover, the difference in L_2 error between the two configurations is negligible. Calculations are also performed on 4 unequally-spaced subdomains using the initial condition,

$$\rho(x,0) = \sin(2\pi f x), \quad x \in [0, 1], \qquad (3.68)$$

with frequency $f = 3.0$ with periodic boundary conditions for one flow-through time. Results for both strong and weak interface conditions on a mesh with 101 points per

Table 3: L_2 error and convergence rates for the one-dimensional sine wave advection problem on single and multiple subdomains.

Number	Single domain		Four subdomains	
of points	$\log(L_2)$	Rate	$\log(L_2)$	Rate
21	-0.2998		0.1996	
49	-1.7806	3.89	-1.7819	5.21
101	-3.0587	4.01	-3.0589	4.01
201	-4.2638	4.00	-4.2640	4.00
401	-5.4682	4.00	-5.4683	4.00
801	-6.6723	4.00	-6.6724	4.00
1601	-7.8700	3.98	-7.8628	3.95

subdomain are displayed in Fig. 25. The maximum grid compression ratio between neighboring subdomains is 4. No noticeable oscillations appear for either interface condition scheme.

Square-Wave Advection: Equation (3.66) is solved with the initial condition,

$$\rho(x,0) = \begin{cases} 1 & : & x \in (0.3, 0.6) \\ 0 & : & x \notin (0.3, 0.6) \end{cases}, \quad x \in [0, 1], \tag{3.69}$$

and periodic boundary conditions, for one flow-through time. Calculations are performed on 4 unequally-spaced subdomains using strong and weak boundary and interface conditions. Figure 26 shows sample results on a mesh with 26 grid-points per subdomain and 104 total points. The maximum grid-compression factor between neighboring subdomains is 4. Strong imposition of the interface conditions results in significant oscillations, while weak conditions eliminate these oscillations.

3.2.2 Two-Dimensional Linear Scalar Wave Equation

The two-dimensional linear scalar hyperbolic wave equation,

$$\frac{\partial \rho}{\partial t} + a\frac{\partial \rho}{\partial x} + b\frac{\partial \rho}{\partial y} = 0, \tag{3.70}$$

is solved for the conserved scalar $\rho(x, y, t)$. The constants a and b denote the horizontal and the vertical wave speeds, respectively.

Square-Wave Advection: Equation (3.70) is solved for the discontinuous initial condition shown in Fig. 27. The circle is advected diagonally towards the top-right of the domain with speed 1. Results after a single pass through the domain are presented in Fig. 28. Calculations are performed on 4 equally-spaced subdomains using weak SAT boundary and interface conditions. Each subdomain has 101×101 grid-points and the entire domain is discretized by 202×202 points.

3.2.3 Euler Equations

One-Dimensional Sod's Shock Tube Problem: The one-dimensional Euler equations,

$$\frac{\partial \boldsymbol{U}}{\partial t} + \frac{\partial \boldsymbol{F}}{\partial x} = 0, \tag{3.71}$$

$$\boldsymbol{U} = \begin{pmatrix} \rho \\ \rho u \\ \rho E \end{pmatrix}, \quad \boldsymbol{F} = \begin{pmatrix} \rho u \\ \rho u^2 + p \\ (\rho E + p)u \end{pmatrix},$$

are solved for the Sod's shock tube problem.[2] Results for strong and weak boundary and interface conditions for 4 equally-spaced subdomains with 101 grid-points each are shown in Fig. 29. Results for strong and weak boundary and interface conditions for 4 unequally-spaced subdomains with a maximum grid compression ratio of 4 are shown in Fig. 30. Each subdomain has 101 grid-points. Noticeable oscillations develop for strongly-imposed conditions. Weak conditions prevent oscillations in density and velocity; however, some perturbation in the energy persists.

Table 4: Comparison of total L_2 error and convergence rates for two-dimensional inviscid vortex convection problem on single and multiple subdomains.

Grid	Single domain		Four subdomains	
	$\log(L_2)$	Rate	$\log(L_2)$	Rate
21×21	-0.73		-0.74	
41×41	-1.81	3.60	-1.82	3.58
81×81	-3.00	3.95	-2.98	3.86
161×161	-3.98	3.25	-3.91	3.08
321×321	-4.68	2.32	-4.61	2.33
641×641	-5.30	2.05	-5.24	2.09

Two-Dimensional Inviscid Vortex: The two-dimensional Euler equations are solved for an inviscid vortex convection problem with exact solution,

$$f(x, y, t) = 1 - \left[(x - x_0 - U_\infty t)^2 + (y - y_0)^2\right],$$
$$\rho(x, y, t) = \left(1 - \epsilon^2 \frac{\gamma - 1}{8\pi^2} \exp(f(x, y, t))\right)^{\frac{1}{\gamma - 1}},$$
$$u(x, y, t) = U_\infty - \epsilon \frac{y - y_0}{2\pi} \exp\left(\frac{f(x, y, t)}{2}\right), \qquad (3.72)$$
$$v(x, y, t) = \epsilon \frac{x - x_0 - U_\infty t}{2\pi} \exp\left(\frac{f(x, y, t)}{2}\right),$$

$p = \frac{\rho}{\gamma}$, $U_\infty = M_\infty c_\infty$, $M_\infty = 0.5$, $x \in [0, 10]$, $y \in [-5, 5]$, $(x_0, y_0) = (5, 0)$.

The exact density solution is shown in Fig. 31. Calculations are performed on 4 equally-spaced subdomains using weak boundary and interface conditions. The L_2 error and convergence rates at $t = 10s$ with SAT interface conditions are shown in Table 4. Both single- and multi-domain results converge to the design-order. Moreover, the difference in L_2 error between the two configurations is small. Sample results are shown in Fig. 32, left column, where each subdomain has 101×101 grid-points, thus the total number of grid-points is 202×202. Calculations are also performed on 4 unequally-spaced subdomains using weak boundary and interface

Table 5: Number of grid-points in each subdomain for the inviscid vortex convection problem with unequally-spaced subdomain grids as shown in Figs. 33–34

Subdomain	N_x	N_y
Bottom left	201	91
Bottom right	91	91
Top left	201	201
Top right	91	201

conditions as shown in Fig. 33 and Fig. 34, left column. The number of grid-points for each subdomain is shown in Table 5. The total grid size is 292×292 and the maximum grid compression ratio across neighboring subdomains is 2.22.

Flow Over a Forward-Facing Step: Results are presented for inviscid flow over a forward-facing step at $Ma = 3.0$.[3,100] The computed density at $t = 4$ on 3 equally-spaced subdomains using weak SAT boundary and interface conditions is shown in Fig. 32. Subdomain partitions are shown. The total grid size is 241×81 and the results are compared with the fifth-order WENO scheme of Shu[3] on a 242×79 mesh. For demonstration, calculations are also performed on 3 subdomains with nonuniform grid-spacing. Results for $t = 3$ are shown in Fig. 34. The total

Table 6: Grid spacing for Mach 3 flow over a front-facing step.

Subdomain	Δx	Δy
Bottom left	0.0125	0.0125
Top left	0.0125	0.025
Top right	0.025	0.025

grid size is 145×49 and subdomain grid-spacing is shown in Table 6. Maximum grid compression ratio across neighboring subdomains is 2. Interference from the interfaces is slight; some dissipation is added at interfaces ($\sigma = -5$) to maintain stability.

3.3   CHAPTER SUMMARY

The closed-domain ESWENO 3-4-3 differentiation scheme[46] and the SAT penalty method[47] are combined to produce a robust solver for hyperbolic-dominated problems. This discretization methodology allows smooth solutions and captures discontinuities even with jumps in grid-spacing between subdomains. The flexibility, stability, and accuracy of the scheme are demonstrated. The methodology is designed to facilitate high-order accuracy on complex geometries, low-overhead parallelization, and flexibility of local grid refinement. With future extension of the method for three-dimensional discretization, it can be used for simulation of flows of interest to hypersonic propulsion.
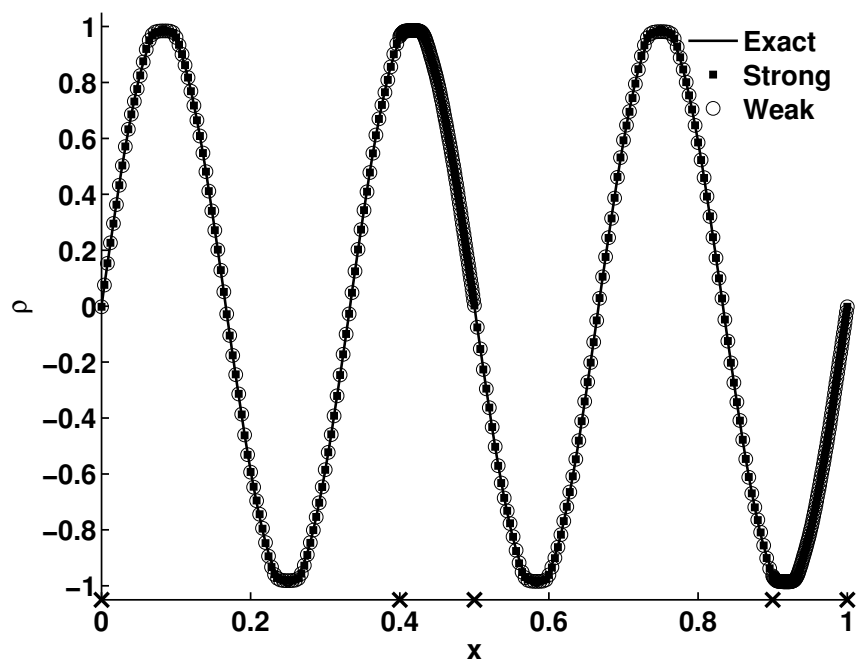
Figure 25: One-dimensional sine-wave advection problem after one flow-through time ($t = 1.0$) on 4 unequally-spaced subdomains for strong and weak (SAT) boundary and interface conditions. X's on the horizontal axis denote interface locations.
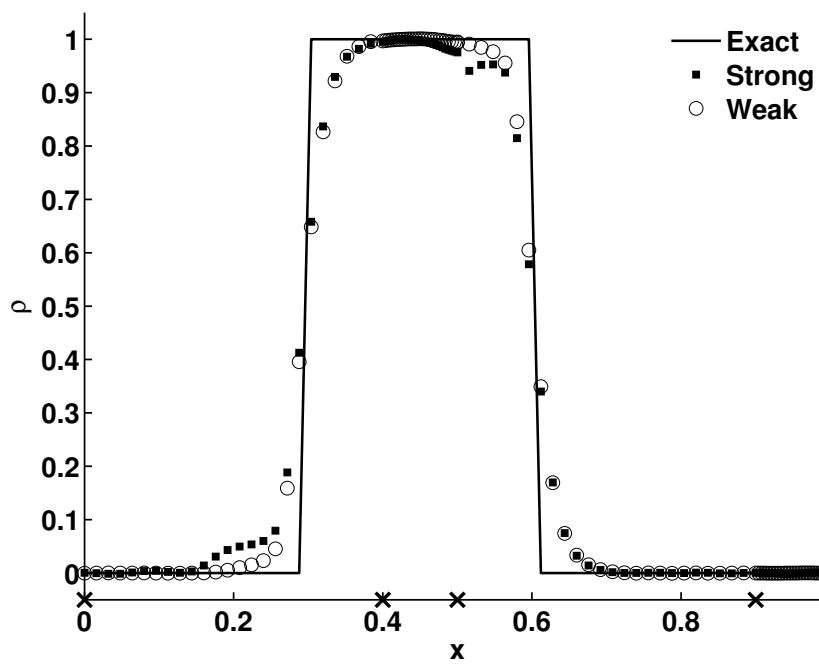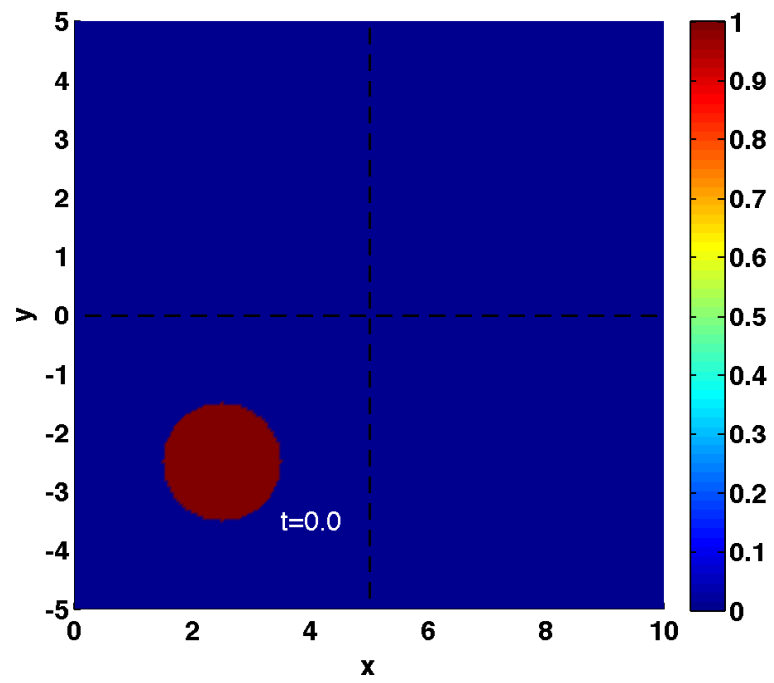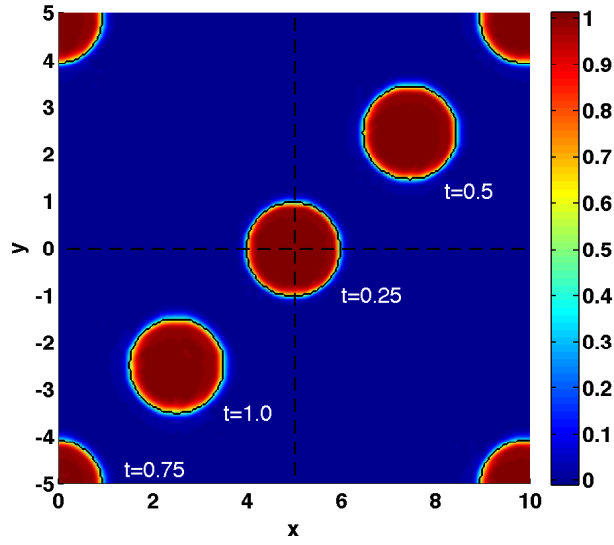
Figure 26: One-dimensional square-wave advection problem after one flow-through time on 4 unequally-spaced subdomains using both strong and weak boundary and interface conditions. X's on the horizontal axis denote interface locations.
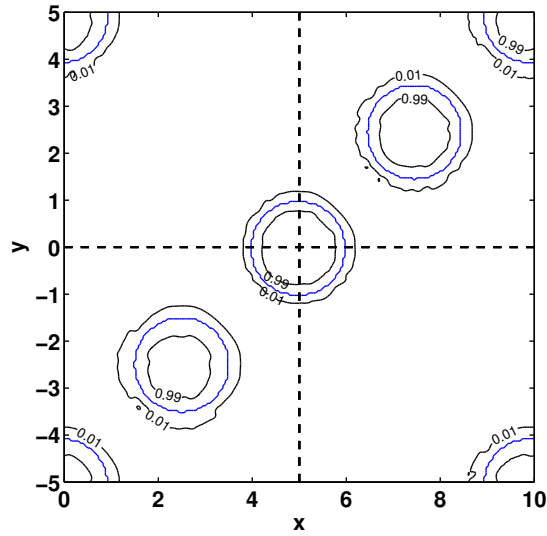
Figure 27: Initial condition, ρ, for two-dimensional square-wave advection problem.

Figure 28: Two-dimensional square-wave advection problem for one flow-through time on 4 equally-spaced subdomains using weak boundary and interface conditions. Dashed lines denote interface locations. In (a), solid lines denote exact solution and color contours are the numerical solution at various times. In (b), solid blue lines denote the exact solution and solid black lines represent contours $\rho = 0.01$ and $\rho = 0.99$ of the numerical solution to display shock smearing.
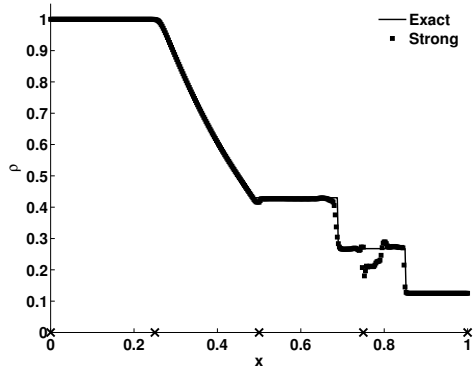
(a) Density
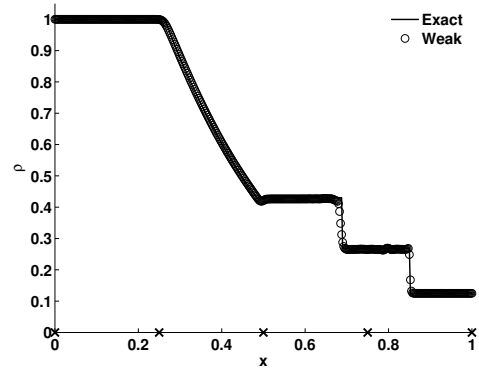
(b) Density
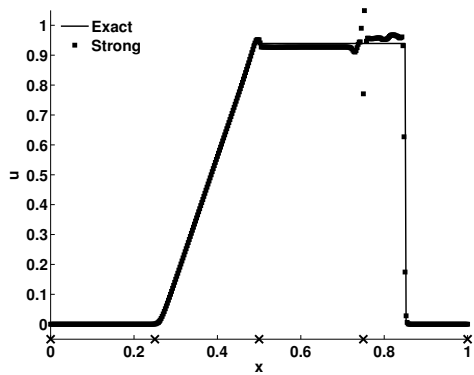
(c) Velocity

(d) Velocity

(e) Energy

(f) Energy

Figure 29: Sod's[2] one-dimensional shock tube problem at $t = 0.2$ on 4 equally-spaced subdomains. Left column: strong interface conditions. Right column: weak interface conditions. X's on horizontal axis denote interface locations.
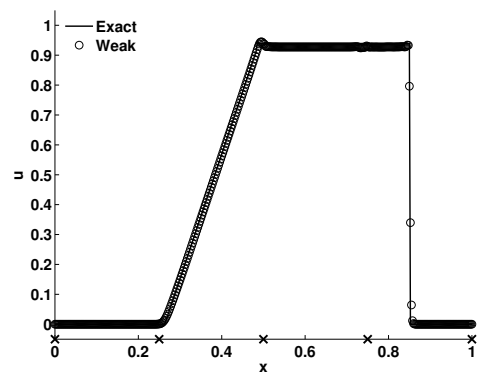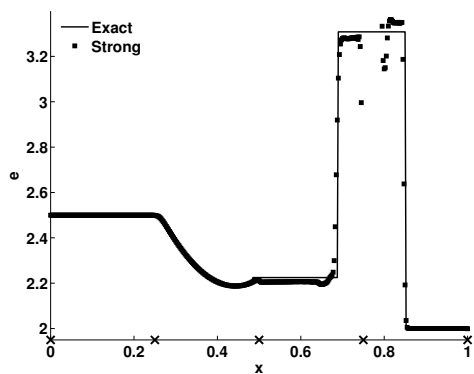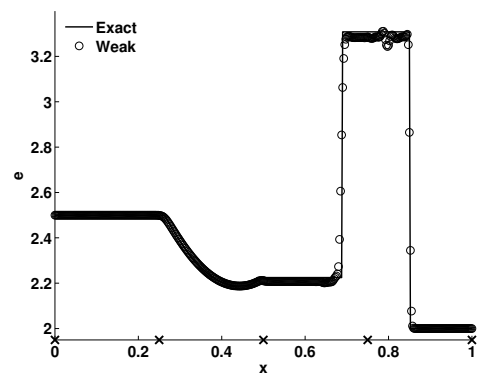
(a) Density
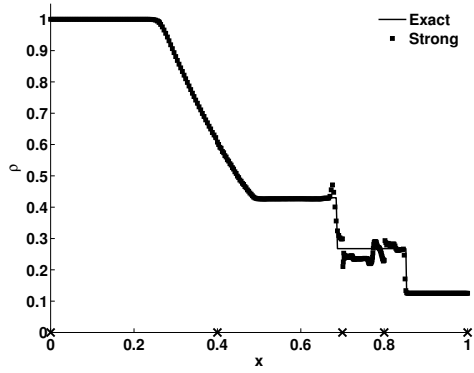
(b) Density
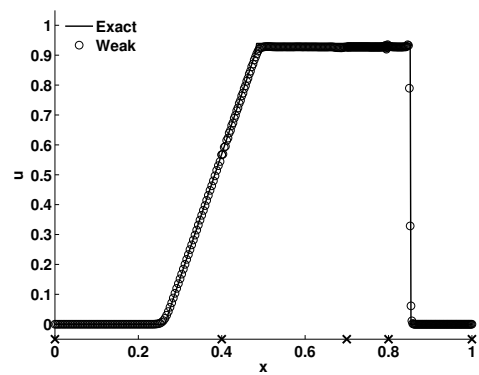
(c) Velocity

(d) Velocity
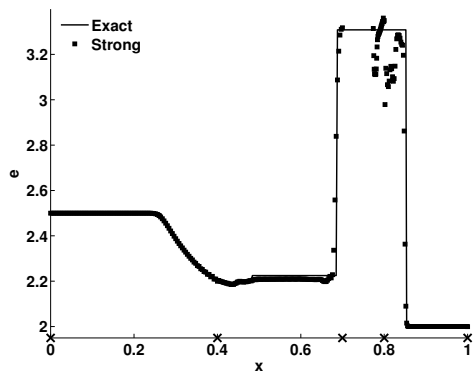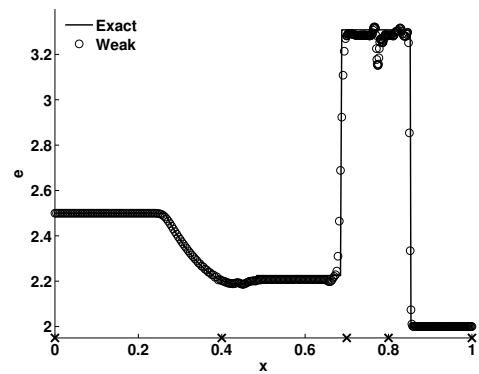
(e) Energy
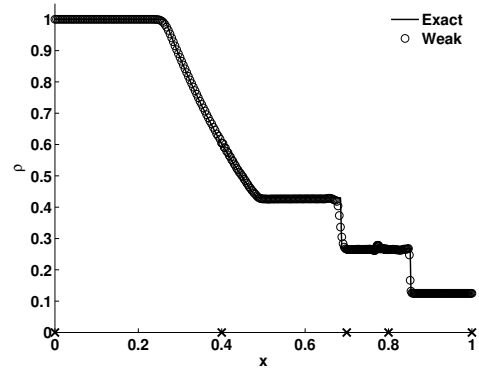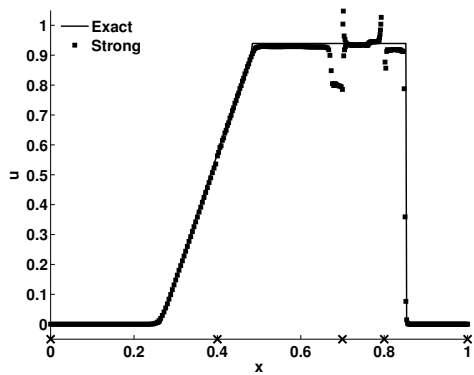
(f) Energy

Figure 30: Sod's[2] one-dimensional shock tube problem at $t = 0.2$ on 4 unequally-spaced subdomains. Left column: strong interface conditions. Right column: weak SAT interface conditions. X's on horizontal axis denote interface locations.
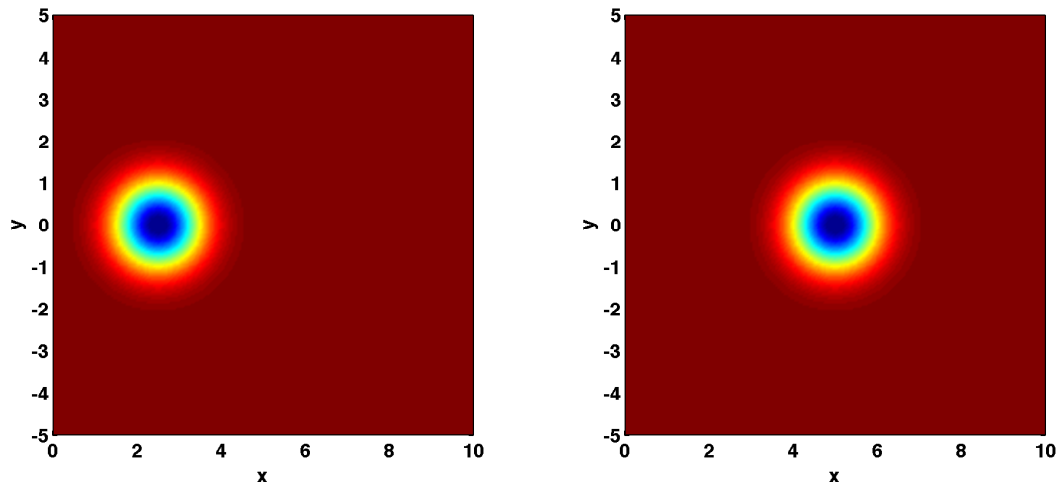
(a) $t = 0$.

(b) $t = 5$.
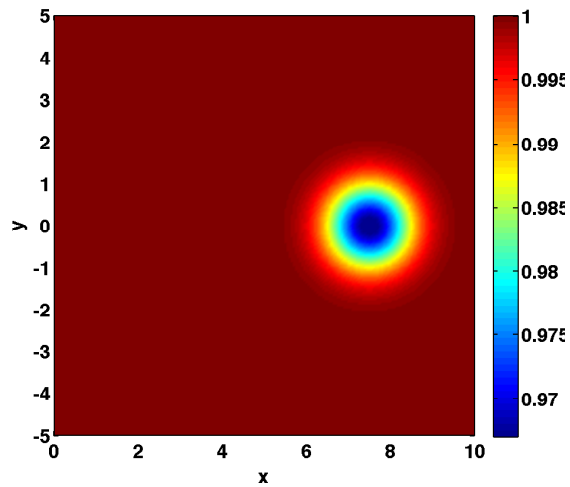
(c) $t = 10$.

Figure 31: Exact density solution for the inviscid vortex advection problem at various times.
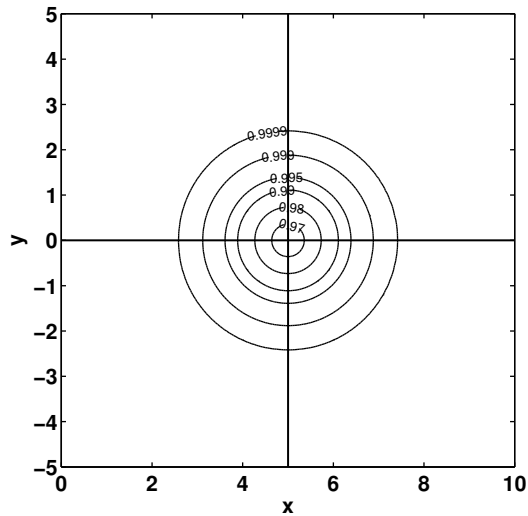
(a) Computed, $t = 5$ (b) Exact, $t = 5$
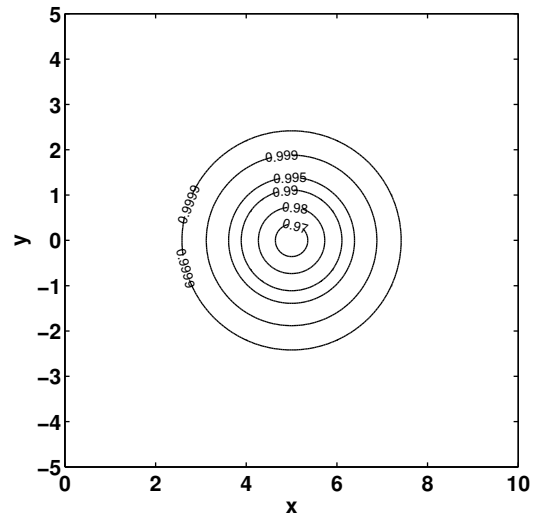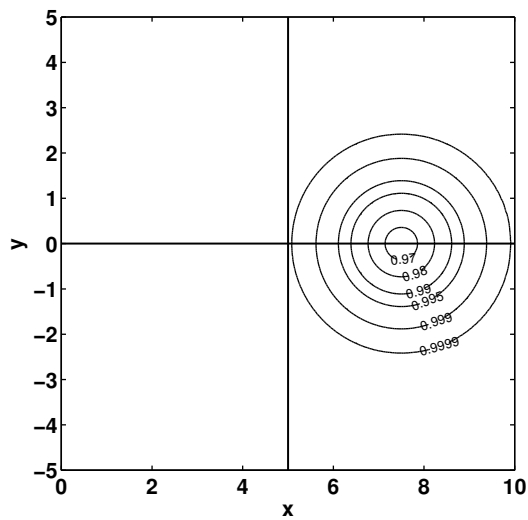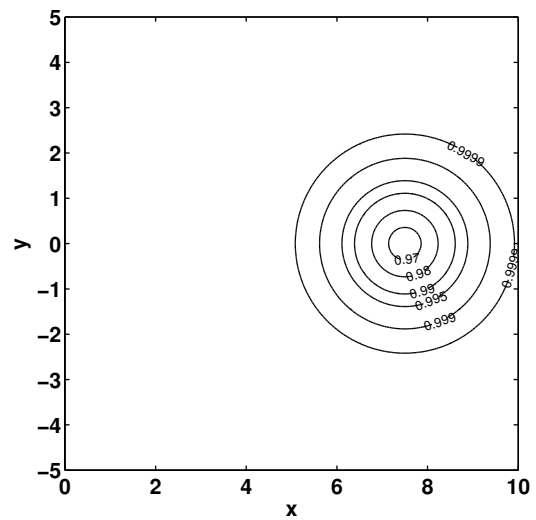
(c) Computed, $t = 10$ (d) Exact, $t = 10$

Figure 32: Density contours for inviscid vortex advection problem at various times. Left column: computed density on 4 equally-spaced subdomains using weak boundary and interface conditions. Solid lines denote interface locations. Right column: analytic solution.
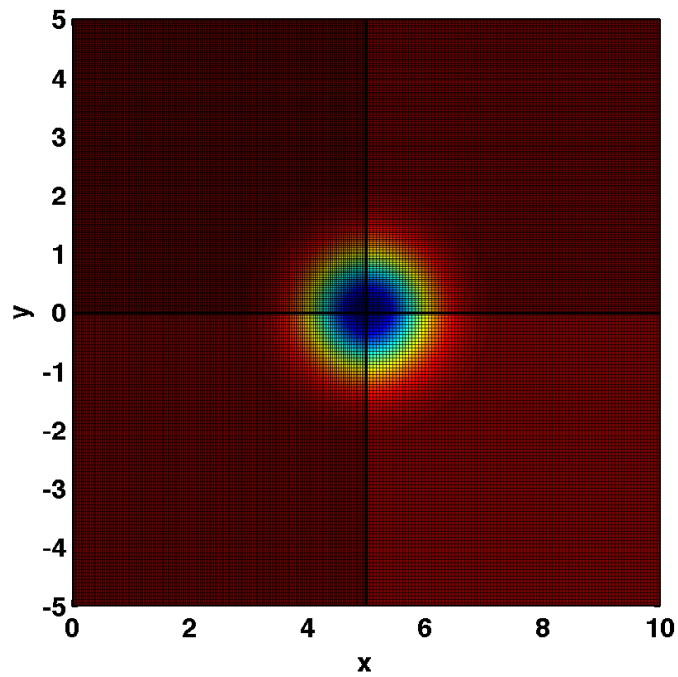
(a) $t = 5$

Figure 33: Computed density for the inviscid vortex advection problem on 4 unequally-spaced subdomains using weak (SAT) boundary and interface conditions. Subdomain grid sizes are shown in Table 5. Solid lines denote interface locations.
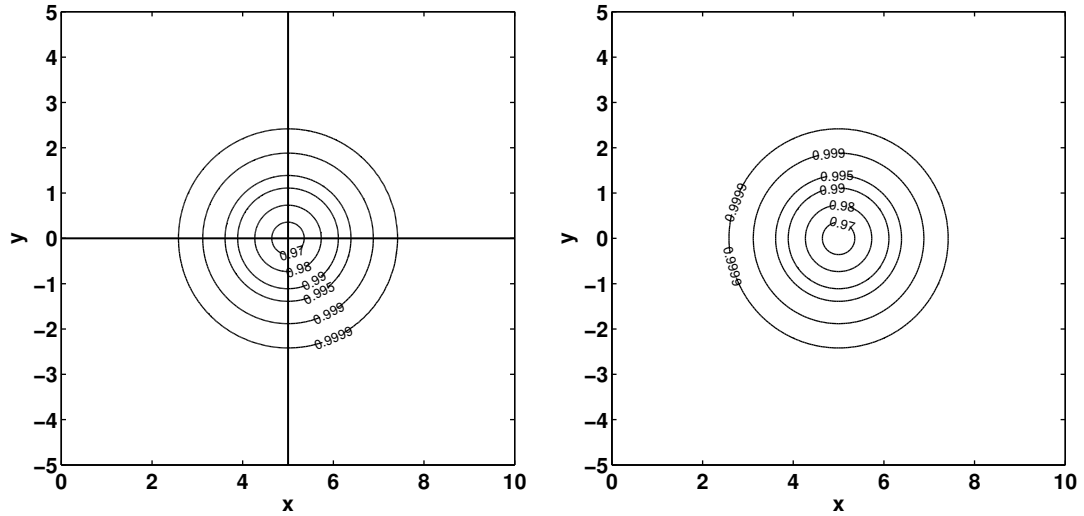
(a) Computed, $t = 5$

(b) Exact, $t = 5$
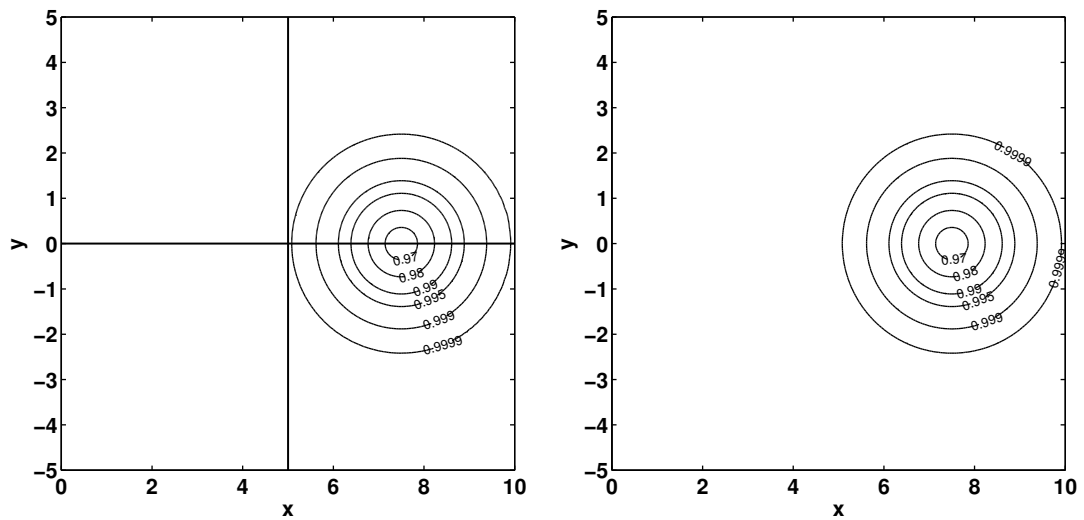
(c) Computed, $t = 10$

(d) Exact, $t = 10$

Figure 34: Density contours for inviscid vortex advection problem at various times. Left column: computed contours on 4 unequally-spaced subdomains using weak (SAT) boundary and interface conditions. Subdomain grid sizes are shown in Table 5 and Fig. 34. Right column: analytic solution.
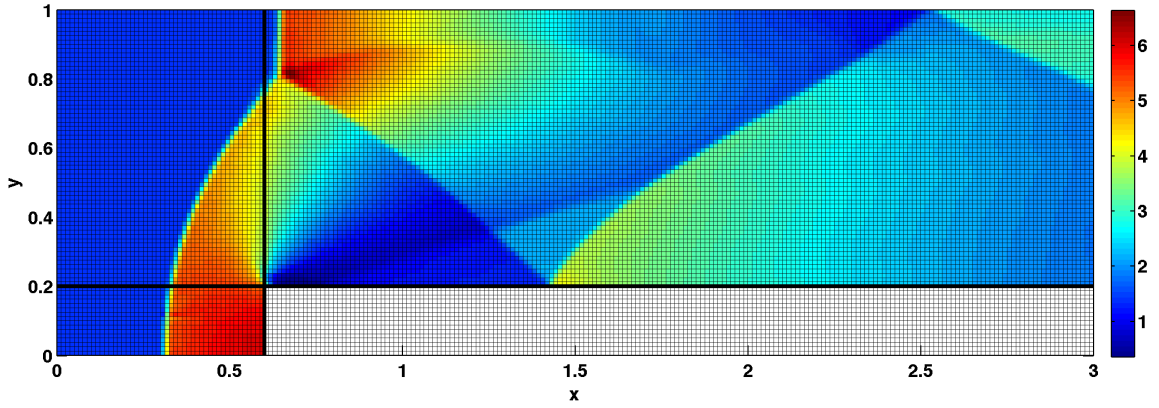
(a) Density with mesh overlaid
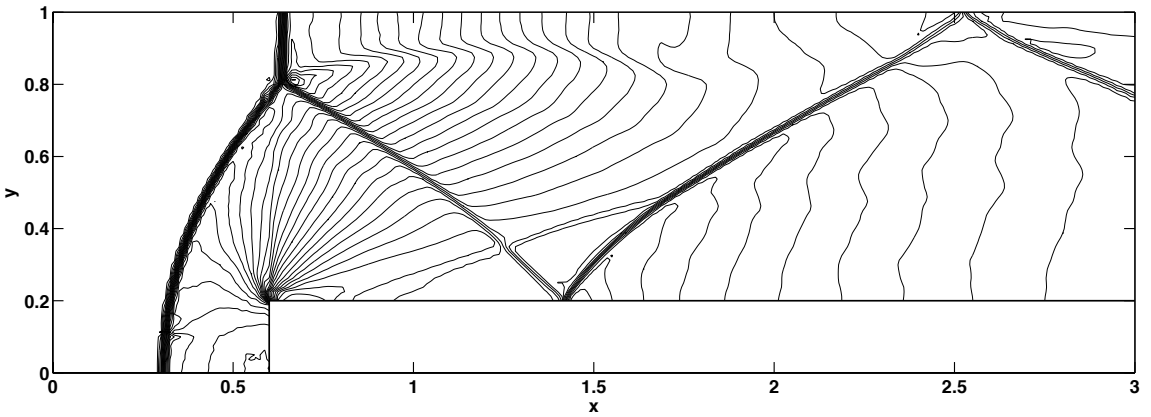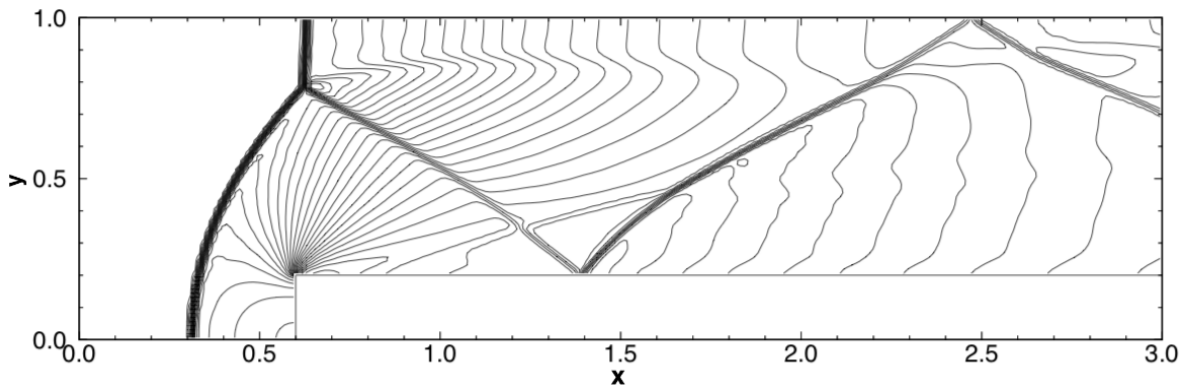
(b) Density

(c) Density from Ref.[3]

Figure 35: Computed density for two-dimensional Mach 3 flow over a forward-facing step at $t = 4$ with uniform grid-spacing. (a),(b) Computed result on 3 equally-spaced subdomains using weak boundary and interface conditions. In (a), bold solid lines denote interface locations. The entire grid is 241×81. (c) Result of Shu[3] for 5th-order WENO on a 242×79 mesh.
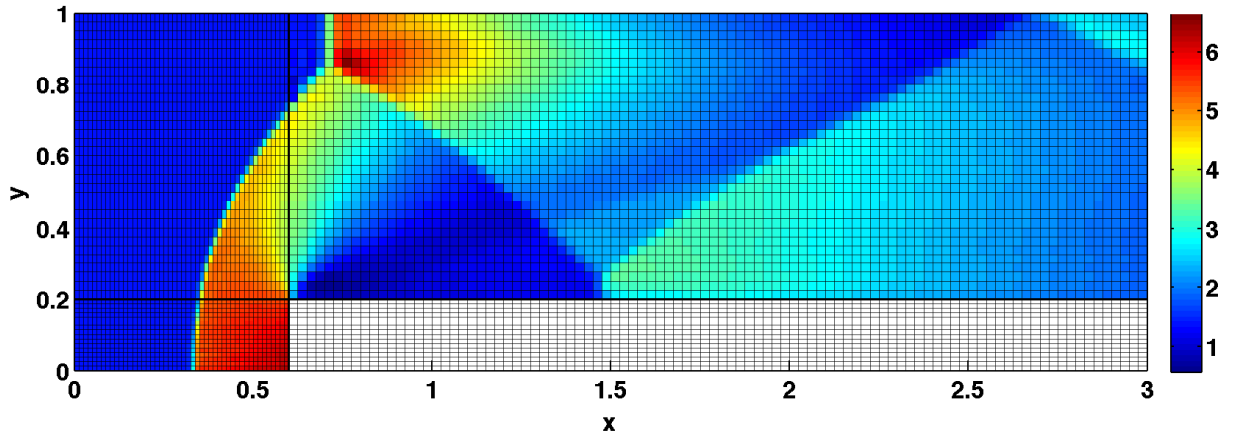
(a) Density with mesh overlaid
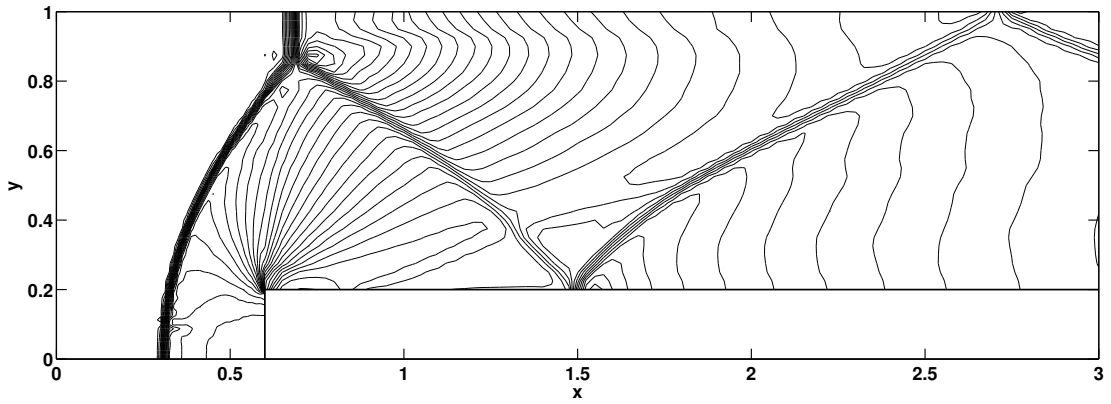
(b) Density

Figure 36: Computed density for two-dimensional Mach 3 flow over a forward-facing step at $t = 3$ with nonuniform grid-spacing. Computed result is on 3 unequally-spaced subdomains using weak boundary and interface conditions. Subdomain grid-spacing is shown in Table 6. Bold solid lines denote interface locations.

4.0 CONCLUSIONS

In this dissertation, the state of the art in turbulent combustion modeling and shock-capturing numerical methods for high-speed flows is advanced. These improvements facilitate high-fidelity prediction of high-speed turbulent reacting flows.

The first part of this dissertation involves extension of the filtered density function (FDF) for modeling of high-speed flows on unstructured meshes. Since its original conception, the FDF methodology, including its mass weighted form, the filtered mass density function (FMDF), has become popular for large eddy simulation (LES) of turbulent combustion.[8,11–14] The simplest and most widely used form considers only the scalar field (SFDF and SFMDF)[16,17] and has been successful in predicting many turbulent flames.[18–26] A major challenge associated with FDF is its implementation in complex geometries. Unstructured grids provide a good solution for meshing complex shapes; however, no previous work has been performed for FDF of high-speed flows on such grids. Herein, the SFMDF methodology is implemented into the US3D computer code.[27–36] This code is an unstructured finite volume solver and has been very effective for LES of compressible flows. The resulting hybrid SFMDF-US3D method is employed for LES of a temporally developing mixing layer. The consistency and accuracy of the methodology is demonstrated via simulations of low and high Mach number flows under both non-reacting and reacting conditions. In particular it is shown that the scheme is capable of accurate simulation of shock dominated flows.

The second part of this dissertation involves development of high-order numerical methods for solution of compressible flows. In these flows, the presence of discontinuities makes it very difficult to obtain accurate and stable solutions. Weighted essentially non-oscillatory (WENO) schemes have proven effective for overcoming

such challenges.[37–40] While WENO schemes are very robust in practice, their counterpart energy-stable WENO (ESWENO) schemes are needed to guarantee time-stability.[41–46] A major challenge in the practical application of ESWENO exists in generating appropriate finite-difference grids to match problem geometry and maintain high-order accuracy in the presence of shocks. Herein, a multi-block ESWENO scheme is developed that alleviates many practical grid-construction challenges. The new method allows smooth solutions and discontinuities to be captured and accurately passed across subdomain boundaries even with jumps in grid-spacing. The closed-domain ESWENO 3-4-3 differentiation scheme and SAT penalty method are combined to produce a robust solver for hyperbolic-dominated problems. The flexibility, stability, and accuracy of the scheme are demonstrated.

Some suggestions for future work include the following items:

- Implementation of SFMDF with the multi-block ESWENO scheme for high-order accurate simulation of high-speed turbulent reacting flows.
- Extension of SFMDF-US3D to use the stand-alone form of the FDF, the energy-pressure-velocity-scalar FMDF (EPVS-SFMDF).
- Extension of ESWENO for three-dimensional simulations.
- Implementation of SFMDF-US3D and ESWENO for LES of complex flow configurations.
- Implementation of curvilinear grid transformations in the context of the multi-block ESWENO scheme to facilitate high-order simulation on highly-complex geometries.
- Utilization of adaptive mesh refinement (AMR) in the multi-block ESWENO scheme.

APPENDIX A

SFMDF ENERGY CONSISTENCY

Here, we derive a transport equation for the Favre filtered total energy, $\langle E \rangle_L$, that is consistent with the equation for the filtered enthalpy, $\langle h \rangle_L$. The filtered enthalpy can be written in terms of the filtered total energy:

$$\langle h \rangle_L = \langle E \rangle_L + \frac{\langle p \rangle_l}{\langle \rho \rangle_l} - \frac{1}{2} \langle u_i u_i \rangle_L. \tag{A.1}$$

Substituting Eq. (A.1) into the filtered enthalpy equation, Eq. (2.24), yields

$$\frac{\partial \langle \rho \rangle_l \langle E \rangle_L}{\partial t} + \frac{\partial \langle \rho \rangle_l \langle u_i \rangle_L \langle E \rangle_L}{\partial x_i} = \frac{\partial}{\partial x_i} \left[(\gamma + \gamma_t) \frac{\partial \langle h \rangle_L}{\partial x_i} \right] + \langle \sigma_{ij} \rangle_L \frac{\partial \langle u_i \rangle_L}{\partial x_j} \\ + \frac{1}{2} \left[\frac{\partial \langle \rho \rangle_l \langle u_i u_i \rangle_L}{\partial t} + \frac{\partial \langle \rho \rangle_l \langle u_j \rangle_L \langle u_i u_i \rangle_L}{\partial x_j} \right]. \tag{A.2}$$

The transport equation for the filtered kinetic energy, $\langle u_i \rangle_L \langle u_i \rangle_L / 2$, is obtained by multiplying Eq. (2.22) by $\langle u_j \rangle_L$ and employing Eq. (2.21):

$$\frac{\partial \langle \rho \rangle_l \langle u_i \rangle_L \langle u_i \rangle_L}{\partial t} + \frac{\partial \langle \rho \rangle_l \langle u_j \rangle_L \langle u_i \rangle_L \langle u_i \rangle_L}{\partial x_j} = \langle u_i \rangle_L \frac{\partial \langle \sigma_{ji} \rangle_L}{\partial x_j} - \langle u_i \rangle_L \frac{\partial T_{ji}}{\partial x_j}. \tag{A.3}$$

Using the definition of SGS stress, Eq. (2.26), the transport equation for the turbulent kinetic energy is obtained:

$$\frac{1}{2} \frac{\partial \langle \rho \rangle_l \langle u_i u_i \rangle_L}{\partial t} + \frac{1}{2} \frac{\partial \langle \rho \rangle_l \langle u_j \rangle_L \langle u_i u_i \rangle_L}{\partial x_j} = \langle u_i \rangle_L \frac{\partial \langle \sigma_{ji} \rangle_L}{\partial x_j} - \langle u_i \rangle_L \frac{\partial T_{ji}}{\partial x_j} \\ + \frac{1}{2} \frac{\partial T_{ii}}{\partial t} + \frac{1}{2} \frac{\partial \langle u_j \rangle_L T_{ii}}{\partial x_j}. \tag{A.4}$$

71

Substituting Eq. (A.4) into Eq. (A.2), yields an enthalpy-consistent transport equation for the total energy:

$$
\frac{\partial \langle \rho \rangle_l \langle E \rangle_L}{\partial t} + \frac{\partial \langle \rho \rangle_l \langle u_i \rangle_L \langle E \rangle_L}{\partial x_i} = \frac{\partial}{\partial x_i} \left[(\gamma + \gamma_t) \frac{\partial \langle h \rangle_L}{\partial x_i} \right] + \frac{\partial \langle u_i \rangle_L \langle \sigma_{ij} \rangle_L}{\partial x_j}
$$
$$
- \langle u_n \rangle_L \frac{\partial \mathcal{T}_{in}}{\partial x_i} + \frac{1}{2} \left[\frac{\partial \mathcal{T}_{nn}}{\partial t} + \frac{\partial \langle u_i \rangle_L \mathcal{T}_{nn}}{\partial x_i} \right].
$$
(A.5)

The modeling assumptions in Section 2.1 imply the modeled energy equation,

$$
\frac{\partial \langle \rho \rangle_l \langle E \rangle_L}{\partial t} + \frac{\partial \langle \rho \rangle_l \langle u_i \rangle_L \langle E \rangle_L}{\partial x_i} = \frac{\partial}{\partial x_i} \left[\gamma \frac{\partial \langle h \rangle_L}{\partial x_i} \right] + \frac{\partial}{\partial x_i} \left[\lambda_t \frac{\partial \langle T \rangle_L}{\partial x_i} \right] + \frac{\partial \langle u_i \rangle_L \langle \sigma_{ij} \rangle_L}{\partial x_j}.
$$
(A.6)

Comparison of Eqs. (A.5)–(A.6) implies this requirement for consistency:

$$
\frac{\partial}{\partial x_i} \left[\gamma_t \frac{\partial \langle h \rangle_L}{\partial x_i} \right] - \langle u_n \rangle_L \frac{\partial \mathcal{T}_{in}}{\partial x_i} + \frac{1}{2} \left[\frac{\partial \mathcal{T}_{nn}}{\partial t} + \frac{\partial \langle u_i \rangle_L \mathcal{T}_{nn}}{\partial x_i} \right] = \frac{\partial}{\partial x_i} \left[\lambda_t \frac{\partial \langle T \rangle_L}{\partial x_i} \right].
$$
(A.7)

When converting between filtered enthalpy and energy variables, it is necessary to account for the turbulent kinetic energy. The filtered kinetic energy is defined as

$$
\left\langle \frac{1}{2} u_i u_i \right\rangle_L = \frac{1}{2} \langle u_i \rangle_L \langle u_i \rangle_L + \frac{1}{2} \frac{\mathcal{T}_{ii}}{\langle \rho \rangle_l}.
$$
(A.8)

Therefore, the conversion formulas are

$$
\langle h \rangle_L = \langle E \rangle_L + \frac{\langle p \rangle_L}{\langle \rho \rangle_l} - \frac{1}{2} \langle u_i \rangle_L \langle u_i \rangle_L - \frac{1}{2} \frac{\mathcal{T}_{ii}}{\langle \rho \rangle_l},
$$
(A.9)

$$
\langle E \rangle_L = \langle h \rangle_L - \frac{\langle p \rangle_L}{\langle \rho \rangle_l} + \frac{1}{2} \langle u_i \rangle_L \langle u_i \rangle_L + \frac{1}{2} \frac{\mathcal{T}_{ii}}{\langle \rho \rangle_l},
$$
(A.10)

$$
c_v \langle T \rangle_L = \langle E \rangle_L - \frac{1}{2} \langle u_i \rangle_L \langle u_i \rangle_L - \frac{1}{2} \frac{\mathcal{T}_{ii}}{\langle \rho \rangle_l} - \Delta h_\alpha^\circ \langle \phi_\alpha \rangle_L.
$$
(A.11)

ESWENO IMPLEMENTATION DETAILS

B.1 DISCRETE OPERATORS

The P-norm is

$$\boldsymbol{P} = \delta x \begin{pmatrix} \boldsymbol{P}_0 & 0 & 0 \\ 0 & \boldsymbol{I} & 0 \\ 0 & 0 & \boldsymbol{P}_0^{PT} \end{pmatrix}, \qquad (\text{B.1})$$

$$\boldsymbol{P}_0 = \frac{1}{15979414} \begin{pmatrix} 71043003 & -7964853 & 4820919 & -2199519 \\ -7964853 & 14093655 & 331299 & 1445721- \\ 4820919 & 331299 & 18932367 & 253203 \\ 2199519 & -1445721 & 253203 & 15938451 \end{pmatrix}.$$

The target $\boldsymbol{Q}$ matrix is

$$
\boldsymbol{Q} =
\begin{pmatrix}
-\frac{1}{2} & \frac{101}{144} & -\frac{29}{144} & 0 & 0 & 0 & 0 & 0 & 0 & 0 & 0 \\
-\frac{101}{144} & 0 & \frac{17}{24} & -\frac{1}{144} & 0 & 0 & 0 & 0 & 0 & 0 & 0 \\
\frac{29}{144} & -\frac{17}{24} & 0 & \frac{85}{144} & -\frac{1}{12} & 0 & 0 & 0 & 0 & 0 & 0 \\
0 & \frac{1}{144} & -\frac{85}{144} & 0 & \frac{2}{3} & -\frac{1}{12} & 0 & 0 & 0 & 0 & 0 \\
0 & 0 & \frac{1}{12} & -\frac{2}{3} & 0 & \frac{2}{3} & -\frac{1}{12} & 0 & 0 & 0 & 0 \\
0 & 0 & 0 & \ddots & \ddots & \ddots & \ddots & \ddots & 0 & 0 & 0 \\
0 & 0 & 0 & 0 & \frac{1}{12} & -\frac{2}{3} & 0 & \frac{2}{3} & -\frac{1}{12} & 0 & 0 \\
0 & 0 & 0 & 0 & 0 & \frac{1}{12} & -\frac{2}{3} & 0 & \frac{85}{144} & -\frac{1}{144} & 0 \\
0 & 0 & 0 & 0 & 0 & 0 & \frac{1}{12} & -\frac{85}{144} & 0 & \frac{17}{24} & -\frac{29}{144} \\
0 & 0 & 0 & 0 & 0 & 0 & 0 & \frac{1}{144} & -\frac{17}{24} & 0 & \frac{101}{144} \\
0 & 0 & 0 & 0 & 0 & 0 & 0 & 0 & \frac{29}{144} & -\frac{101}{144} & \frac{1}{2}
\end{pmatrix} .
\tag{B.2}
$$

The energy-stable terms are

$$
\boldsymbol{\Lambda}_1 = \mathrm{Diag}
\begin{pmatrix}
0 \\
\frac{1}{288}\left(58 - 100w_2^{(L)} - 101w_1^{(R)}\right) \\
\frac{1}{288}\left(-56 + 100w_2^{(L)} - 61w_3^{(L)} + 101w_1^{(R)} - 44w_2^{(R)}\right) \\
\frac{1}{288}\left(22 + 61w_3^{(L)} - 72w_4^{(L)} + 44w_2^{(R)} - 83w_3^{(R)}\right) \\
\frac{1}{288}\left(72w_4^{(L)} - 72w_5^{(L)} + 83w_3^{(R)} - 72w_4^{(R)}\right) \\
\frac{1}{4}\left(w_i^{(L)} - w_{i+1}^{(L)} + w_{i-1}^{(R)} - w_i^{(R)}\right) \\
\vdots \\
\frac{1}{4}\left(w_i^{(L)} - w_{i+1}^{(L)} + w_{i-1}^{(R)} - w_i^{(R)}\right) \\
\frac{1}{288}\left(72w_{N-4}^{(L)} - 83w_{N-3}^{(L)} + 72w_{N-5}^{(R)} - 72w_{N-3}^{(R)}\right) \\
\frac{1}{288}\left(-22 + 83w_{N-3}^{(L)} - 44w_{N-2}^{(L)} + 72w_{N-4}^{(R)} - 61w_{N-3}^{(R)}\right) \\
\frac{1}{288}\left(56 - 101w_{N-1}^{(L)} + 44w_{N-2}^{(L)} + 61w_{N-3}^{(R)} - 100w_{N-2}^{(R)}\right) \\
\frac{1}{288}\left(-58 + 101w_{N-1}^{(L)} + 100w_{N-2}^{(R)}\right) \\
0
\end{pmatrix} ,
\tag{B.3}
$$

$$\mathbf{\Lambda}_2 = \mathrm{Diag} \begin{pmatrix} 0 \\ \frac{1}{288}\left(100w_2^{(L)} - 101w_1^{(R)}\right) \\ \frac{1}{288}\left(61w_3^{(L)} - 44w_2^{(R)}\right) \\ \frac{1}{288}\left(72w_4^{(L)} - 83w_3^{(R)}\right) \\ \frac{1}{4}\left(w_i^{(L)} - w_{i-1}^{(R)}\right) \\ \vdots \\ \frac{1}{4}\left(w_i^{(L)} - w_{i-1}^{(R)}\right) \\ \frac{1}{288}\left(83w_{N-3}^{(L)} - 72w_{N-4}^{(R)}\right) \\ \frac{1}{288}\left(44w_{N-2}^{(L)} - 61w_{N-3}^{(R)}\right) \\ \frac{1}{288}\left(101w_{N-1}^{(L)} - 100w_{N-2}^{(R)}\right) \\ 0 \end{pmatrix}, \tag{B.4}$$

$$\mathbf{\Lambda}_3 = 0. \tag{B.5}$$

B.2 PSEUDOCODE FOR TWO-DIMENSIONAL EULER EQUATION IMPLEMENTATION

1. Read in options and parameters files. Initialize subdomain. Initialize MPI.

2. **FOR** each time iteration:

   ▷ **FOR** each Runge-Kutta (RK) substep:
   - Set conserved variables based on RK substep.
   - Compute local RK primitive variables and supplementary vars (enthalpy, sound speed, Mach number, pressure, etc.) from conserved variables.
   - Get analytic/exact solution for calculating L2 error norm and boundary conditions (if applicable).
   - **FOR** each dimension:
     * Define one-dimensional (1D) hyperbolic problem in current dimension.
     * **FOR** each 1D subproblem in the current dimension (e.g. for each row or column):

◇ Get boundary values via MPI call. (For efficiency, these are batched at the beginning of each RK substep in a future software release.)

◇ Reconstruct Roe-averaged variables at the flux points.

◇ Eigen decomposition: Calculate $\mathbf{\Lambda}$, $\mathbf{S}$, and $\mathbf{S}^{-1}$ at the flux-points based on Roe-averaged variables. (Store $\mathbf{\Lambda}_{max}$ for calculating maximum timestep.) At end-points, calculate decomposition matrices based on averaged state so that collocated interface points are moved to the same characteristic space.

◇ **FOR** each variable, calculate the derivative via ESWENO-SAT:

  ⋆ Move from physical to characteristic space. For each flux-point, rotate data at all solution-points in its stencil to its characteristic space and store in a vector local to each flux-point. Move boundary data to characteristic space.

  ⋆ Split into left-running and right-running waves.

  ⋆ **FOR** each split:

    ○ Interpolate flux onto flux points.

    ○ Calculate smoothness indicators based on characteristic variables.

    ○ Calculate WENO weights.

    ○ Calculate ESWENO stable dissipation and dissipative flux.

  ⋆ Join left-running and right-running fluxes and dissipative flux.

  ⋆ Add on interface penalty.

◇ Return to physical space.

◇ Calculate derivative as difference of fluxes.

• **IF** RKstep=1, calculate timestep based on target CFL.

▷ Integrate in time.

▷ Compute global primitive and supplementary variables.

3. Clean up memory and MPI. Output results files.

BIBLIOGRAPHY

[1] Sheikhi, M. R. H., Joint Velocity Scalar Filtered Density Function for Large Eddy Simulation of Turbulent Reacting Flows, Ph.D. Thesis, Department of Mechanical Engineering, University of Pittsburgh, Pittsburgh, PA, 2005.

[2] Sod, G. A., A Survey of Several Finite Difference Methods for Systems of Non-linear Hyperbolic Conservation Laws, *J. Comput. Phys.*, **27**(1):1–31 (1978).

[3] Shu, C.-W., Essentially Non-Oscillatory and Weighted Essentially Non-Oscillatory Schemes for Hyperbolic Conservation Laws, in *Advanced Numerical Approximation of Nonlinear Hyperbolic Equations*, Chapter 4, pp. 325–432, Springer, New York, NY, 1998.

[4] Drummond, J. P., Methods to Predict High-Speed Reacting Flows in Aerospace Propulsion Systems, in *48th AIAA/ASME/SAE/ASEE Joint Propulsion Conference and Exhibit*, 2012, AIAA-2012-0112.

[5] Kuo, K. K. and Acharya, R., *Fundamentals of Turbulent and Multiphase Combustion*, John Wiley and Sons Inc., Hoboken, NJ, 2012.

[6] Poinsot, T. and Veynante, D., *Theoretical and Numerical Combustion*, R. T. Edwards, Inc., Philadelphia, PA, 3rd edition, 2011.

[7] Janicka, J. and Sadiki, A., Large Eddy Simulation of Turbulent Combustion Systems, *Proc. Combust. Inst.*, **30**(1):537–547 (2005).

[8] Pope, S. B., *Turbulent Flows*, Cambridge University Press, Cambridge, U.K., 2000.

[9] Bilger, R. W., Future Progress in Turbulent Combustion Research, *Prog. Energ. Combust.*, **26**(4–6):367–380 (2000).

[10] Peters, N., *Turbulent Combustion*, Cambridge University Press, Cambridge, U.K., 2000.

[11] Givi, P., Model-Free Simulations of Turbulent Reactive Flows, *Prog. Energ. Combust.*, **15**(1):1–107 (1989).

[12] Givi, P., Filtered Density Function for Subgrid Scale Modeling of Turbulent Combustion, *AIAA J.*, **44**(1):16–23 (2006).

[13] Ansari, N., Jaberi, F. A., Sheikhi, M. R. H., and Givi, P., Filtered Density Function as a Modern CFD Tool, in Maher, A. R. S., editor, *Engineering Applications of Computational Fluid Dynamics*, pp. 1–22, International Energy and Environment Foundation, 2011.

[14] Pope, S. B., Computations of Turbulent Combustion: Progress and Challenges, *Proc. Combust. Inst.*, **23**(1):591–612 (1990).

[15] Nik, M. B., VS-FMDF and EPVS-FMDF for Large Eddy Simulation of Turbulent Flows, Ph.D. Thesis, Department of Mechanical Engineering and Materials Science, University of Pittsburgh, Pittsburgh, PA, 2012.

[16] Colucci, P. J., Jaberi, F. A., Givi, P., and Pope, S. B., Filtered Density Function for Large Eddy Simulation of Turbulent Reacting Flows, *Phys. Fluids*, **10**(2):499–515 (1998).

[17] Jaberi, F. A., Colucci, P. J., James, S., Givi, P., and Pope, S. B., Filtered Mass Density Function for Large-Eddy Simulation of Turbulent Reacting Flows, *J. Fluid Mech.*, **401**:85–121 (1999).

[18] Barlow, R. S. and Frank, J. H., Effects of Turbulence on Species Mass Fractions in Methane/Air Jet Flames, *Proc. Combust. Inst.*, **27**(1):1087–1095 (1998).

[19] Sandia National Laboratories, TNF Workshop Website, http://www.sandia.gov/TNF/, 2013.

[20] Nik, M. B., Yilmaz, S. L., Givi, P., Sheikhi, M. R. H., and Pope, S. B., Simulation of Sandia Flame D Using Velocity-Scalar Filtered Density Function, *AIAA J.*, **48**(7):1513–1522 (2010).

[21] Nik, M. B., Yilmaz, S. L., Sheikhi, M. R., and Givi, P., Grid Resolution Effects on VSFMDF/LES, *Flow Turbul. Combust.*, **85**(3–4):677–688 (2010).

[22] Sheikhi, M. R. H., Drozda, T. G., Givi, P., Jaberi, F. A., and Pope, S. B., Large Eddy Simulation of a Turbulent Nonpremixed Piloted Methane Jet Flame (Sandia Flame D), *Proc. Combust. Inst.*, **30**(1):549–556 (2005).

[23] Drozda, T. G., Sheikhi, M. R. H., Madnia, C. K., and Givi, P., Developments in Formulation and Application of the Filtered Density Function, *Flow Turbul. Combust.*, **78**(1):35–67 (2007).

[24] Yilmaz, S. L., Nik, M. B., Givi, P., and Strakey, P. A., Scalar Filtered Density Function for Large Eddy Simulation of a Bunsen Burner, *J. Propul. Power*, **26**(1):84–93 (2010).

[25] Ansari, N., Goldin, G. M., Sheikhi, M. R. H., and Givi, P., Filtered Density Function Simulator on Unstructured Meshes, *J. Comput. Phys.*, **230**(19):7132–7150 (2011).

[26] Ansari, N., Pisciuneri, P. H., Strakey, P. A., and Givi, P., Scalar-Filtered Mass-Density-Function Simulation of Swirling Reacting Flows on Unstructured Grids, *AIAA J.*, **50**(11):2476–2482 (2012).

[27] Peterson, D. M. and Candler, G. V., Hybrid Reynolds-Averaged and Large-Eddy Simulation of Normal Injection into a Supersonic Crossflow, *J. Propul. Power*, **26**(3):533–544 (2010).

[28] Subbareddy, P. K. and Candler, G. V., A Fully Discrete, Kinetic Energy Consistent Finite-Volume Scheme for Compressible Flows, *J. Comput. Phys.*, **228**(5):1347–1364 (2009).

[29] Candler, G. V., Peterson, D. M., and Drayna, T. W., Detached Eddy Simulation of a Generic Scramjet Inlet and Combustor, in *47th AIAA Aerospace Sciences Meeting*, 2009, AIAA 2009-0130.

[30] Nompelis, I., Drayna, T. W., and Candler, G. V., A Parallel Unstructured Implicit Solver for Hypersonic Reacting Flow Simulations, in *17th AIAA Computational Fluid Dynamics Conference*, 2007, AIAA 2005-4867.

[31] Martin, M. P. and Candler, G. V., A Parallel Implicit Method for the Direct Numerical Simulation of Wall-Bounded Compressible Turbulence, *J. Comput. Phys.*, **215**(1):153–171 (2006).

[32] Druguet, M.-C. and Candler, G. V., Effect of Numerics on Navier-Stokes Computations of Hypersonic Double-Cone Flows, *AIAA J.*, **43**(3):616–623 (2005).

[33] Wright, M. J., Candler, G. V., and Bose, D., Data-Parallel Line Relaxation Method for the Navier-Stokes Equations, *AIAA J.*, **36**(9):1603–1609 (1998).

[34] Nompelis, I., Drayna, T. W., and Candler, G. V., Development of a Hybrid Unstructured Implicit Solver for the Simulation of Reacting Flows Over Complex Geometries, in *34th AIAA Fluid Dynamics Conference*, 2004, AIAA 2004-2227.

[35] Candler, G. V. and Nompelis, I., Computational Fluid Dynamics for Atmospheric Entry, Technical Report, Von Karman Institute for Fluid Dynamics Lecture Series on Hypersonic Entry and Cruise Vehicles, 2008, RTO-EN-AVT-162.

[36] Candler, G. V., Nompelis, I., Druguet, M.-C., Holder, M. S., Wadhams, T. P., Boyd, I. D., and Wang, W.-L., CFD Validation for Hypersonic Flight: Hypersonic Double-Cone Flow Simulations, Technical Report, Aerospace Engineer-

ing and Mechanics & Army HPC Research Center, Minneapolis, MN, 2006, RTO-TR-AVT-007-V3.

[37] Borges, R., Carmona, M., Costa, B., and Don, W. S., An Improved Weighted Essentially Non-Oscillatory Scheme for Hyperbolic Conservation Laws, *J. Comput. Phys.*, **227**(6):3191–3211 (2008).

[38] Burger, R. and Kozakevicius, A., Adaptive Multiresolution WENO Schemes for Multi-Species Kinematic Flow Models, *J. Comput. Phys.*, **224**(2):1190–1222 (2007).

[39] Shu, C.-W., High Order Weighted Essentially Non-Oscillatory Schemes for Convection Dominated Problems, *SIAM Rev.*, **51**(1):82–126 (2009).

[40] Chou, C.-S. and Shu, C.-W., High Order Residual Distribution Conservative Finite Difference WENO Schemes for Convection-Diffusion Steady State Problems on Non-Smooth Meshes, *J. Comput. Phys.*, **224**(2):992–1020 (2007).

[41] Strand, B., Summation by Parts for Finite Difference Approximations for d/dx, *J. Comput. Phys.*, **110**(1):47–67 (1994).

[42] Kreiss, H.-O. and Scherer, G., Finite Element and Finite Difference Methods for Hyperbolic Partial Differential Equations, in *Mathematical Aspects of Finite Elements in Partial Differential Equations*, Academic Press, Inc., New York, NY, 1974.

[43] Yamaleev, N. K. and Carpenter, M. H., Third-Order Energy Stable WENO Scheme, *J. Comput. Phys.*, **228**(8):3025–3047 (2009).

[44] Yamaleev, N. K. and Carpenter, M. H., A Systematic Methodology for Constructing High-Order Energy Stable WENO Schemes, *J. Comput. Phys.*, **228**(11):4248–4272 (2009).

[45] Fisher, T. C., Carpenter, M. H., Yamaleev, N. K., and Frankel, S. H., Boundary Closures for Fourth-Order Energy Stable Weighted Essentially Non-Oscillatory Finite Difference Schemes, NASA TM 2009-216166, NASA Langley Research Center, Hampton, VA, 2009.

[46] Fisher, T. C., Carpenter, M. H., Yamaleev, N. K., and Frankel, S. H., Boundary Closures for Fourth-Order Energy Stable Weighted Essentially Non-Oscillatory Finite-Difference Schemes, *J. Comput. Phys.*, **230**(10):3727–3752 (2011).

[47] Carpenter, M. H., Nordstrom, J., and Gottlieb, D., A Stable and Conservative Interface Treatment of Arbitrary Spatial Accuracy, *J. Comput. Phys.*, **148**(2):341–365 (1999).

[48] Otis, C. C., Ferrero, P., Yilmaz, S. L., Candler, G. V., and Givi, P., SFMDF in US3D for LES of Compressible Flows on Unstructured Meshes, in *48th*

AIAA/ASME/SAE/ASEE Joint Propulsion Conference and Exhibit, 2012, AIAA-2012-4260.

[49] Ferrero, P., Candler, G. V., and Otis, C. C., Filtered Mass Density Function for Variable-Density Turbulent Reactive Flows on Unstructured Meshes, in *42nd AIAA Fluid Dynamics Conference and Exhibit*, 2012, AIAA-2012-2964.

[50] Yilmaz, S. L., Ansari, N., Pisciuneri, P. H., Nik, M. B., Otis, C. C., and Givi, P., Advances in FDF Modeling and Simulation, in *47th AIAA/AS-ME/SAE/ASEE Joint Propulsion Conference and Exhibit*, 2011, AIAA 2011-5918.

[51] Yilmaz, S. L., Ansari, N., Pisciuneri, P. H., Nik, M. B., Otis, C. C., and Givi, P., Applied Filtered Density Function, *J. Appl. Fluid Mech.*, (2013), in Press.

[52] Otis, C. C., A Semi-Unstructured Multi-Block Fourth-Order Energy Stable Weighted Essentially Non-Oscillatory Finite Difference Scheme, in *7th International Conference on Computational Fluid Dynamics*, 2012, ICCFD7-1602.

[53] Otis, C. C., A Multi-Block Fourth-Order Energy Stable Weighted Essentially Non-Oscillatory Finite Difference Scheme, in *42nd AIAA Fluid Dynamics Conference and Exhibit*, 2012, AIAA 2012-2837.

[54] Williams, F. A., *Combustion Theory*, The Benjamin/Cummings Publishing Company, Menlo Park, CA, second edition, 1985.

[55] Sagaut, P., *Large Eddy Simulation for Incompressible Flows*, Springer, New York, NY, third edition, 2010.

[56] Geurts, B. J., *Elements of Direct and Large-Eddy Simulation*, R. T. Edwards, Inc., Philadelphia, PA, 2004.

[57] Ghosal, S. and Moin, P., The Basic Equations for the Large Eddy Simulation of Turbulent Flows in Complex Geometry, *J. Comput. Phys.*, **118**(1):24–37 (1995).

[58] Smagorinsky, J., General Circulation Experiments with the Primitive Equations. I. The Basic Experiment, *Mon. Weather Rev.*, **91**(3):99–164 (1963).

[59] Yoshizawa, A. and Horiuti, K., A Statistically-Derived Subgrid Scale Kinetic Energy Model for Large Eddy Simulation of Turbulent Flows, *J. Phys. Soc. Japan*, **54**(8):2834–2839 (1985).

[60] Yoshizawa, A., Statistical Modelling of Passive-Scalar Diffusion in Turbulent Shear Flows, *J. Fluid Mech.*, **195**:541–555 (1988).

[61] Martin, P. M., Piomelli, U., and Candler, G. V., Subgrid Scale Models for Compressible Large Eddy Simulations, *Theoret. Comput. Fluid Dyn.*, **13**(5):361–376 (2000).

[62] Lundgren, T. S., Distribution Functions in the Statistical Theory of Turbulence, *Phys. Fluids*, **10**(5):969–975 (1967).

[63] O'Brien, E. E., The Probability Density Function (PDF) Approach to Reacting Turbulent Flows, in Libby, P. and Williams, F., editors, *Turbulent Reacting Flows*, *Topics in Applied Physics*, Vol. 44, Chapter 5, pp. 185–218, Springer Berlin / Heidelberg, 1980.

[64] Dopazo, C. and O'Brien, E. E., Statistical Treatment of Non-Isothermal Chemical Reactions in Turbulence, *Combust. Sci. Technol.*, **13**(1–6):99–122 (1976).

[65] Pope, S. B., PDF Methods for Turbulent Reactive Flows, *Prog. Energ. Combust.*, **11**(2):119–192 (1985).

[66] Pope, S. B., On the Relation Between Stochastic Lagrangian Models of Turbulence and Second-Moment Closures, *Phys. Fluids*, **6**(2):973–985 (1994).

[67] Risken, H., *The Fokker-Planck Equation, Methods of Solution and Applications*, Springer-Verlag, New York, NY, 1989.

[68] Gardiner, C. W., *Handbook of Stochastic Methods for Physics, Chemistry and the Natural Sciences*, Springer-Verlag, New York, NY, second edition, 1990.

[69] Peterson, D. M., Simulations of Injection, Mixing, and Combustion in Supersonic Flow Using a Hybrid RANS/LES Approach, Ph.D. Thesis, Aerospace Engineering & Mechanics, University of Minnesota, Minneapolis, MN, 2011.

[70] Nompelis, I., Computational Study of Hypersonic Double-Cone Experiments for Code-Validation, Ph.D. Thesis, Aerospace Engineering & Mechanics, University of Minnesota, Minneapolis, MN, 2004.

[71] Hirsch, C., *Numerical Computation of Internal and External Flows*, Wiley, New York, NY, 1991.

[72] Ducros, F., Ferrand, V., Nicoud, F., Weber, C., Darracq, D., Gacherieu, C., and T., P., Large-Eddy Simulation of the Shock/Turbulence Interaction, *J. Comput. Phys.*, **152**(2):517–549 (1999).

[73] Kloeden, P. E. and Platen, E., *Numerical Solution of Stochastic Differential Equations*, *Applications of Mathematics*, Vol. 23, Springer, Berlin; New York, corr. 3rd print edition, 1999.

[74] Madnia, C., Jaberi, F. A., and Givi, P., Large Eddy Simulation of Heat and Mass Transport in Turbulent Flows, in Minkowycz, W. J., Sparrow, E. M., and Murthy, J. Y., editors, *Handbook of Numerical Heat Transfer*, Chapter 5, pp. 167–190 (2006), John Wiley & Sons, Inc., New York, NY, 2nd edition, 2006.

[75] Moser, R. D. and Rogers, M. M., The Three-Dimensional Evolution of a Plane Mixing Layer: Pairing and Transition to Turbulence, *J. Fluid Mech.*, **247**:275–320 (1993).

[76] Moser, R. D. and Rogers, M. M., The Three-Dimensional Evolution of a Plane Mixing Layer: The Kelvin-Helmholtz Rollup, *J. Fluid Mech.*, **243**:183–226 (1992).

[77] McMurtry, P. A., Jou, W.-H., Riley, J. J., and Metcalfe, R. W., Direct Numerical Simulations of a Reacting Mixing Layer with Chemical Heat Release, *AIAA J.*, **24**:962–970 (1986).

[78] McMurtry, P. A., Riley, J. J., and Metcalfe, R. W., Effects of Heat Release on the Large Scale Structures in a Turbulent Reacting Mixing Layer, *J. Fluid Mech.*, **199**:297–332 (1989).

[79] Vreman, B., Geurts, B., and Kuerten, H., Realizability Conditions for the Turbulent Stress Tensor in Large-Eddy Simulation, *J. Fluid Mech.*, **278**:351–362 (1994).

[80] Drozda, T. G., Implementation of LES/SFMDF for Prediction of Non-Premixed Turbulent Flames, Ph.D. Thesis, Department of Mechanical Engineering, University of Pittsburgh, Pittsburgh, PA, 2005.

[81] Bilger, R. W., Turbulent Flows with Nonpremixed Reactants, in Libby, P. and Williams, F., editors, *Turbulent Reacting Flows*, *Topics in Applied Physics*, Vol. 44, Chapter 3, pp. 65–113, Springer Berlin / Heidelberg, 1980.

[82] McMurtry, P. A., Direct Numerical Simulation of a Reacting Mixing Layer with Chemical Heat Release, Ph.D. Thesis, Mechanical Engineering Department, University of Washington, Seattle, WA, 1987.

[83] Sebastian, K. and Shu, C.-W., Multidomain WENO Finite Difference Method with Interpolation at Subdomain Interfaces, *J. Sci. Comput.*, **19**:405–438 (2003).

[84] Costa, B. and Don, W. S., Multi-Domain Hybrid Spectral-WENO Methods for Hyperbolic Conservation Laws, *J. Comput. Phys.*, **224**(2):970–991 (2007).

[85] Chao, J., Haselbacher, A., and Balachandar, S., A Massively Parallel Multi-Block Hybrid Compact-WENO Scheme for Compressible Flows, *J. Comput. Phys.*, **228**(19):7473–7491 (2009).

[86] Erlebacher, F., Hussaini, M. Y., and Shu, C.-W., Interaction of a Shock with a Longitudinal Vortex, *J. Fluid Mech.*, **337**(1):129–153 (1997).

[87] Zhang, S., Jiang, S., Zhang, Y., and Shu, C.-W., The Mechanism of Sound Generation in the Interaction Between a Shock Wave and Two Counter-Rotating Vortices, *Phys. Fluids*, **21**(7) (2009).

[88] Jiang, G.-S. and Shu, C.-W., Efficient Implementation of Weighted ENO Schemes, *J. Comput. Phys.*, **126**(1):202–228 (1996).

[89] Gustafsson, B., The Convergence Rate for Difference Approximations to Mixed Initial Boundary Value Problems, *Math Comput.*, **29**(130):396–406 (1975).

[90] Svard, M. and Nordstrom, J., On the Order of Accuracy for Difference Approximations of Initial-Boundary Value Problems, *J. Comput. Phys.*, **218**(1):333–352 (2006).

[91] Carpenter, M. H., Gottlieb, D., and Abarbanel, S., Time-Stable Boundary Conditions for Finite-Difference Schemes Solving Hyperbolic Systems: Methodology and Application to High-Order Compact Systems, *J. Comput. Phys.*, **111**:220–236 (1994).

[92] Nordstrom, J. and Carpenter, M. H., Boundary and Interface Conditions for High-Order Finite Difference Methods Applied to the Euler and Navier-Stokes Equations, *J. Comput. Phys.*, **148**(2):621–645 (1999).

[93] Nordstrom, J. and Carpenter, M. H., High-Order Finite Difference Methods, Multidimensional Linear Problems, and Curvilinear Coordinates, *J. Comput. Phys.*, **173**(1):149–174 (2001).

[94] Mattsson, K., Svard, M., Carpenter, M. H., and Nordstrom, J., High-Order Accurate Computations for Unsteady Aerodynamics, *Comp. Fluids*, **36**:636–649 (2007).

[95] Svard, M., Carpenter, M. H., and Nordstrom, J., A Stable High-Order Finite Difference Scheme for the Compressible Navier-Stokes Equations, Far-Field Boundary Conditions, *J. Comput. Phys.*, **225**(1):1020–1038 (2007).

[96] Pulliam, T. H., A Diagonal Form of an Implicit Approximate-Factorization Algorithm, *J. Comput. Phys.*, **39**(2):347 – 363 (1981).

[97] Berger, M. J. and Oliger, J., Adaptive Mesh Refinement for Hyperbolic Partial Differential Equations, *J. Comput. Phys.*, **53**(3):484 – 512 (1984).

[98] Berger, M. J. and Colella, P., Local Adaptive Mesh Refinement for Shock Hydrodynamics, *J. Comput. Phys.*, **82**(1):64 – 84 (1989).

[99] Hoffman, J., *Numerical Methods for Engineers and Scientists*, Marcel Dekker, New York, NY, 2001.

[100] Woodward, P. and Colella, P., The Numerical Simulation of Two-Dimensional Fluid Flow with Strong Shocks, *J. Comput. Phys.*, **54**(1):115 – 173 (1984).